The SHMS 11 GeV/c Spectrometer in Hall C at Jefferson Lab

S. Ali[a], A. Ahmidouch[b], G.R. Ambrose[c], A. Asaturyan[d,e], J. Benesch[e], V. Berdnikov[a,e], H. Bhatt[k], P. Brindza[e], M. Bukhari[u], M. Burton[f,g], R. Carlini[e], M. Carmignotto[a], M. E. Christy[e,h], C. Cotton[i], J. Crafts[a], D. Day[i], S. Danagoulian[b], A. Dittmann[j], B. Duran[s,t], D. Dutta[k], R. Ent[e], H. Fenker[e], M. Fowler[e], D. Gaskell[e], A. Hamdi[c], N. Heinrich[c], W. Henry[e], N. Hlavin[a], T. Horn[a,e], G.M. Huber[c], Y. Illieva[l], J. Jarrell[f,m], M. K. Jones[e,*], M. Junaid[c], N. Kalantarians[n], S.J.D. Kay[c,o], V. Kumar[c], S. Lassiter[e], W.B. Li[c,p], S. Malace[e], A. Mkrtchyan[a], H. Mkrtchyan[d], P. Monaghan[h,q], C. Morean[a], P. Nadel-Turonski[e], G. Niculescu[f], M. I. Niculescu[f], A. Ramos[r], J. Reinhold[r], B. Sawatzky[e], H. Szumila-Vance[e], V. Tadevosyan[d], R.L. Trotta[a], A. Usman[c], M. Yurov[i], S. Zhamkochyan[d], S. A. Wood[e], J. Zhang[i]

[a] *The Catholic University of America, Washington, DC 20064, USA*
[b] *North Carolina A&T State University, North Carolina 27411, USA*
[c] *University of Regina, Regina, Saskatchewan S4S 0A2, Canada*
[d] *A. I. Alikhanyan National Science Laboratory, Yerevan 0036, Armenia*
[e] *Thomas Jefferson National Accelerator Facility, Newport News, Virginia 23606, USA*
[f] *James Madison University, Harrisonburg, Virginia 22801, USA*
[g] *Johns Hopkins University Applied Physics Laboratory, Laurel, Maryland 20723, USA*
[h] *Hampton University, Hampton, Virginia 23668, USA*
[i] *University of Virginia, Charlottesville, Virginia 22904, USA*
[j] *University of Illinois, Urbana-Champaign, Illinois, USA*
[k] *Mississippi State University, Mississippi State, Mississippi 39762, USA*
[l] *University of South Carolina, Columbia, South Carolina 29208, USA*
[m] *Lawrence Berkeley National Laboratory, Berkeley, California 94720, USA*
[n] *Virginia Union University, Richmond, Virginia 23220, USA*
[o] *University of York, Heslington, York, Y010 5DD, UK*
[p] *Stony Brook University, Stony Brook, New York 11794, USA*
[q] *Christopher Newport University, Newport News, Virginia, 23606, USA*
[r] *Florida International University, University Park, Florida 33199, USA*
[s] *Temple University, Philadelphia, PA, USA*
[t] *Argonne National Laboratory, Lemont, IL, USA*
[u] *Jazan University, Jazan 45142, Saudi Arabia*

Abstract

The *Super High Momentum Spectrometer* (SHMS) has been built for Hall C at the Thomas Jefferson National Accelerator Facility (Jefferson Lab). With a momentum capability reaching 11 GeV/c, the SHMS provides measurements of secondary charged particles produced in electron scattering experiments using the maximum available beam energy from the upgraded Jefferson Lab accelerator. The SHMS is an ion-optics magnetic spectrometer comprised of a series of new superconducting magnets which transport charged particles through an array of triggering, tracking, and particle-identification detectors that measure momentum, energy, angle and position in order to allow kinematic reconstruction of the events back to their origin at the scattering target. The detector system is protected from background radiation by a sophisticated shielding enclosure. The entire spectrometer is mounted on a rotating support structure which allows measurements to be taken with a large acceptance over laboratory scattering angles from 5.5° to 40°, thus allowing a wide range of low cross-section experiments to be conducted. These will complement and extend the previous Hall C research program to higher energies.

Keywords: Magnetic spectrometer, Electron scattering, Tracking detectors, Particle identification, Electron calorimetry, Radiation shielding.

1. Introduction

1.1. Jefferson Lab Overview

The Continuous Electron Beam Accelerator Facility at Thomas Jefferson National Accelerator Facility (Jefferson Lab) provides high energy electron beams for fundamental nuclear physics experiments. Originally planned for maximum electron beam energies of 4 GeV, the accelerator operated at energies of up to 6 GeV starting in 2000. An upgrade of the facility was completed in 2017, enabling beam delivery at a maximum energy of 12 GeV to the new experimental Hall D, and 11 GeV to the existing Halls, A, B, and C.

The electron beam at Jefferson Lab operates at high duty cycle, with beam repetition rates of 249.5 or 499 MHz delivered to the experimental halls. High beam polarization (> 80%) is also routinely available.

In the 6 GeV era, Halls A, B, and C executed a large program of experiments focusing primarily on elucidating the quark-gluon structure of nucleons and nuclei. Experimental Hall B made use of a large acceptance spectrometer capable of detecting many-body final states over a large region of kinematic phase space in one setting. Halls A and C made use of magnetic focusing spectrometers. In Hall A, the two High Resolution Spectrometers (HRS) emphasized excellent momentum resolution. In Hall C, the Short Orbit Spectrometer (SOS) facilitated the detection of short-lived final states (pions and kaons) at modest momentum while the High Momentum Spectrometer was capable of detecting particles up the maximum beam energy at Jefferson Lab.

As part of the 12 GeV upgrade at Jefferson Lab, a new experimental hall, Hall D, was built to search for gluonic excitations in the meson spectrum using a photon beam produced via coherent bremsstrahlung. The GlueX experiment in Hall D began commissioning in 2014 and has taken production-quality data since 2016.

The existing Halls A, B, and C were also upgraded as part of the 12 GeV upgrade. The Hall A beamline and beam polarimeters were upgraded to accommodate operation at 11 GeV. Hall A has made use of the existing HRS spectrometers in its early 12 GeV era experiments (which began initial data-taking in 2014) and has also installed specialized, dedicated equipment for recent measurements. Experimental Hall B replaced its large acceptance CLAS spectrometer with the new CLAS-12 spectrometer. This new spectrometer retains the key features of large acceptance and robust particle identification over a large momentum range but with more emphasis on particle detection in the forward direction, required due to the higher beam energies. Finally, Hall C replaced its Short Orbit Spectrometer with the new Super-High Momentum Spectrometer (SHMS). This new spectrometer was designed guided by experience from the 6 GeV program, with the goal of serving as an optimal partner to the HMS for coincidence experiments.

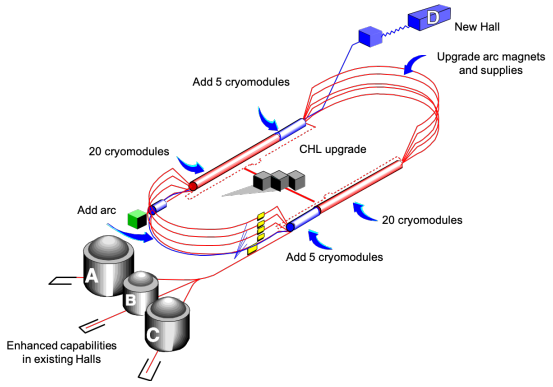

Figure 1: Schematic of hall and accelerator improvements as part of the Jefferson Lab 12 GeV Upgrade.

1.2. Hall C Experimental Program at 6 GeV

The HMS and SOS spectrometers in Hall C enabled the execution of a diverse program of experiments. The well-understood acceptance of both spectrometers, in tandem with excellent kinematic reproducibility allowed the extraction of precise cross sections. A particular strength was the control of point-to-point systematic uncertainties, which allowed high precision Rosenbluth, or L-T, separations. Examples of inclusive cross section measurements, using primarily the HMS, are shown in Figs. 2 and 3.

In addition, the small minimum angle (10.5 degrees) accessible with the HMS allowed the execution of pion electroproduction experiments, where, in many cases, the pion is emitted in the forward direction. This allowed the successful execution of a program of measurements of the pion form factor [3, 4], which also incorporates precise L-T separations, as well measurements of charged pion production in Semi-inclusive Deep Inelastic Scattering (SIDIS) [5] (see Figs. 4 and 5).

The high momentum reach of the HMS (up to the available beam energy of 6 GeV) enabled measurements of the $A(e,e'p)$ process to large Q^2 [6, 7] (Fig. 6) to look for signs of color transparency as well measurements of

*jones@jlab.org

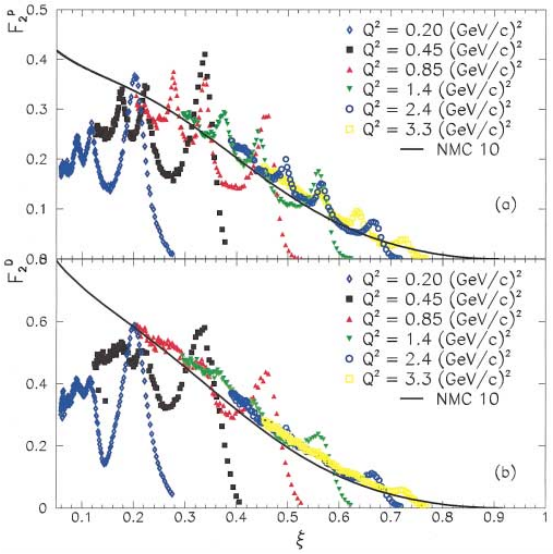

Figure 2: Inclusive F_2 structure functions measured in the resonance region compared to a DIS fit. When plotted vs. the Nachtmann variable ξ, the DIS fit agrees, on average, with the resonance region data, demonstrating quark-hadron duality [1].

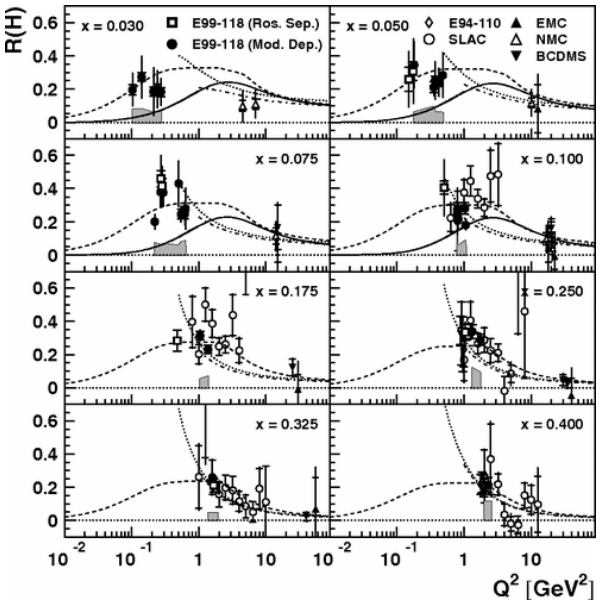

Figure 3: Measurement of $R = \frac{\sigma_L}{\sigma_T}$ at low Q^2. The extraction of R requires precise L-T separations with excellent control of point-to-point systematic uncertainties. Figure from [2].

inclusive electron scattering at $x > 1$ to access contributions of "superfast" quarks to inelastic structure functions [8] and measure the relative contributions of Short Range Correlations (SRCs) in the nuclear wave function [9] (Fig. 7).

The experiments noted above are just a sample of the ~30 "standard equipment" experiments that were executed in the 6 GeV era in Hall C. Other experiments include measurements of exclusive kaon production, resonance (Δ, S_{11}) production, color transparency via pion electroproduction, and numerous inclusive electron scattering measurements using hydrogen and deuterium, as well as heavier nuclear targets. In some cases, the HMS was paired with dedicated equipment for special measurements. Examples of this include measurement of the ratio of elastic proton form factors (G_E/G_M) to large Q^2, as well as measurements using a dynamically polarized NH_3 target.

1.3. Hall C 12 GeV Program

The new, Super-High Momentum Spectrometer was designed to build on the experimental capabilities exploited during the Hall C program at lower energies. Notably, this includes:

1. Excellent kinematic control and reproducibility.
2. Thorough understanding of spectrometer acceptance.
3. Small angle capability (down to 5.5 degrees) for detection of forward mesons.
4. Central momentum up to (nearly) the maximum beam energy accessible in Hall C.
5. In-plane and out-of-plane acceptance well matched to the existing HMS to facilitate experiments detecting two particle in coincidence.

Several "commissioning" experiments were chosen for the first year of 12 GeV running in Hall C to exercise the above requirements as much as possible. These experiments ran in 2018 and will be discussed briefly below.

The first commissioning experiment was a measurement of inclusive electron scattering cross sections from hydrogen and deuterium [10] (see Fig. 8). Such a cross section experiment is an excellent testing ground for understanding of the spectrometer acceptance, while not pushing the SHMS performance in other areas. Some settings for this experiment were chosen to allow simultaneous measurement with the well-understood HMS to provide a cross section. In addition, some time was devoted to the measurement of inclusive cross section ratios for nuclear targets relative to deuterium [11]. These ratios are well-measured for certain nuclei and serve as another straightforward verification of the spectrometer acceptance due to the need to compare yields from extended (10 cm long) targets to shorter, solid targets (mm scale). These measurements resulted in the first extrac-

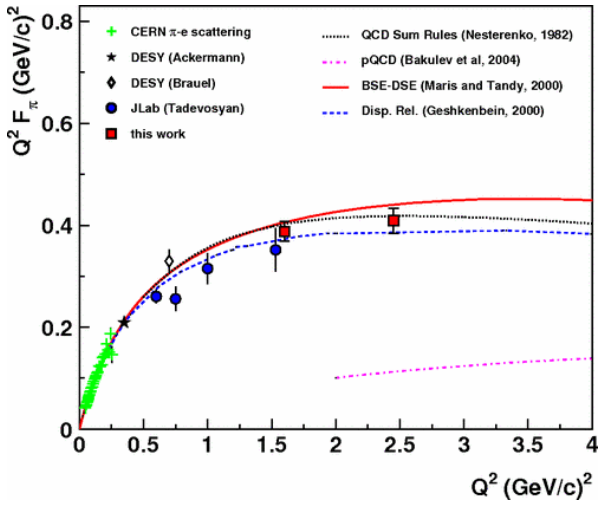

Figure 4: Measurements of the charged pion form factor in Hall C (6 GeV era). Extraction of the pion form factor requires a precise L-T separation, as well as detection of the charged pion at small forward angles. Figure from [4].

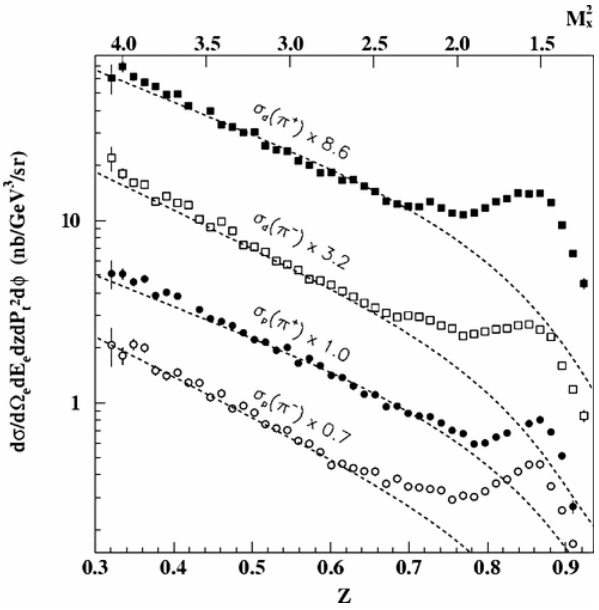

Figure 5: Cross sections for semi-inclusive π^+ and π^- production from hydrogen and deuterium. The cross sections are compared to a parameterization that uses fragmentation functions fit to high energy e^+e^- collisions. Figure from [5].

tion of the EMC Effect in ^{10}B and ^{11}B [12].

An extension of the 6 GeV color transparency experiments to larger Q^2 [13] served as an excellent first experiment with which to exercise the SHMS in coincidence mode. In this $A(e,e'p)$ experiment, there are few random coincidences. so isolating the coincidence reaction is straightforward. This experiment, as well as a measurement of deuteron electro-disintegration [14], also tested the high momentum capabilities of the SHMS. The SHMS was used at momenta larger than 8.5 GeV/c for these experiments. Although the maximum central momentum of the SHMS is almost 11 GeV, 8.5 GeV/c was already sufficient to learn about the performance of the superconducting magnets and spectrometer optics when pushed to a significant fraction of the spectrometer's ultimate capabilities. In addition, the body of $H(e,e'p)$ data acquired for both these initial coincidence experiments served to provide constraints on the experiment kinematics, allowing one to test the possible variation of, *e.g.* the spectrometer pointing or central momentum for various settings. Results from the color transparency and deuteron electro-disintegration experiments are shown in Figs. 9 and 10.

A set of meson electroproduction experiments followed the initial commissioning experiments and further exercised the SHMS capabilities. Two of the experiments measured charged pion electroproduction in semi-inclusive deep inelastic scattering, SIDIS [17, 18]. The SHMS was used at central angles smaller than 7° for the SIDIS running. An additional challenge was the relatively high singles rates in the SHMS. Both experiments aimed to make precise measurements of π^+/π^- ratios, so control of rate dependent systematic effects is a key challenge. The third experiment [19] measured exclusive cross sections for K^+ production above the resonance region, in particular, extracting the longitudinal and transverse cross sections via a Rosenbluth separation. In this case, the experimental uncertainties are expected to be dominated by statistics, so this serves as an excellent candidate for a first L-T separation,since the systematic requirements are less stringent. In common with the charged pion SIDIS experiments, the kaon experiment required use of the SHMS at small angles and had to face the challenge of high singles rates.

The "commissioning" and "year-1" experiments described above give a sense of the SHMS capabilities important for the overall physics program. Since then, a variety of experiments have been completed in Hall C. These include measurements of J/Ψ photoproduction [20], virtual Compton scattering [21], exclusive charged pion electroproduction to extract the pion form factor and for cross section scaling tests [22], inclusive electron scattering from polarized ^{3}He to extract A_1^n and d_2^n [23, 24], and exclusive and inclusive scattering from nuclei to make measurements of short range correlations and the EMC Effect [25, 26, 11]. In the future, additional L-T separations in inclusive scattering (to mea-

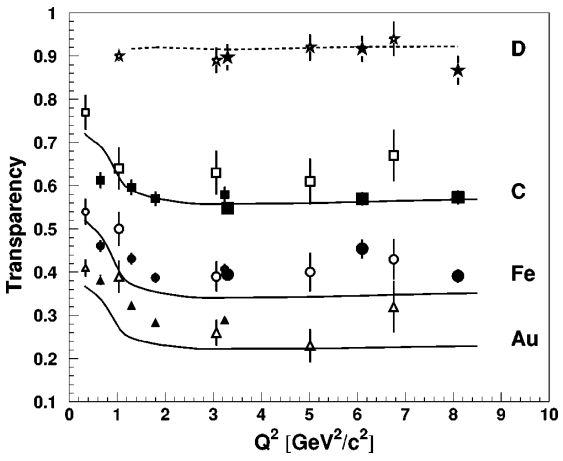

Figure 6: Measurement of transparency for $(e, e'p)$. Solid points are from (6 GeV era) Hall C measurements [6, 7]. At the largest Q^2, the HMS momentum is > 5 GeV. Figure from [7].

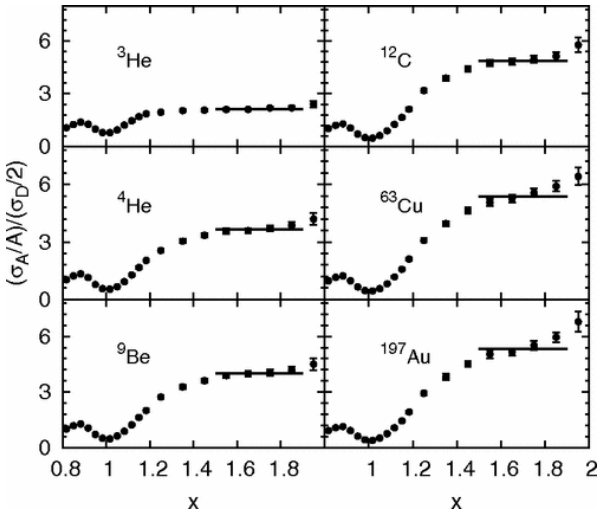

Figure 7: Measurements of cross section ratios for nuclear targets relative to deuterium at $x > 1$. The size of the ratio is proportional to the relative contributions of 2-nucleon Short Range Correlations to the nuclear wave function. These measurements required high momentum in the HMS. Figure from [9].

sure $R = \frac{\sigma_L}{\sigma_T}$ from hydrogen, deuterium, and several nuclei) and semi-inclusive reactions (to make the first precise measurement of R for the SIDIS reaction) are also planned. While not all future experiments will make use of the SHMS, it is a key component of the Hall C 12 GeV experimental program.

2. Specifications for the upgraded Hall-C Spectrometer complex

The physics outlined in the previous section can be accessed only if the Hall C spectrometer system is capable of providing the necessary measurements with precision, rate, and trigger capabilities consistent with those physics goals. Originally, Hall C offered the 7.4 GeV/c High Momentum Spectrometer (HMS) and its lower-momentum (1.8 GeV/c) partner, the Short-Orbit Spectrometer (SOS). These two devices were utilized independently by some experiments and in coincidence by others. The performance specifications for the SHMS were drafted such that the SHMS-HMS pair would provide similar complementary functions in the higher-momentum regime. That is, the SHMS was developed as a general-purpose spectrometer with properties similar to the existing HMS, but with a higher maximum momentum capability (11 GeV/c). The 11 GeV/c limit of the SHMS was selected because the accelerator constrained maximum beam energy to any of the first generation endstations (A, B, C) is 11 GeV/c. Table 1 summarizes the demonstrated performance of the HMS and the design specifications for the SHMS.

With the higher beam energies in use at Jefferson Lab after the 12 GeV upgrade, scattered electrons and secondary particles are boosted to more forward directions. Thus the SHMS acceptance is made to extend down to a 5.5° scattering angle, and needs to cover angles no higher than 40°. Nevertheless, high energies generally lead to smaller cross sections. Therefore precision experiments can be performed only if a spectrometer provides large overall acceptance, high rate capability, and precise momentum measurement. As shown in Table 1, the SHMS design includes a momentum bite even larger than the HMS, and achieves an angular acceptance within a factor of two of its low-energy partner. The combination of dispersive optics and precision tracking provides excellent momentum resolution. Triggering, data-acquisition, and particle identification rates are the same or better than those of the HMS. This performance is achieved not only through the use of faster, modern electronics, but also by innovative radiation shielding that reduces the background flux seen by the detectors.

3. Design and Development of the SHMS Systems

In this section we present design details and data demonstrating the performance of each the SHMS subsystems. The entire spectrometer is carried on a steel support structure which can rotate through an arc on the left side of the beam-line in Hall C. Like the HMS carriage, it is secured to a central pivot so that it rotates

Parameter	***HMS Performance***	***SHMS Specification***
Range of Central Momentum	0.4 to 7.4 GeV/c	2 to 11 GeV/c
Momentum Acceptance	±10%	-10% to +22%
Momentum Resolution	0.1% – 0.15%	0.03% – 0.08%
Scattering Angle Range	10.5° to 90°	5.5° to 40°
Target Length Accepted at 90°	10 cm	25 cm
Horizontal Angle Acceptance	±32 mrad	±18 mrad
Vertical Angle Acceptance	±85 mrad	±45 mrad
Solid Angle Acceptance	8.1 msr	4 msr
Horizontal Angle Resolution	0.8 mrad	0.5 – 1.2 mrad
Vertical Angle Resolution	1.0 mrad	0.3 – 1.1 mrad
Target resolution (y_{tar})	0.3 cm	0.1 - 0.3 cm
Maximum Event Rate	4–5 kHz	4–5 kHz
Max. Flux within Acceptance	~ 5 MHz	~ 5 MHz
e/h Discrimination	>1000:1 at 98% efficiency	>1000:1 at 98% efficiency
π/K Discrimination	100:1 at 95% efficiency	100:1 at 95% efficiency

Table 1: Demonstrated Performance of the HMS and Design Specifications for the SHMS. Resolutions are quoted at 1 sigma.

around a vertical axis that intersects the electron beamline at the experimental target. This is shown in Fig. 11.

Acceptance at the smallest scattering angles is enabled by the presence of a horizontal-bending dipole as the first element in the magnetic optical system. This small deflection moves the subsequent pieces of the SHMS farther from the beamline, relaxing the size constraints on the other magnetic elements (described in Section 3.1) and shielding (Section 3.2). The shielded enclosure is itself a technically-optimized combination of concrete, lead, boron, and plastic. It surrounds the detectors and the electronics of the control and data-acquisition systems.

Basic trigger information comes from four planes of scintillator or quartz-bar hodoscopes. Tracking is provided by twelve planes of conventional drift chambers, and particle identification uses gas and aerogel Cherenkov counters, a preshower counter, and a total-absorption shower counter. The detector system details are presented in Sec. 3.3– 3.9. Details of the event-triggering schemes, the data-acquisition system, and software appear in Secs. 4 and 5. The performance of the detector subsystems is discussed in Sec. 6.

3.1. Magnetic Optics

The SHMS consists of five magnets used to determine the momentum, angles and position of particles scattered from the target using their angle and position measurements by the SHMS detectors. The first is a dipole magnet which bends the incident particles in the horizontal plane. A quadrupole triplet provides a point-to-point focus. To optimize acceptance in the vertical scattering plane, the first quadrupole focuses in the vertical while the second quadrupole defocuses and the third quadrupole focuses. A vertical-bending dipole magnet follows the last quadrupole and disperses particles with different momenta across the focal plane. In point-to-point optics, all particles with the same momentum will be displaced by the same vertical distance in the focal plane.

3.1.1. The Magnets and Vacuum Channel

A specially-designed horizontal-bend dipole (HB) precedes the first quadrupole. Its purpose is to provide an initial 3° separation between scattered particles and the electron beam so that particles scattered at small angles can be accepted.

As shown in Fig. 11, in order to fit within the space available in Hall C the SHMS must be even shorter than its lower-momentum partner, the HMS. All of the SHMS magnets are superconducting so that they can provide the necessary large bending and focusing effects in short distances. Given the small-angle acceptance requirement, the HB and the first two quadrupoles (Q1 and Q2) must have special provisions to provide clear-

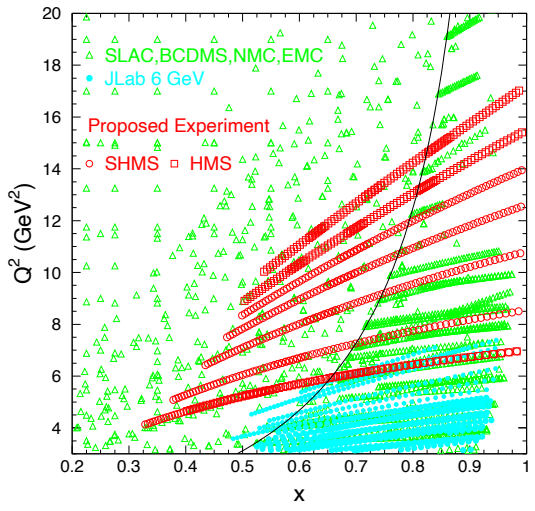

Figure 8: Kinematic coverage of F_2 measurements from experiment E12-10-002 [10], which measured inclusive electron scattering cross sections as part of Hall C's 12 GeV commissioning experiments.

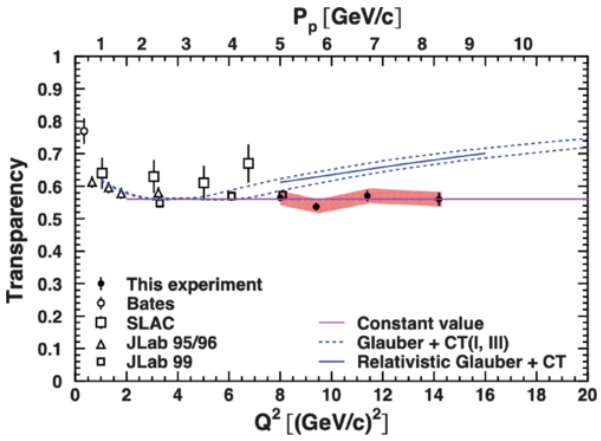

Figure 9: Results from experiment E12-06-107, a measurement of color transparency to large Q^2 [15] (Hall C commissioning experiment). This measurement served as the first coincidence measurement in the 12 GeV era in Hall C.

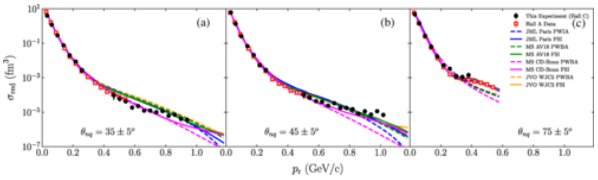

Figure 10: Results from experiment E12-10-003, a measurement of deuteron electro-disintegration at large missing momentum [16] (Hall C commissioning experiment).

ance for the electron beam and its vacuum pipe. HB is a "C"-magnet so that all of the flux-return iron is on the side away from the beamline. As initially constructed, the HB leaked significant field into the beamline such that the beam would have been deflected outside of the beam dump. Simulations were done to determine the optimal shielding design to reduce the field in the beamline region for all combinations of SHMS angle and momentum and these remediation were implemented [27]. The front of the HB cryostat, between the beamline and the magnet bore, is made very narrow. Both Q1 and Q2 have notches in their cryostats and iron yokes so that they, too, can clear the beamline when the spectrometer is configured at small scattering angles. Yoke steel for Q1 is inside the cryostat. The final quadrupole (Q3) and the dipole (D_{SHMS}) have external warm yokes. Parameters of the SHMS magnets are provided in Table 2.

To minimize multiple scattering as particles pass through the SHMS, the bores of all of the magnets are evacuated. The vacuum space begins at a window on the front of HB. The entrance window into the HB is approximately 15 cm square and is made of 0.01" thick aluminum. A vacuum connection is made between the exit of HB and Q1 entrance which is followed by the 40 cm diameter vacuum bore in Q1. The exit of Q1 is connected to the entrance of Q2 by a vacuum pipe. The vacuum vessel bore through Q2, Q3, and D_{SHMS} is 60 cm in diameter. The location of the end of the vacuum after the exit of D_{SHMS} depends on the needs of the experiment. If the experiment needs the Noble Gas Cherenkov (NGC) detector (described in Sec. 3.7), then a window is placed at the exit of D_{SHMS} with the NGC detector placed between the exit window and the drift chambers. Otherwise, a Vacuum Extension Tank (VET) is attached to the exit of the D_{SHMS} that puts the exit window at 30 cm from the first drift chamber in the detector stack. In both cases, the dipole exit window is made of 0.020" thick aluminum.

3.1.2. Optics

The relative strengths of the integral fields of the magnets are set to maximize acceptance while at the same time optimizing resolution in momentum and scattering angle. The transport of a particle with the relative momentum, $\delta = \frac{p-p_c}{p_c}$, from the target to midway between the two set drift chambers in the focal plane of the SHMS can be characterized by an optics matrix. The particle momentum is p and the central momentum of the spectrometer is p_c. The particle starts with the vertical and horizontal positions (x_{tar} and y_{tar}) and angles ($x'_{tar} = \frac{\Delta x_{tar}}{\Delta z_{tar}}$ and $y'_{tar} = \frac{\Delta y_{tar}}{\Delta z_{tar}}$) in the $z_{tar} = 0$ plane. These positions and angles are measured relative to the central ray of the spectrometer. After magnetic transport, it ar-

Parameter	*HB*	*Q1*	*Q2*	*Q3*	D_{SHMS}
Max Field or Gradient	2.6 T	7.9 T/m	11.8 T/m	7.9 T/m	3.9 T
Effective Field Length	0.80 m	1.9 m	1.6 m	1.6 m	2.9 m
Current at 11 GeV/c	3923 A	2322 A	3880 A	2553 A	3510 A
Aperture	14.5x18 cm	40 cm	60 cm	60 cm	60 cm

Table 2: Parameters of the SHMS Magnets

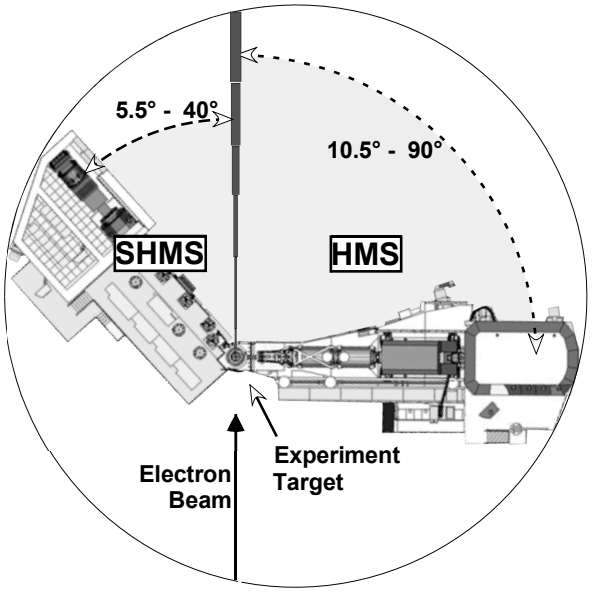

Figure 11: Simplified Plan View of Hall C showing the footprints of the SHMS and HMS. The SHMS occupies the smaller side of Hall C, where the smaller, low-momentum Short-Orbit Spectrometer (SOS) had been previously located.

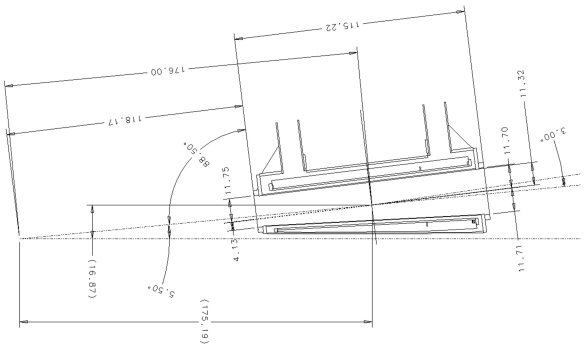

Figure 12: Top view schematic of the horizontal bender (HB) magnet with dimensions given in units of cm. The center of the HB magnet is at 5.5° for the beam line and 176 cm from the hall center.

rives at the focal plane with the vertical and horizontal positions (x_{fp} and y_{fp}) and angles (x'_{fp} and y'_{fp}). The first order optics matrix is

$$\begin{pmatrix} x_{fp} \\ x'_{fp} \\ y_{fp} \\ y'_{fp} \end{pmatrix} = \begin{pmatrix} -1.5 & 0.0 & 0.0 & 0.0 & 1.65 \\ -0.5 & -0.7 & 0.0 & 0.0 & 3.2 \\ 0.0 & 0.0 & -1.9 & -0.2 & -0.1 \\ 0.0 & 0.0 & -3.0 & -0.8 & 0.1 \end{pmatrix} \begin{pmatrix} x_{tar} \\ x'_{tar} \\ y_{tar} \\ y'_{tar} \\ \delta \end{pmatrix} \quad (1)$$

The units of the positions, angles and δ are in centimeters, milliradians and %.

The acceptance of the spectrometer is mainly determined by the collimator that is placed between the HB magnet and the first quadrupole. A remotely-operated collimator box is installed on the SHMS between the HB and Q1 magnets. The collimator ladder assembly within this box may be positioned at three settings. The top position (accessed when the assembly is at its lowest position) is a stretched octagon with opening height 9.843" and width 6.693" on the upstream side. It is 2.5" thick. The lower two positions both present sieve holes in rectangular pattern with holes separated by 0.6457" horizontally and 0.9843" vertically. The sieve pattern at the middle ladder position has 11 columns of holes with the sixth column centered horizontally. The holes on the bottom sieve are in ten columns and are offset by one-half a column gap from those in the middle sieve. The sieve collimators are 1.25" thick. The geometry is illustrated in Fig. 13. Both sieves and octagonal collimator are made of Mi-Tech™ Tungsten HD-17 (Density 17 g/cc. 90% W, 6% Ni, 4% Cu).

To determine the vertical size of the collimator studies were done with SNAKE (magnet transport code). Without the collimator, the vertical acceptance is mainly determined by the mechanical exit of the HB magnet. The vertical size of ±12.5 cm was chosen to match this vertical cut-off to maximize the acceptance. Two vertical sizes of ±8 cm and ±10.5 cm for the collimators were studied. A plot of the acceptance of each collimator versus δ is shown in Fig. 14. The acceptance drops from an average of 4 msr for ±12.5 cm to an average of 3 msr for ±8 cm. Another consideration is minimizing the loss of events in the bore of the vertical dipole after they pass the entrance of the dipole. A plot in Fig. 14

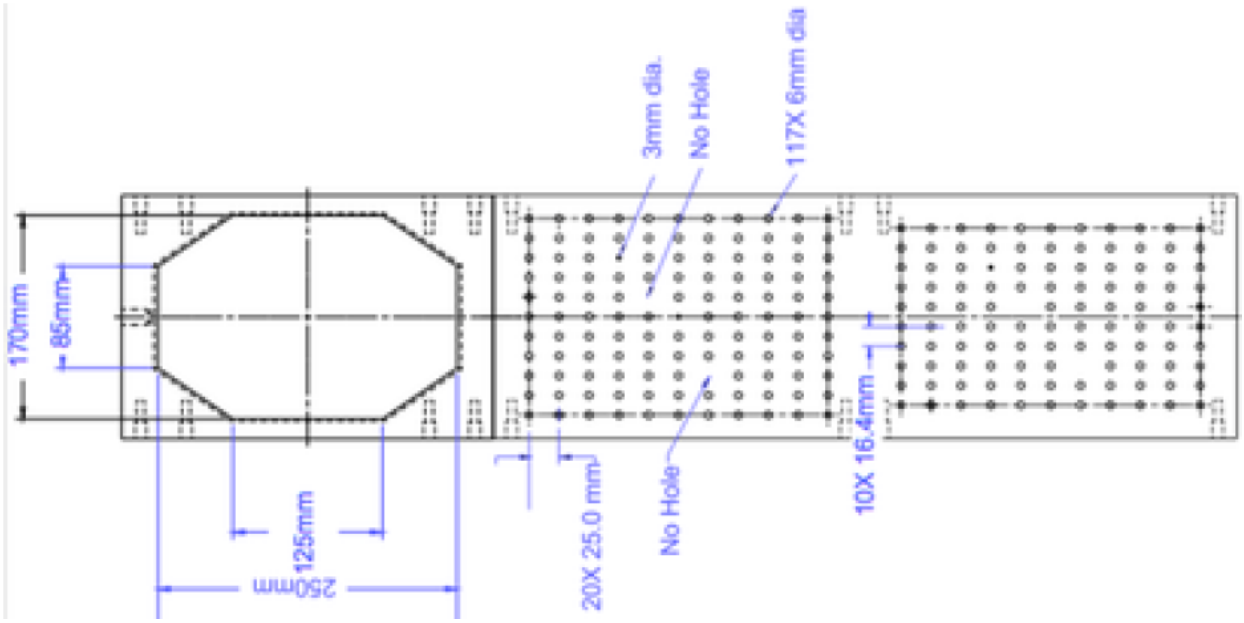

Figure 13: Schematic diagram of the SHMS collimator.

shows the fraction of events which make it to the focal plane. The number of events lost in the dipole bore as a function of δ is reduced by decreasing the vertical height of the collimator. With the ± 12.5 cm collimator, the fraction of events making to the focal plane drops to 75% at $\delta = 0.15$. The decision was made to use the ± 12.5 cm vertical opening to maximize the solid angle acceptance of the SHMS at the expense of increased reliance on the understanding the losses in the SHMS dipole bore.

SNAKE was also used to model the acceptance of the SHMS. The mechanical sizes of the magnets and magnet field maps from TOSCA are used to create a model of the SHMS in SNAKE. The acceptance of the SHMS versus δ determined by SNAKE is plotted in Fig. 15. A separate calculation is done using the Hall C Monte Carlo (SIMC) simulation which uses the COSY transport matrix. The acceptance of the SHMS versus δ determined by SIMC is also plotted in Fig. 15. As seen in this figure, the agreement between the two calculations is excellent.

The reconstruction of a particle's momentum, horizontal target position, vertical and horizontal angles from the focal plane positions and angles can also be represented by an optics matrix. Each event calculates the target interaction point from the tracks reconstructed in the focal plane using the drift chamber information. Target offsets, beam offsets and spectrometer mis-pointings are accounted for separately when reconstructing events. The optics matrix elements consist of a set of coefficients and the values of the powers for each focal plane element. The coefficients for each focal plane variable are X', Y, Y', and D, and the powers of each focal plane variable are represented by $ijklm$. The powers for each term range from zero to six with the sum of the powers for a given term not exceeding six. The reconstruction equations for the target quantities are written as shown in Eq. 2.

$$
\begin{aligned}
x'_{tar} &= \sum_{ijklm} X'_{ijklm} x^i_{fp} x'^j_{fp} y^k_{fp} y'^l_{fp} x^m_{tar} \\
y_{tar} &= \sum_{ijklm} Y_{ijklm} x^i_{fp} x'^j_{fp} y^k_{fp} y'^l_{fp} x^m_{tar} \\
y'_{tar} &= \sum_{ijklm} Y'_{ijklm} x^i_{fp} x'^j_{fp} y^k_{fp} y'^l_{fp} x^m_{tar} \\
\delta &= \sum_{ijklm} D_{ijklm} x^i_{fp} x'^j_{fp} y^k_{fp} y'^l_{fp} x^m_{tar}
\end{aligned}
\tag{2}
$$

From Eq. 2, it can be seen that the target reconstruction is actually under-determined. For each event, there are four given quantities (x_{fp}, y_{fp}, x'_{fp}, y'_{fp}) and five unknowns to solve for (x_{tar}, y_{tar}, x'_{tar}, y'_{tar}, and δ). x_{tar} is never directly measured, but it is reconstructed with the knowledge of the beam position and reconstructed values of y_{tar}, x'_{tar}, y'_{tar}. The x_{tar} dependent coefficients are used directly from COSY calculations with the reconstructed x'_{tar} and δ being most sensitive to knowledge of

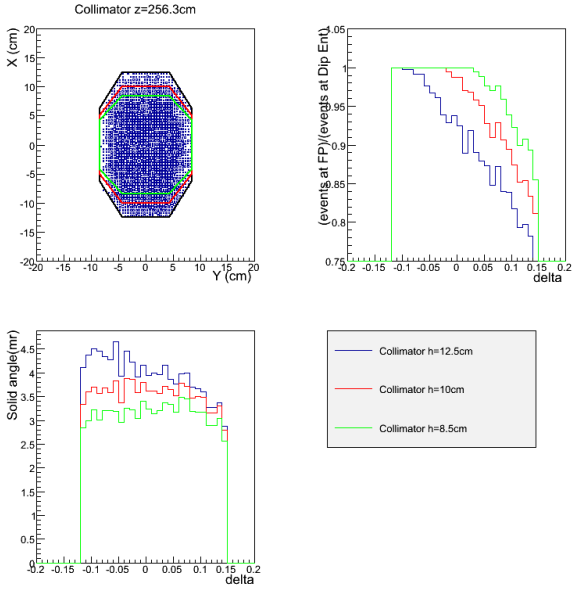

Figure 14: The upper left figure is distribution of events at the location of the collimator with three different vertical size collimators. The lower left figure is the acceptance as a function of δ for each of the collimators. The upper right figure is the fraction of events lost in the dipole bore after the dipole entrance.

x_{tar}. To account for x_{tar}, an iterative procedure is done where first the y_{tar}, x'_{tar}, y'_{tar} and δ are calculated by setting x_{tar} equal to the vertical beam position. Then x_{tar} is calculated using the vertical beam position, y_{tar}, x'_{tar} and y'_{tar} and the reconstruction matrix is recalculated with the new x_{tar}. This is repeated in a loop until the change in x'_{tar} compared to the previous iteration is less than 2 mrad for no more than five iterations.

The determination of x_{tar} independent coefficients (when $m = 0$ in Eq. 2) in the reconstructed matrix elements was done using data from specific run settings. In all cases, a single or multi-foil carbon target is used with a sieve installed downstream from the target. For each interaction that pass through a sieve hole, all true target quantities, including x_{tar}, can be calculated from knowledge of the beam position, foil location and sieve hole location.

The calibration of the δ matrix elements was done using carbon elastic data. Using the first order optics from COSY and selecting events from a carbon target interaction that pass through a single hole in the sieve, the carbon elastic peak and excitation spectrum is clearly seen as shown in Fig. 16.

The carbon energy spectrum shows the elastic peak and the 4.4 MeV carbon excited state. Additional carbon states are observable in the smaller peaks to the right of the 4.4 MeV peak. The δ matrix elements were optimized by taking a series of runs where the carbon elastic peak moved across the focal plane for incremental settings of the spectrometer central momentum.

The optimization of the reconstructed target quantities y_{tar}, y'_{tar}, and x'_{tar} used data from multi-foil carbon targets with the sieve inserted in the beam line. Each hole in the sieve is used to define the true physical values of an event and is compared to the reconstructed angles and positions for optimization. The reconstructed y_{tar} is approximately $z_{tar} \sin\theta$ where θ is the central angle of the spectrometer, and z_{tar} is the target foil position in the hall beam line coordinate system. To optimize over the full range of possible y_{tar} values, data must be taken with the spectrometer at various central angles. Two sieves were used to collect the data having the same hole

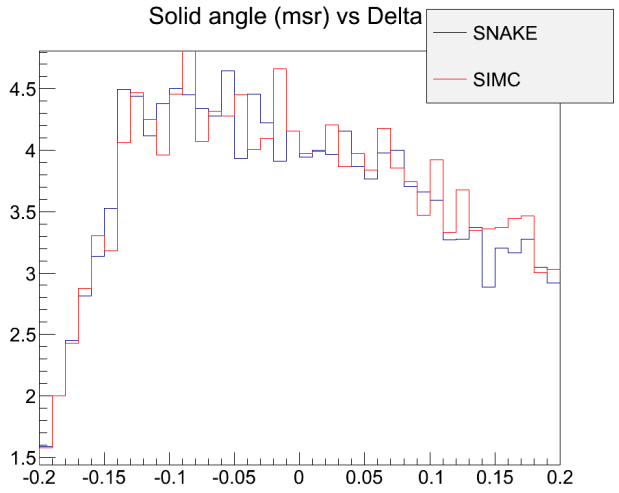

Figure 15: Comparison of predicted SHMS acceptance using the Hall C Monte Carlo (SIMC) and the magnetic transport code SNAKE.

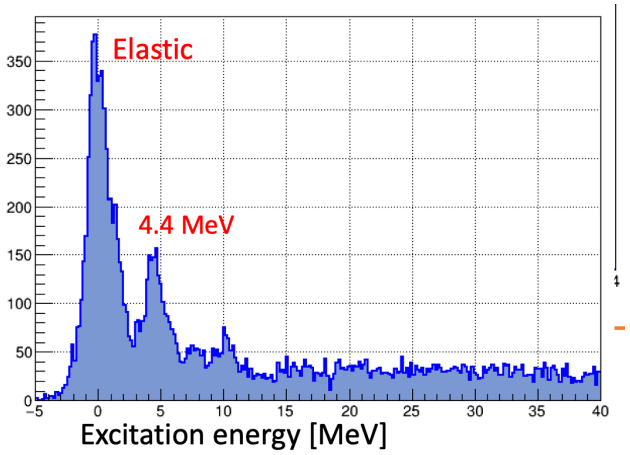

Figure 16: The carbon elastic energy spectrum for events for a single sieve hole, as calculated in terms of delta from the first order optics, clearly shows the carbon elastic peak and the 4.4 MeV excited state.

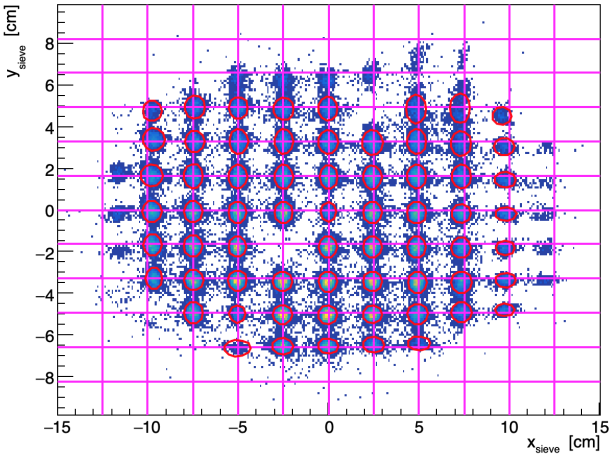

Figure 17: The sieve pattern is reconstructed here where the true sieve hole positions are indicated by the magenta cross lines and the reconstructed holes are outlined in red. The holes at the edges of the sieve are somewhat shifted from the true desired values.

patterns: one where the central hole was centered on the spectrometer axis and the other where the central hole was shifted by half the distance between the holes relative to the spectrometer axis. Data was taken with each sieve separately in order optimize the full spectrometer acceptance. A reconstructed sieve pattern using a single carbon foil is shown in Fig. 17.

The general procedure for the optimization of the target quantities y_{target}, y'_{target}, and x'_{target} is as follows: the events are initially reconstructed using the original reconstruction matrix elements generated from the COSY model. These events are used to determine the true physical values by determining which target foil an event originated from and which sieve hole the event passed through. The differences between the measured events and the real true physical values are minimized by solving a Singular Value Decomposition (SVD) to calculate the optimized/improved reconstruction matrix

elements. In operation, the SHMS has achieved angular resolutions of $\sim 0.9\,mrad$ in the horizontal direction and $\sim 1.1\,mrad$ in the vertical direction.

3.2. Shield House Layout, Shielding Design

The radiation environment is an important consideration for the design of the SHMS shield house, in particular, the effect of radiation-induced effects on the performance and reliability of detectors and electronics. It has been shown that many new commercial off the shelf components are sensitive to radiation damage and single event upsets, requiring a careful evaluation of the impact of the radiation-induced effects on their performance and reliability [28, 29]. A specialized SHMS shield house design was thus developed at Jefferson Lab. Shielding thicknesses were optimized using a Monte Carlo simulation and benchmarked against the HMS shielding house, which has been proven to provide the necessary detector shielding over more than a decade of experiments at the 6 GeV JLab. A full description of the shielding optimization can be found in Ref. [30].

The primary particle radiation is created when the CEBAF electron beam strikes the experimental target. The main components are scattered electrons, neutral particles (photons and neutrons), and charged hadrons. The energy spectrum of this radiation depends on the incident beam energy and decreases generally as $1/E$. It has been shown that the most efficient way to protect the experimental equipment from radiation damage is to build an enclosure around it using certain key materials. The type and thickness of the shield house walls depends on the energy and particle one needs to shield against. However, one may qualitatively expect that the largest amount of shielding material is needed on the side facing the primary source, which in the case of the Hall C focusing spectrometers is the front face. Additional sources of radiation are the beampipe, which extends from the experimental target to the beam dump, and the beam dump area itself. Thus, the faces of the spectrometer exposed to direct sources of radiation are the front, beam side, and the back walls.

Primary and scattered electrons lose a significant amount of energy as they traverse a material by producing a large number of lower energy photons through bremsstrahlung [31]. It is thus important to consider shielding materials that efficiently stop the latter as well.

Neutral particles have a higher penetration power than charged particles. They are attenuated in intensity as they traverse matter, but do not continuously lose energy. Photons interact in materials almost exclusively with electrons surrounding the atom or by pair production in the field of the nucleus. The probability for an interaction depends on the atomic number of the material. Neutrons interact with atomic nuclei in a more complicated way.

An additional source of radiation is due to charged hadrons (e.g. protons, pions). However, the probability for producing hadron radiation is relatively low, and thus will be neglected here. The shielding is, nevertheless, effective for charged hadrons. The front wall will, for instance, stop 1 GeV protons.

Fig. 18 shows a schematic of the SHMS shielding plan. The SHMS shield house is similar to the HMS design, but has several new features due to additional requirements. For example, the space between the beam side shield wall and the beam pipe is limited at very forward angles, and in addition, the length of the SHMS detector stack and minimum distance between the back of the detector house to the hall wall requires a reduction in thickness of the concrete shield wall.

Typical beam-target geometries were simulated using Monte Carlo techniques. Simulations were performed using the GEANT MCWORKS distribution, which includes detailed physical and geometric descriptions of the experimental hall and simulates the physics processes using standard GEANT3 together with the DINREG nuclear fragmentation package. Hadronic interactions are treated using the DINREG package, which calculates the probability of such interactions using a database of photonuclear cross sections. For electron-nucleus interactions an "equivalent photon" representation of the electron (or positron) is used.

In this simulation, the CEBAF beam electrons start 1 m upstream of the target, strike it head-on along the cylindrical symmetry axis, and have no momentum component transverse to the beamline. The simulation also includes the beam pipe, target entrance and exit windows, and the entire geometry of Hall C, including all elements of the beam dump. The transmission of particles through the shielding materials was calculated as a function of the material thickness and the angle relative to the beam direction.

A limitation of the radiation studies is the lack of cross section data for low-energy neutrons. The accuracy of the GEANT simulations was tested by benchmark calculations using the MCNP code [32] with an isotropic neutron point source of 1 MeV located 1 m from the shield wall. The MCNP calculations suggest that 50 cm of concrete thermalizes most of the fast neutrons, and after 1 m practically no epithermal neutrons remain. The thermalized neutrons can be captured by a 1 cm Boron layer. In reality, however, the neu-

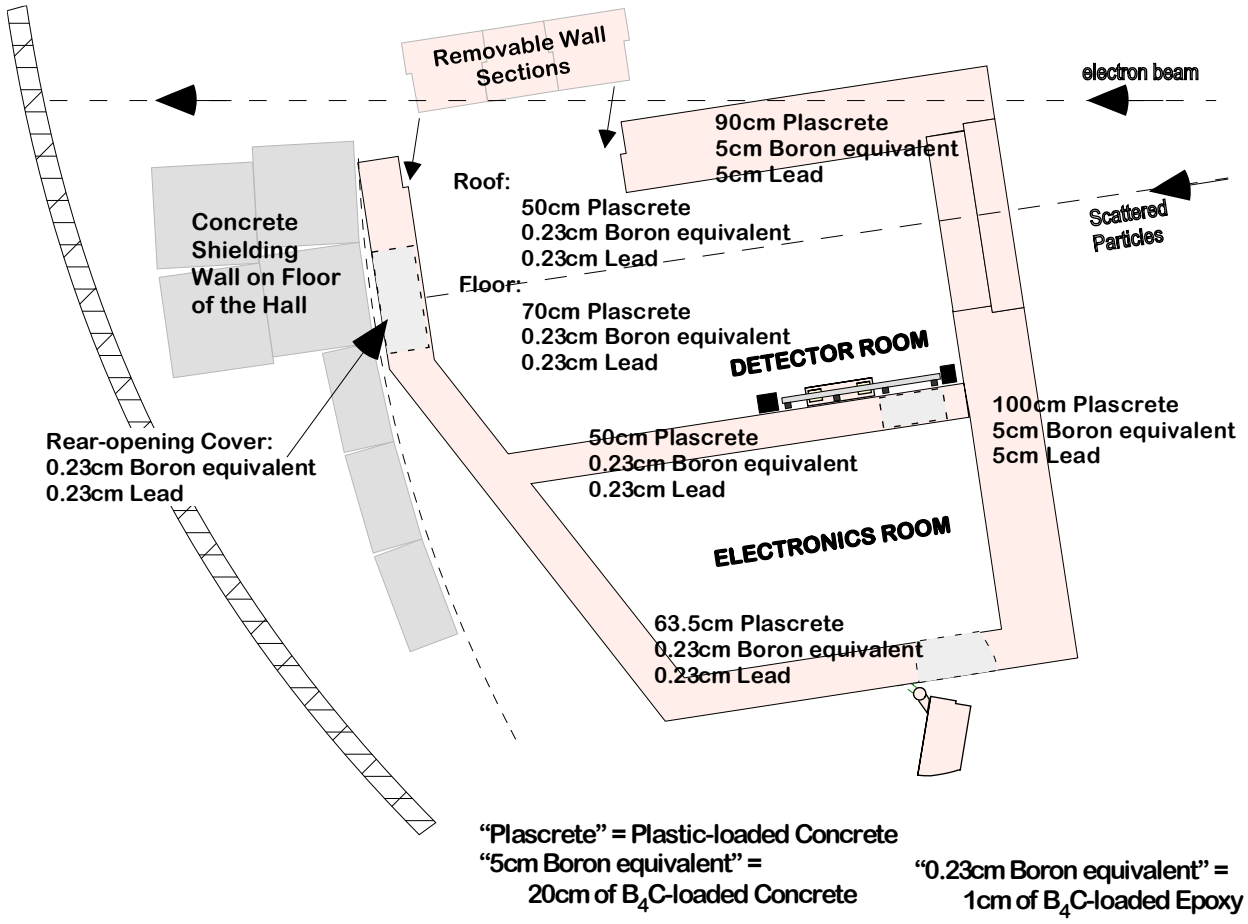

Figure 18: Plan View of the SHMS Shield House showing the layout, thickness, and composition of the walls.

tron spectrum also includes higher energy neutrons, for instance produced by electrons interacting in the concrete, and thus the actual amount of material for the walls exposed to the primary sources of radiation has to be thicker. A simple transmission calculation using GEANT4 for incident neutron beams of energies between 1 and 10 MeV suggests that a thickness 150 cm of concrete is sufficient to stop the majority of low-energy neutrons.

The SHMS shielding model is composed of standard concrete ($\rho = 2.4\,\mathrm{g/cm^{-1}}$). The thickness of the wall in front of the detector and electronics rooms is 200 cm, to shield from the primary radiation source around the target. Figure 19 shows the surviving background flux for varying front wall concrete thicknesses. The results are normalized to the background flux in the HMS at 20°. This angle was chosen as experiments in Hall C have shown that electronics problems seem to dominate at lower angles. The simulation results suggest that 200 cm of concrete reduces the total flux to half of the HMS at 20°.

Figure 20 shows the energy spectra for surviving photons and neutrons with varying front wall thickness. In order to optimize the shielding, these secondary particles have to be absorbed as well. Our assumption on radiation damage is that photons below 100 keV will not be a significant source of dislocations in the lattice of the electronics components, while neutrons will cause radiation damage down to thermal energies. Adding lead to the concrete wall reduces the photon flux significantly, but it does not help for neutrons. On the other hand, the boron reduces the flux of very low energy neutrons. Assuming that low energy photons and neutrons cause a significant fraction of the radiation damage, then adding the relevant material would be important.

The thickness of the beam-side wall (shielding from an extended source, the beamline) is constrained by the clearance with the detector stack inside the enclosure

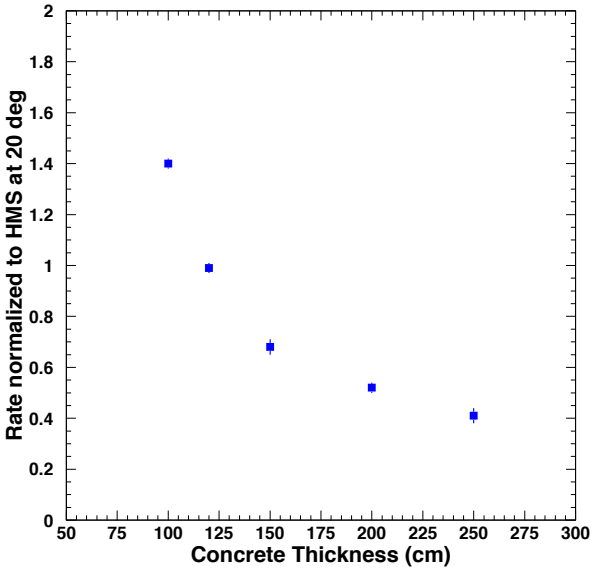

Figure 19: The normalized background rate vs. front wall thickness based on simulations described in the text. The rates are normalized to those found in the HMS at 20°.

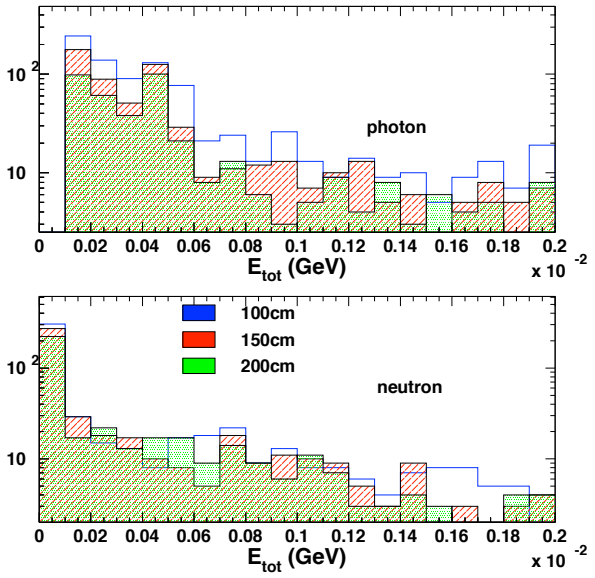

Figure 20: The outgoing particle spectrum, which is soft (< 10 MeV).

and the beamline at small angles. Conservatively assuming a clearance of 5 cm between detector stack and the shield wall, the total concrete wall thickness is limited to 105 cm. A 90 cm concrete wall combined with a 5 cm boron and 5 cm lead layer provides the optimal shielding configuration. Adding boron is not much different from adding (or replacing) concrete, but in addition it captures thermal neutrons.

The majority of charged particles are stopped by the outer walls of the spectrometer shield house. An additional source of radiation may be created from particles entering the enclosure through the magnets. In order to protect the electronics further, an intermediate wall was installed between the detector and electronics rooms. Figure 21 shows the normalized rate as the thickness of this intermediate wall is varied. This suggests that the optimal configuration is provided by a concrete thickness of 80–100 cm[1]. Further details on shielding configurations investigated and their optimization can be found in Ref. [30].

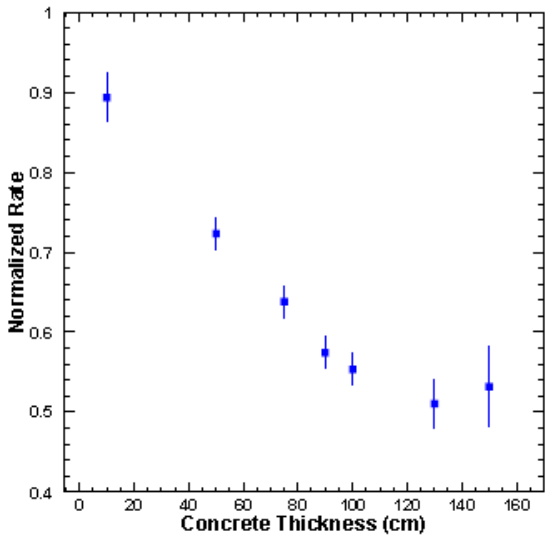

Figure 21: The normalized rate versus the intermediate concrete wall thickness.

The hydrogen-rich concrete walls function as a shield, an absorber, and a neutron moderator, and are thus placed on the outside of all faces of the shield house. On the other hand, the ordering of lead and boron to shield against the photon and neutron flux may, at first glance, not be obvious, and is discussed in detail below.

[1] Note that a minimum wall thickness of 50 cm is needed to provide support for the roof of the shield house

The incoming photon flux has two components: externally produced photons and bremsstrahlung photons produced by electrons in the twenty radiation lengths of concrete. The simulations have shown that the outgoing photon spectrum is soft (<10 MeV). Placing a lead layer after the concrete is essential to suppress this low energy photon flux. The (γ, n) reaction in lead is not a problem. The threshold for the reaction is given by the neutron binding energy ($\sim$ 8 MeV). At higher energies, the cross sections are in the mbarn range [33]. Even disregarding the low cross section, however, it is not clear that this reaction contributes to the irradiation of the electronics, because a high energy photon is replaced by a low energy (but not thermal) neutron.

The incoming neutron flux also has two components. Neutrons from excited nuclei will typically not exceed 10 MeV. The other neutrons are produced through direct interactions with only one nucleon in the nucleus. These will have high energies, but the flux is low. As shown by the MCNP calculation, which has reliable low energy neutron cross sections, 0.5 m of concrete almost fully thermalizes 1 MeV neutrons. Thus, 2 m of concrete should be sufficient to thermalize the first component. Some of these will be captured in the concrete, but to eliminate the surviving thermal neutrons a layer of boron is needed. There are two relevant reaction channels: (n, γ) and $(n, \alpha\gamma)$. The former produces high energy photons, but the cross section is relatively small. The latter produces a 0.48 MeV photon for every captured neutron. The thermal cross section is about 10 kbarn, and even at 1 MeV it is still in the barn range. The majority of neutrons can thus be expected to be captured in a sufficiently thick boron layer. An optimal shielding configuration would also stop these photons produced in the capture. At 0.48 MeV, the photoelectric effect and Compton scattering contribute about equally to the attenuation in lead. Photons from the latter will also need to be absorbed.

Thus, placing the lead in front of the boron layer has limited benefit. It will not affect the neutron flux, but will create an additional source of photons. The more lead one places after the boron, the more efficiently these photons will be suppressed. From the point of view of stopping bremsstrahlung photons, the order of boron and lead layers does not matter. Thus, all lead should be placed after the boron.

Fig. 22 is a photograph showing the resulting multi-layered shielding in one of the SHMS shield house walls. The ceiling, floor, and other walls have similar compositions but varying dimensions as shown in Fig. 18. Details about the development of custom concrete material containing boron can be found in Ref. [34].

Figure 22: Photograph of the SHMS beam-side shield wall in cross-section view, showing the layers of different materials making up the wall.

In summary, the SHMS shielding consists of concrete walls to moderate and attenuate particles. Low energy (thermal) neutrons are absorbed in a boron layer inside the concrete. Low energy and 0.5 MeV capture photons are absorbed in lead. With this design, the rates at forward angles of 5.5° are estimated to be less than 70% of the design goal (HMS at 20°) in the detector room and below 50% in the electronics room.

3.3. Scintillator Trigger Hodoscopes

The SHMS hodoscope system provides a clean trigger and trigger time information as well as the definition of the detector package fiducial area, required for physics cross section measurements. The system is composed of four separate planes of detector paddles: S1X and S1Y located immediately after the second drift chamber and S2X and S2Y approximately 2.6 m away along the z direction. The S1X, S1Y, and S2X planes were built using thin scintillator paddles while S2Y uses quartz bars.

3.3.1. Design and Construction

The overall dimensions and granularity of the three scintillator planes were driven by the Monte Carlo simulations of the SHMS acceptance. The S1X and S1Y planes cover a 1000×980 mm^2 area while the S2X plane covers 1100×1335 mm^2. Further design constraints for this detector include high ($\geq$ 99%) detection efficiency, position independent along the scintillator paddle; good time resolution ($\sim$ 100 ps) and high rate capability ($\sim$ 1 MHz/cm). As the detector's lifetime is assumed to be a decade or more stable, cost effective, readily available materials and readout chain were used.

To meet the requirements listed above, the SHMS Hodoscope was built as a series of arrays (planes) of plastic scintillator paddles. The S1X and S1Y planes have 13 1000×80 mm paddles each, while the S2X plane has 14 1100×100 mm paddles. For each of the three scintillator planes the paddles were staggered by 7 mm and overlapped by 5 mm. To minimize the impact of the scintillators on downstream detectors and also to ensure good timing resolution, the thickness of paddles was 5 mm.

The scintillator material used was Rexon `RP-408`. The paddles were wrapped by the manufacturer with millipore paper, aluminum foil, and 2" wide electrical tape. The transition between the thin scintillator material and the photomultiplier (PMT) tubes used for readout was done using a Lucite fishtail-shaped light guide. As the glued joint between the scintillator paddle and the light guide is rather fragile (5×80 and 5×100 mm joints) aluminum "splints" were used to reinforce it. The PMT to fishtail joint was originally wrapped with 2" tape as well and light-leak tested; subsequently this wrapping was reinforced with TEFLON tape and a 3" heat-shrink sleeve.

Each scintillator paddle is read at both ends by PMTs glued to the fishtail using optical glue (BC-600) matching the index of refraction of the Lucite. A combination of Photonis XP 2262 and ET 9214B 2" tubes were used. Both models have 12-stage amplification and their maximum photocathode sensitivity is in the blue–green range. The typical gain is 3×10^7. Gains were measured as a function of high voltage during the construction and the whole hodoscope was gain matched *in situ* once installed in SHMS.

3.4. Quartz-bar Trigger Hodoscope

The SHMS hodoscope quartz plane was designed to help with neutral background rejection in the 12 GeV high-rate environment. It operates on the principle of Cherenkov light production by electrically charged particles. It is one of the four hodoscope planes that form the basic 3 out of 4 trigger in the SHMS. In what follows the design and construction of this detector will be presented as well as its performance with electron beam in Hall C.

3.4.1. Design and Construction

Quartz bars of 2.5×5.5×125 cm^3 dimensions with an index of refraction of 1.5 were chosen. The Cherenkov light produced by electrically charged particles is detected by UV-glass window PMTs (model ET9814WB) quartz window ET9814QB photomultiplier tubes optically coupled to the quartz bars through RTV615 silicon rubber of 50 μm thickness. There are 16 bars in use in the hodoscope quartz plane are staggered so that there is an overlap between adjacent bars of 0.5 cm. The quartz plane frame allows for more bars to be added.

3.5. Drift Chambers

3.5.1. Design

The SHMS horizontal drift chambers provide information to determine the trajectory of charged particles passing through the detector stack. The drift chamber package consists of two horizontal drift chambers separated by a distance of 1.1 m and oriented in the detector stack such that the sense wires planes are perpendicular to the central ray. Each chamber consists of a stack of six wire planes providing information on the track position along a single dimension in the plane of the wires and perpendicular to the wire orientations to better than 250 μm. The perpendicular distance of the track relative to the wire is determined from the time of the signal produced by the ionization electrons as they drift from their production point to the wire in an electric field of approximately 3700 V/cm.

The basic design and construction technique is based on that of previous successful chambers built for the Hall C 6 GeV program, which have been shown to reach the resolutions and particle rate specifications of the SHMS. The open layout design consists of a stack of alternating wire and cathode foil planes; each plane consisting of 1/8" thick printed circuit board (PCB). These are sandwiched between a pair of aluminum plates on the outside, which provide both the overall structural support and the precise alignment of each board via dowel pins at the corners. Just inside each pair of plates is a fiberglass board with the central area cut out and covered with a vacuum stretched film of aluminized Mylar, which provides the gas window. These are sealed to prevent gas leakage via an o-ring around the gas fitting through-hole on the inside of the plate.

Each chamber consists of two identical half chambers separated by a fiberglass mid-plane, which also supports

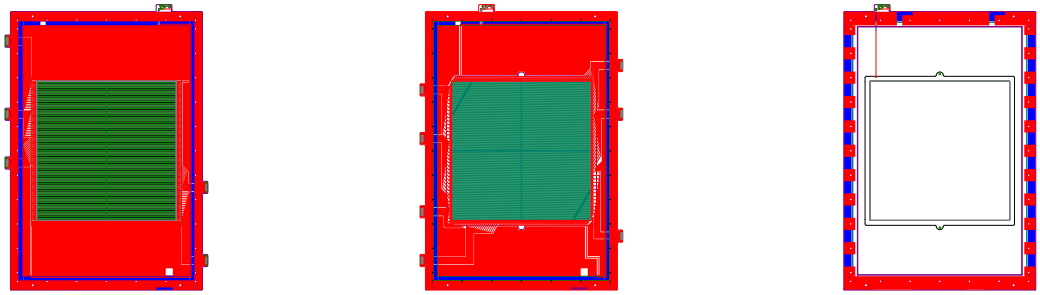

Figure 23: Technical drawings of the PCBs for the X-plane (Left), U-plane (Middle), and K-plane (Right).

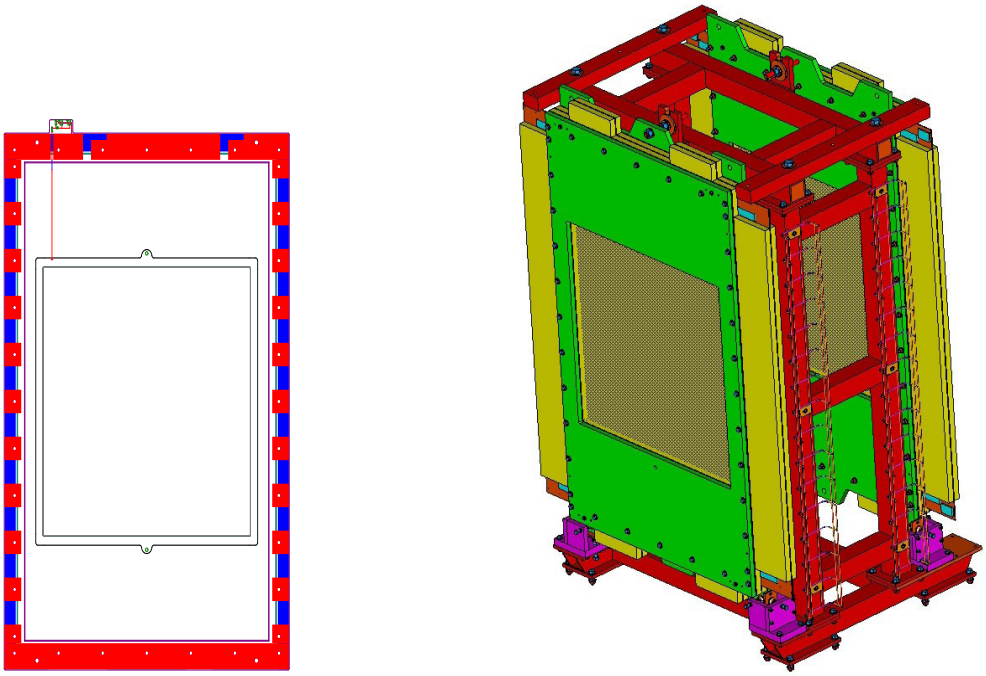

Figure 24: (Left) Technical drawing of cathode (k-plane) PCB. (Right) Technical drawing of the two drift chambers mounted in the Aluminum frame such that the scattered particles would enter the chamber from the left. The chambers are fixed to the frame by a bolt through the top tab on the chamber plate which allows for fine adjustments to the pitch. The downstream chamber (DC2) is mounted in the reverse orientation from the upstream chamber (DC1).

the amplifier discriminator cards required for the sense wire readout. To minimize the production costs, only two unique PCB types were designed: an X-plane with wires oriented horizontally (left panel of Figure 23), and a U-plane with wires oriented at +60° relative the X-plane (right panel of Figure 23). All other plane orientations are generated by rotations of these two basic board types. For instance, the boards are designed such that a rotation of 180° in-plane about an axis through the center of the board produces boards with wires of the same orientation, but shifted by 1/2 cell width, thus allowing the resolution of left/right ambiguities. Rotation of Figure 23 such that the top becomes the bottom produces the X' and U' orientations. The V and V' boards, with wire orientation of -60° relative to the X-plane, are produced by a rotation of the U and U' boards of 180° into the page about a vertical axis though the center of the board. Each half chamber has three planes with the first half consisting of (U, U', X) and the second half consisting of (X', V', V). The first chamber is oriented in the SHMS frame such that the board ordering as seen by particle traversing the spectrometer is (U, U',

X, X', V', V), while for the second chamber the ordering is reversed (V, V', X', X, U', U). A drawing showing the chambers mounted in the frame is presented in Figure 24.

The drift gas (50/50 mixture of Ethane/Argon in production mode) flows across each board through holes in the cathode planes (k-planes) alternating from top to bottom. A technical drawing of a k-plane is presented in Figure 23. The overall dimensions of the wire chambers are driven by the desired active area for particles at the focal plane of the SHMS; this has been set at 80 cm x 80 cm. The active area of each wire plane consists of alternating 20 μm diameter gold tungsten sense wires and 80 μm diameter copper plated beryllium field wires separated by 0.5 cm. Each wire plane is sandwiched between a pair of cathode planes with the cathode surfaces consisting of 5 mil thick stretched foils of copper plated Kapton.

3.5.2. Calibration

As charged particles traverse the drift chambers and ionize the gas, free electrons from the ionized gas drift towards the sense wires in the chamber. This process produces a measurable current signal in the sense wire, this signal is pre-amplified and read out by 16-channel input discriminators. The discriminators produce logic signals that are sent to the TDC which registers the time at which this signal arrives. This signal is utilised to determine the drift time, the time taken for the free electrons to drift to the sense wire, via

$$t_D = (t_{meas} - t_{REF}) - [(t_{wire} + t_{cable}) - t_{REF}]\,. \quad (3)$$

In Eqn. 3, t_{meas} is the time recorded by the TDC and the term $t_{wire}+t_{cable}$ is the time it takes the signal to propagate across the sense wire, through the cable and into the TDC if the track were to pass directly through the sense wire. All of these times are measured relative to a common reference time, t_{REF}. When combined with information about the position of wires in each chamber, this quantity can provide coarse track information. However, this can be further refined by converting the drift time to a drift distance. This is accomplished by utilising time-to-distance maps for the detector. The purpose of the drift chamber calibration procedure is to produce these per-plane look-up tables.

A single cell[2] will see a uniform distribution of events through it. For a collection of events illuminating all cells in any given wire plane, a drift time distribution can be obtained. This distribution can be averaged over an entire group (up to 16 wires per discriminator card) or over the entire plane. Associated with each drift time distribution is a time, t_0, which corresponds to the time at which ionized particles come into contact with the wire. If this value is non-zero, this is the value by which all drift times must be shifted in order to assure that $t_0 = 0\,ns$. All subsequent times in each spectra are measured relative to this time. To determine t_0 for a plane, the weighted average of all t_0 wire values in that plane is utilised.

From the drift time spectra, $F(t)$, the drift distance, $D(t)$, spectra can be determined via

$$D(t) = D_{Max}\frac{\int_{t_0}^{t} F(t)dt}{\int_{t}^{t_{Max}} F(t)dt} \quad (4)$$

where D_{Max} is the maximum possible drift distance (0.5 cm, half a cell), t_{Max} is the maximum drift time and t is the measured drift time. Note that $D(t_0) = 0$ cm and $D(t_{max}) = 0.5$ cm. Due to the finite resolution of the TDC, the integrals in Eqn. 4 become sums over finite bin widths and Eqn. 4 can be re-written as

$$\frac{1}{N_{Tot}}\sum_{\mathrm{bin}(t_0)}^{\mathrm{bin}(t_0+T)} F(t), \quad (5)$$

which is simply a ratio of the sum of bin contents (up to some drift time, T) over all bin contents (up to a maximum, t_{max}), N_{tot}. The results of the calibration are per-plane look up tables which utilise this ratio to map any given drift time to a drift distance for that plane. When properly calibrated, this should result in a flat, uniform distribution of drift distances for each chamber. An example drift distance spectra, showing the pre and post calibration distributions can be seen in Fig. 25.

3.6. Heavy-Gas Cherenkov Counter

3.6.1. Design

The SHMS Heavy-Gas Cherenkov detector (HGC) is a threshold-type Cherenkov detector, designed to separate charged π and K over most of the SHMS operating momentum range, 3–11 GeV/c. C_4F_{10} radiator gas at 1 atm, with an index of refraction of n=1.00143 at standard temperature [35], allows $\pi^{\pm}$ to produce abundant Cherenkov light above 3 GeV/c momentum, while $K^{\pm}$ remain below Cherenkov threshold until about 7 GeV/c. Optimal π/K separation at higher momenta requires a reduction in the gas pressure, down to 0.3 atm at 11 GeV/c.

A schematic view of the detector is shown in Fig. 26. The SHMS focal plane is subtended by four 55×60 cm

[2] A cell is one sense wire surrounded by field wires such that the sense wire is at the center and the field wires are at the corners

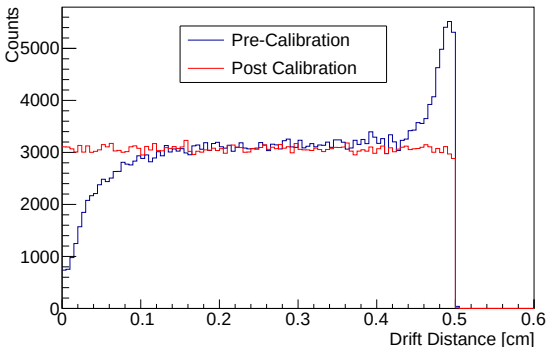

Figure 25: Example drift distance distributions for the SHMS drift chambers before (blue) and after (red) a successful calibration.

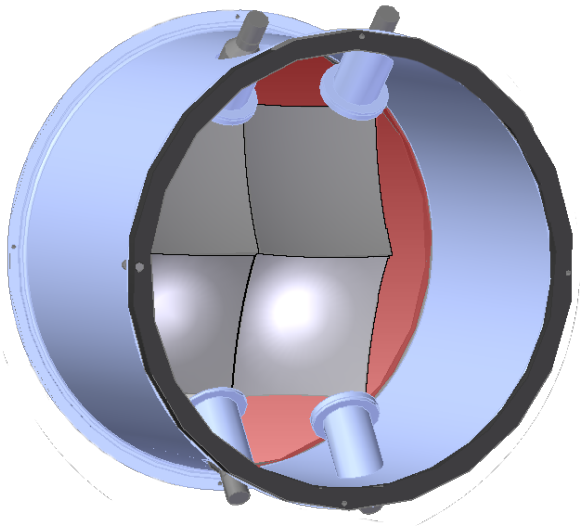

Figure 26: 3D-CAD rendering of the Heavy Gas Cherenkov Detector.

0.3 cm thick glass mirrors, which reflect the Cherenkov radiation to four Hamamatsu R1584 12.5 cm diameter photomultiplier tubes located above and below the particle envelope. The mirrors and gas are enclosed in a cylindrical aluminum tank of 164.9 cm inner diameter and 113.5 cm length, with entrance and exit windows of hydroformed 0.102 cm thickness 2024 T-4 aluminum alloy [36]. The vessel is sufficiently strong to be pumped to vacuum before introducing the radiator gas, avoiding the need to purge when filling. A unique aspect of the detector is the placement of the photomultipliers outside the gas envelope, viewing the enclosure through 1.00 cm thick Corning 7980 quartz windows. This allows the gas enclosure to be smaller in diameter than would otherwise be possible, as the full length of the PMT and base no longer need to be fully within the diameter of the vessel. It also makes the PMTs available for servicing without venting the gas.

The mirrors are inexpensive, having been produced by the slumping process [37]. As a result, they deviate from the desired 110 cm radius of curvature with a slightly oblate shape [38]. However, the Cherenkov cone on the mirrors for 3-7 GeV/c $\pi^{\pm}$ in C_4F_{10} is 7-10 cm in diameter, so optical quality mirrors are not required for this application. The UV wavelength characteristics of the respective optical components are relatively well matched. C_4F_{10} has good transmittance down to ~160 nm [35]. The quartz viewing windows provide >88% transmission down to 200 nm, including the ~10% loss due to surface reflection [39], and the optical glass face PMTs have 70% of their peak quantum efficiency at 200 nm (peak at 350 nm) [40]. Accordingly, the mirror reflectivity was optimized for >90% at 270 nm, and 75% at 200 nm [41].

The mirrors are arranged in a 2×2 array, with two mirrors directing the light to two upper PMTs and the other two directing it to lower PMTs. Because the mirrors are curved in both the horizontal and vertical directions, it is necessary to stagger the mirrors along the tank z-axis to avoid dead areas. The upper left and right mirrors are the most forwards, with the lower left and right being behind. The mirrors overlap slightly to give good $x-y$ coverage. The geometry near the center of the tank, where the mirrors make their closest approach, is complicated, and some shadowing for certain Cherenkov light trajectories is unavoidable. This leads to a small region of lower detection efficiency at the center of the tank. This is further discussed in Sec. 6.3.3

Each mirror is clamped individually along its two outer edges and is held in place by 3 flexible three-point mounts extending from the tank to the mirror clamps. This allows each mirror to be optically aligned in 3 dimensions separately from the others. The mirror positions were fine-tuned with the use of an LED-light array clamped to the front of the tank (the "Christmas tree"). The reflected light from each LED onto the PMT positions was compared to predictions of a Geant4 simulation and adjustments made until they came into close agreement.

3.6.2. Calibration

The goal of the SHMS HGC calibration procedure is to generate an accurate translation from raw FADC channels (or charge in pC) to the number of photoelectrons emitted from the cathode surface of the PMT

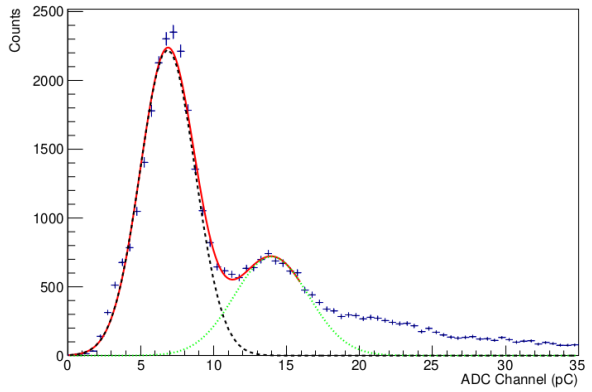

Figure 27: The isolated 1 (dashed black) and 2 (dotted green) photoelectron peaks for the lower right PMT #2, and their sum (solid red), obtained by selecting adjacent mirror light from the upper right quadrant #4. Three such adjacent mirror plots are obtained for each PMT. The light from the mirror closest to the PMT is far more intense, with too few SPE events available to yield a reliable calibration.

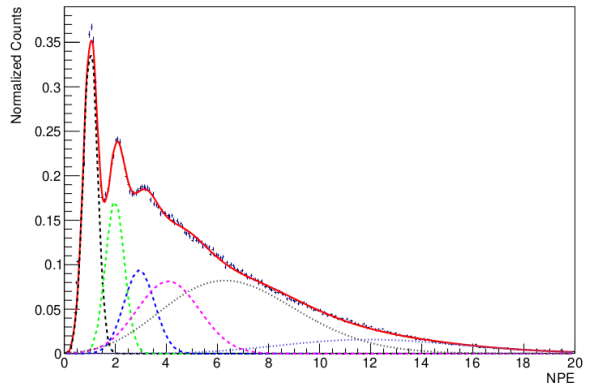

Figure 28: Results from a successful calibration of the HGC. Shown is the NPE distribution of the lower right PMT #2 obtained from all four mirrors. The 1, 2, and 3 NPE peaks are shown, indicated by dashed Gaussian distributions. Two Poisson distributions (dotted lines) provide a good description of the nearest mirror events with large NPE, and a broad Gaussian near 4 NPE fills in the gap with the lower NPE peaks. The sum of all 6 distributions is shown as the solid red curve.

(NPE). This is achieved by isolating the single photoelectron (SPE) peak, yielding a calibration, and then verified by examining the regular spacing of the first few photoelectron contributions in the ADC spectrum.

To isolate the SPE peak, tracking cuts are applied to the data to analyze what each PMT detected from charged particles traversing each mirror quadrant. As a charged particle passes through a mirror quadrant, the produced Cherenkov cone allows some light to be incident on adjacent mirrors. As each mirror is focused on a single PMT, one PMT will receive most of the produced light while the other three "off-axis" PMTs receive much smaller amounts. This small signal on the 3 "off-axis" PMTs allows the SPE peak to be measured, yielding a reliable calibration. To select this adjacent mirror light, cuts (based on the physical dimensions of the mirrors) are placed on the tracked coordinates of the charged particles, extrapolated to the HGC mirror plane,

$$x_{\text{HGC}} = x_{\text{Focal Plane}} + x'_{\text{Focal Plane}} \cdot z_{\text{HGC}} \quad (6)$$

$$y_{\text{HGC}} = y_{\text{Focal Plane}} + y'_{\text{Focal Plane}} \cdot z_{\text{HGC}}, \quad (7)$$

where $z_{\text{HGC}} = 156.27$ cm is the distance from the focal plane to the HGC mirror plane. The coordinate axis for the HGC is the convention used in charged particle transport in dispersive magnetic systems. The x-axis is the direction of increasing particle momentum, the z-axis is the direction of particle travel through the spectrometer, and the y-axis is deduced from $z \times x$. Additionally, timing cuts are applied to the HGC data, collected using the high resolution pulse time setting in the FADC250's FPGA. The time measured corresponds to the time it takes a pulse to reach half of its maximum amplitude after passing a pedestal threshold of 5 mV. Lastly, a cut on particle velocity, β, is also applied, obtained from the tracking algorithm.

An example of a completed calibration is shown in Figs. 27, 28. For this run, the HGC was filled with C_4F_{10} at 1 atm, and the SHMS central momentum was 2.583 GeV/c, with polarity set to detect positively-charged particles. Cherenkov radiation is produced by π^+ traversing the HGC with momentum > 2.598 GeV/c. This can occur only for $\delta > +0.5\%$, which corresponds roughly to the bottom half of the HGC. Subthreshold π^+ with $\delta < +0.5\%$, as well as K^+ and p, may produce low-level light in the HGC via knock-on electron emission and scintillation in the radiator gas. The adjacent mirror cuts described above produce a clear SPE peak in Fig. 27, which provides the main source of calibration information.

A histogram of light collected in one PMT from all four mirrors is shown in Fig. 28, where the average number of photo electrons detected per event is higher due to the more intense light from the closest mirror. In this figure, the spectrum is fit with a sum of four Gaussian and two Poisson distributions, shown by the solid red line.

An inherent systematic uncertainty is present in the HGC calibration due to statistical errors in determining the location of the SPE peak in the various mirror quadrants. This uncertainty was quantified by recording the locations of the SPE across several runs, for the different adjacent mirror combinations for each PMT, as well as by varying the contribution of the higher PE tail extending underneath the SPE peak, as in Figs. 27, 28. The

systematic uncertainty in the calibration is taken to be the root mean square of this set of values, giving ±1.5%. It should be noted this uncertainty is somewhat larger than the statistical uncertainty of the SPE peak, which is typically 0.2 to 0.6%.

3.6.3. Gain Matching

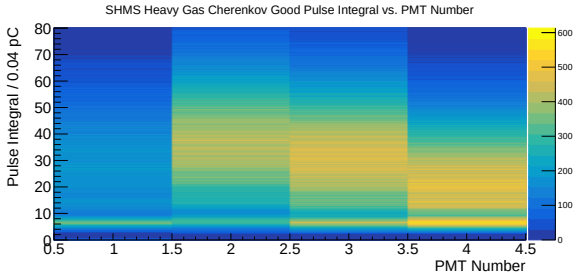

Figure 29: Demonstration of gain matching between PMTs by the alignment of the single photoelectron, indicated by the yellow band about 6.825 pC. The horizontal axis refers to PMT number, the vertical axis to Pulse Integral in bins of 0.04 pC. The color axis represents the number of events filling each bin.

To ensure each PMT has a similar response to incident light, the voltages of each PMT were adjusted to obtain accurate gain matching. This can be seen in Fig. 29 by the alignment of the SPE at approximately 6.825 pC, represented by the common band across all four PMTs at that value. Additionally, the gain of each PMT was tested by the manufacturer, Hamamatsu, and at Jefferson Lab. The results of each test are shown in Table 3. The Hamamatsu data were taken directly at 2000 V in a highly controlled environment, thus leading to small uncertainty in the gain which was not quoted. The Jefferson Lab measurement were also taken at 2000 V, but taken in an experimental environment. This gives rise to an uncertainty in the JLab gain data on the order of 1%, larger than the Hamamatsu data.

PMT	JLab Gain	Hamamatsu Gain
PMT 1	$(2.79 \pm 0.01) \times 10^7$	0.969×10^7
PMT 2	$(6.55 \pm 0.04) \times 10^7$	3.60×10^7
PMT 3	$(7.12 \pm 0.05) \times 10^7$	5.79×10^7
PMT 4	$(5.35 \pm 0.04) \times 10^7$	3.20×10^7

Table 3: Gain characteristics for the PMTs in the HGC. Two measurements were performed, one at Jefferson Lab in an experimental setting, and one by the manufacturer Hamamatsu. The set voltage for the gain measurements is 2000 V for each PMT.

3.7. Noble-Gas Cherenkov Counter

3.7.1. Design

Analyzing momenta up to 11 GeV/c at scattering angles from 5.5° to 40.0°, the SHMS will reach kinematic regions in which the pion background rate dominates the scattered electron rate by more than 1000:1. The suppression of these anticipated pion backgrounds while maintaining efficient identification of electrons is therefore one of the main duties of the SHMS detector elements and the SHMS Noble Gas Cherenkov Detector shoulders a large portion of this particle identification burden. The design of the noble gas threshold Cherenkov detector is such that it will meet these twin goals of suppression and identification. The main goal of the detector is to distinguish between electrons and pions with momenta between 6 GeV/c and 11 GeV/c. Operating at 1 atm it will use a mixture of argon and neon as the radiator: pure argon with an index of refraction n=1.00028201 at a SHMS momenta of 6 GeV/c and pure neon with an index of refraction n=1.000066102 at 11 GeV/c and a mixture of argon and neon at intermediate momenta.

The SHMS NGC design was restricted by the available space and the need to have good discrimination at the highest momenta. The number of photoelectrons is maximized in this design by the use of quartz window PMTs and mirrors with excellent reflectivity well into the UV.

The NGC consists of the four main elements: 1) a light tight box with thin entrance and exit windows designed to operate at 1 atm; 2) four spherical mirrors held in a rigid frame; 3) four 5 inch quartz window photomultipliers (PMTs) and 4) the radiator gas.

The tank was fabricated with an internal rigid aluminum t-slot frame and thin aluminum walls welded together and has an active length of 2 m along the beam direction and approximately 90 cm perpendicular to the beam direction. The main access is provided through a large ‘door’, and four small panels provide modest access to the PMTs. The tank has feedthroughs for gas management as well as for HV and signal cables. The interior was painted with a black flat paint to prevent the reflection of light from cosmic rays or hall background. Thin entrance and exit windows made of two layers of 2 mils of the Dupont product Tedlar $(CH_2CHCl)_n$ are also present. The PMTs were positioned outside the active area of the scattered particles, achieved by a 15° tilt of the mirrors.

Four spherical thin glass mirrors of radius 135 cm, square in shape with edges of 43 cm focus the Cherenkov light onto the PMTs. The glass blanks were

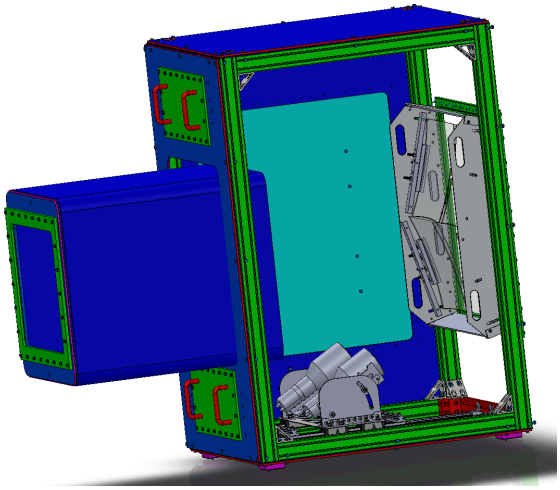

Figure 30: Sketch of the NGC tank. This view is possible as one panel is removed. Note the PMT mounting system is different than shown here.

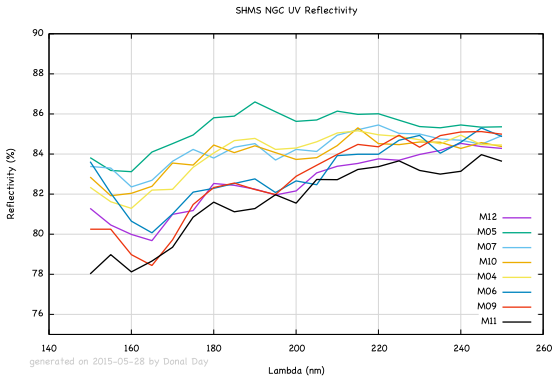

Figure 31: The UV measured reflectivity of the finished mirrors, coated at CERN which is no less than 78% at 150 nm. Between 250 nm and 600 nm the reflectivity rises to almost 90%.

manufactured by Rayotek Scientific [42] from borosilicate glass of 3 mm thickness by slumping over a polished steel mold and then cutting to dimensions. Simulations showed a reduction of collection efficiency due to incoming photon losses at the exposed edges of the mirror. As such, the edges were bevelled away from the active surface to minimize scattering from these edges.

The final batch of the glass blanks was shipped to Apex Metrology Solutions of Fort Wayne for coordinate measuring machine shape scanning measurements. Apex's measurements were performed on a grid of 1806 points. The data were fitted with spherical, conical and elliptical fit functions for each mirror. Though the elliptical fit described the surface slightly better than the spherical fit, the updated simulation with the real measured parameters showed almost no difference in the collection efficiency between the two. In addition, the same fitting was performed for 5 selected locations on the mirror: entire mirror, the center, and 4 quadrants. Based on the spherical fit results "best" mirrors and "best" corners for each mirror were identified. The 4 mirrors come together and overlap at the center of the acceptance where a majority of the scattered electrons are focused. Care was then made to select among the best 4 glass pieces their best corners so as to be in the overlap region. The radii of the 4 best pieces of glass, from fitting, was found to never vary by more than 2 cm from the contracted value of 135 cm in fit areas described above.

The blanks were coated by the Thin Film and Glass Service of the Detector Technologies Group at CERN [43]. The reflectivity was also measured at CERN and found to be excellent well into the UV (Fig. 31).

Like the HGC, the four mirrors are arranged in a 2 by 2 array with a small overlap in the center, providing full coverage over the active area. In order to accomplish this without mechanical interference, the mirrors were staggered at slightly different along the tank z-axis. The mirrors were mounted in a monolithic frame installed as single unit (see Figure 32), and are tilted at 15° off the z-axis to place the PMTs to be outside the active area.

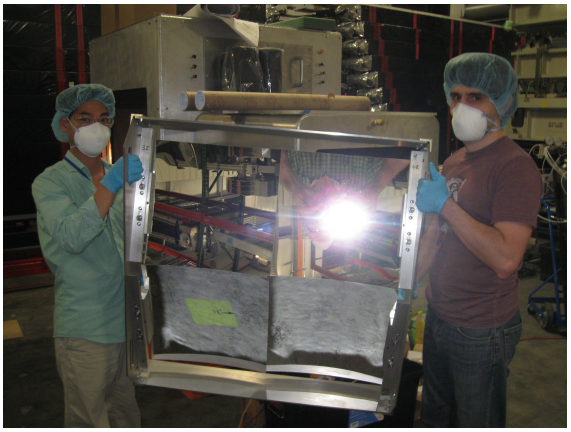

Figure 32: Frame with mirrors about to be moved into tank.

The four PMTs are 14 stage 5" quartz window PMTs manufactured by Electron Tubes Enterprises [44], model 9823QKB04. The tubes are surrounded by a mu-metal shield and the HV is distributed to the stages by a positive base. The 9823QKB04 has a quantum efficiency above 5% at 150 nm and 30% at 350 nm as seen

in Figure 33.

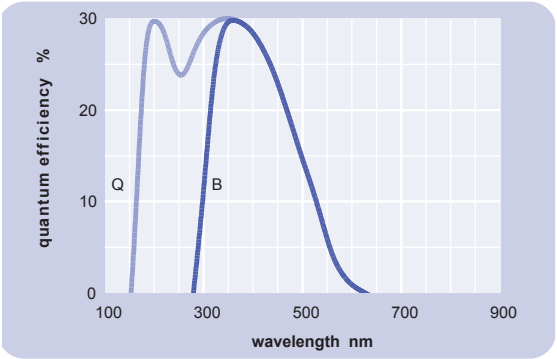

Figure 33: Quantum efficiency of Electron Tubes Enterprises model 9823QKB04 - light blue curve, labeled "Q".

3.7.2. Calibration

As with the HGC (see Sec. 3.6.2), the goal of the NGC calibration procedure is to generate an accurate transformation from raw FADC channels to the number of photoelectrons (NPE) emitted from the cathode surface of the PMT. The NGC calibration method can be broken down into three key steps:

1. Selecting an appropriate data set.
2. Selection cuts to identify a clean electron sample for each PMT.
3. Using the clean electron sample to fit the pulse integral distribution for each PMT. This is used to determine the calibration constants.

Selecting an appropriate data set. The NGC calibration requires electron events in the SHMS. Any data set with the SHMS running with negative polarity can in theory be utilised for calibrations. However, for best results, a data sample with an even distribution of events across all PMTs in the NGC should be utilised. Additionally, the data set should contain on the order of $\sim 10^6$ events or more.

Selection Cuts. To obtain a clean electron sample from the data, several selection cuts are applied to the data. Cuts are applied on:

- $-10 \leqslant \delta \leqslant 20$, a nominal acceptance cut, removing events outside this range.
- $0.7 \leqslant E_{TotTrackNorm} \leqslant 2.0$, a calorimeter based PID cut using the normalized calorimeter energy to remove pion/hadron background events.
- NGC multiplicity and position cuts. These are used to select events where the majority of the Cherenkov light was deposited in a single PMT.

After selection cuts, the PMTs can be calibrated.

Determining Calibration Constants. After selection cuts, the pulse integral distributions for each of the NGC PMTs are fitted with the function

$$f(x) = A \frac{\frac{\lambda}{\mu}^{\frac{x}{\mu}} e^{-\frac{\lambda}{\mu}}}{\Gamma\left(\frac{x}{\mu}+1\right)}, \tag{8}$$

where A is a normalization factor to account for the number of events in the dataset being fit, λ is the mean NPE emitted from the photocathode of the PMT for an event above the Cherenkov threshold, and μ is the calibration constant which relates the pulse integral to the corresponding NPE emitted from the photocathode of the PMT. This value is determined for each PMT. An example pulse integral distribution and the associated fit can be seen in Fig. 34.

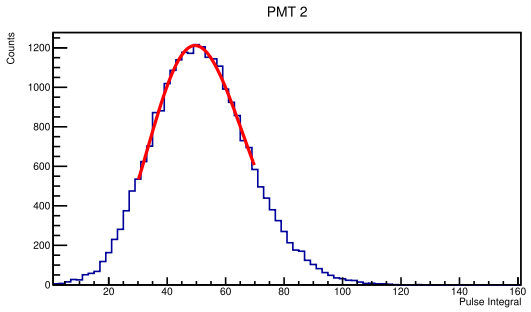

Figure 34: A sample pulse integral distribution fitted with the function described by Eqn. 8 shown in red.

The NGC PMTs were also gain matched in a similar manner to the HGC. Refer to Sec. 3.6.3 for details on this procedure.

3.8. Aerogel Cherenkov Counter

3.8.1. General Design Overview

The detector design is summarized in Fig. 35 which shows a photograph of the aerogel counter installed downstream of the cylindrical HGC in the SHMS detector stack. The detector consists of two main components: a tray which holds the aerogel material, and a light diffusion box with photomultiplier tubes (PMTs) for light readout. Four identical trays for aerogel of nominal refractive indices of 1.030, 1.020, 1.015 and 1.011 were constructed. The design allows for easy detector assembly and replacement of the aerogel trays.

Using up to 9 cm aerogel thickness in the trays, the total depth of the detector is 24.5 cm along the optical axis of the SHMS. A detailed discussion of the detector, characterization of its components, and performance tests can be found in Refs. [45, 46].

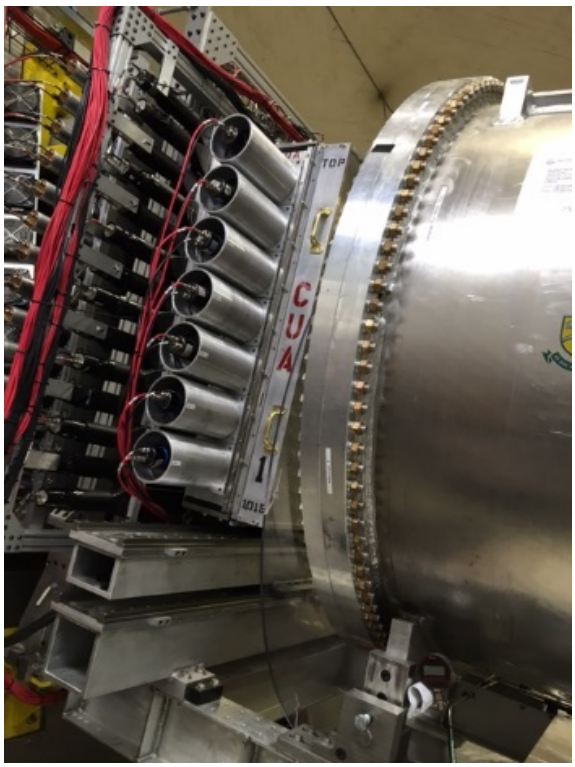

Figure 35: Photograph of the aerogel Cherenkov detector (*"CUA"* printed on the side of the radiator tray) installed in the SHMS detector stack. To its right is the Heavy Gas Cherenkov. On the left can be seen the edge of the S2X and S2Y hodoscope arrays.

Table 4: Threshold momenta P_{Th} in GeV/c for Cherenkov radiation for charged muons, pions, kaons, and protons in aerogel of four refractive indices ranging from n=1.011 to 1.030.

Particle	P_{Th} n=1.030	P_{Th} n=1.020	P_{Th} n=1.015	P_{Th} n=1.011
μ	0.428	0.526	0.608	0.711
π	0.565	0.692	0.803	0.935
K	2.000	2.453	2.840	3.315
p	3.802	4.667	5.379	6.307

The diffusion box is made of the aluminum alloy 6061-T6. The side panels are constructed of ~2.5 cm (1-inch) plates. The back cover is ~1 mm (1/16") thick. The inner dimensions of the box are ~ 103 × 113 × 17.3 cm^3 (40.5" × 44.5" ×6.82"). To optimize light collection the inner surface of the diffusion box is lined with either 3 mm (covering ~60% of the surface) or 1 mm (remaining ~40% of the surface) thick GORE reflector material [47]. This material has a reflectivity of about 99% over the entire spectrum.

The light collection is handled by 5"diameter photomultiplier tubes (XP4500). The 5.56" (14.1 cm) diameter cylindrical housings holding the PMTs are mounted upon 14 waterjet cut circular openings on the left and right (long) sides of the diffusion box, with minimum spacing of 14.92 cm (5.875") between the centers. The PMTs are sealed into their housing using a light-tight synthetic rubber material (Momentive RTV103 Black Silicone Sealant) and the whole assembly is sealed light-tight. The mechanical design includes six openings on the top of the diffusion box, presently covered with blanks, that can be used to increase the signal output from the detector by about 30%, if needed.

The magnetic shielding for the PMTs consists of 13.5 cm (5.316") diameter μ-metal cylinders, which were constructed to end abreast with the PMT window. The construction also features bucking coils that can be installed on the PMTs, if excessive residual magnetic fields appear to be present in the SHMS hut.

The aerogel trays are of the same transverse size as the diffusion box but 11.3 cm (4.45") deep. The front cover of the trays is made of a 5 mm thick honeycomb panel with an effective aluminum thickness of ~1.3 mm (0.050"). The inner surface of the SP-30 and SP-20 aerogel trays is covered with 0.45 μm thick Millipore paper membrane GSWP-0010 (Millipore) of reflectivity of about 96% [48]. Though Millipore is difficult to handle, its chemical inertness makes it superior to reflective paints. For the two lower refractive index trays (SP-15 and SP-11), in order to optimize light collection, we used 1 mm thick GORE diffusive reflector material (DRP-1.0-12x30-PSA) with reflectivity of about 99%.

For the Cherenkov radiator high transparency aerogels were used. The higher two of the refractive indices (SP-30 and SP-20) were originally manufactured by Matsushita Electric Works, Ltd. The lower two indices (SP-15 and SP-11) were manufactured by the Japanese Fine Ceramics Center. These tiles have dimensions of approximately 11 cm by 11 cm by 1 cm. They feature a waterproof coating that make them hydrophobic [49, 50]. This removes the need for baking (which in fact would destroy the coating). Detailed studies of the aerogel characteristics are presented in Ref. [45].

The trays were filled with aerogel tiles layer by layer. In each layer the tiles were laid down flat and arranged in a brick pattern to minimize holes in the radiator. To fill gaps of less than the size of a full tile at the edges of

the tray, the aerogel material was cut using a diamond coated saw or razor depending on the refractive index of the material. The aerogel radiator is on average ~9 cm thick (8 layers). The SP-30, SP-20 and SP-15 aerogel trays were filled over their entire 110 cm x 100 cm area. The SP-11 aerogel tray radiator covers only the active area of 90 cm x 60 cm required by the experiments [51, 19, 17, 52, 13]. An inner frame has been designed to arrange the aerogel tiles inside the active area of this tray. The sides of this inner frame are made of carbon fiber square tubes. This assembly allows future X-Y repositioning of the inner frame inside the tray.

To protect the aerogel radiator from severe damage in case of accidental flipping over of a tray during installation, a net of thin stainless steel wires is installed in close proximity to the aerogel surface. This is a technique previously tested in aerogel detectors at JLab [53]. The wires form an interweaving grid by running between stainless steel screws on the sides of the box. Small springs attached to the ends of wires provide necessary tension.

An aerogel tray attaches to the diffusion box by means of bolting through flanges surrounding both boxes. A round O-ring running in a shallow groove along the diffusion box sides ensures a light tight connection. The entire detector is designed so that it can be removed from the sliding detector stand that positions the detector into the SHMS detector stack.

3.8.2. Performance aspects

The light collection performance of the detector was tested with cosmic rays and electron beam. The detector signal shows good uniformity along the vertical (Y) coordinate of the detector surface, but has a significant dependence in the horizontal (X) direction. Possible optimization of this include a variable threshold and an optimized selection of the PMTs installed on the right and left side of the detector. The response of the detector to particles is shown in Fig. 36.

The mean number of photo-electrons in saturation for the tray filled with n=1.030 (n=1.020) refractive index aerogel is ~10 (~8), which is close to expectation from Monte Carlo simulation. For the trays filled with n=1.015 and n=1.011 refractive index aerogel, high numbers of photoelectrons were obtained with the use of higher reflectivity GORE material to cover the tray, ~10 and ~5.5 respectively. This result could be fully reproduced by our Monte Carlo simulation by also assuming the aerogel absorption length on the order of 220 cm.

3.8.3. Results from tests with beam

The performance of the detector was tested with beam in Hall C. The detector signal showed good uniformity along the vertical direction, but significant dependence in the horizontal direction. Possible optimizations to address this are discussed below. The mean number of photoelectrons in saturation for a tray filled with n=1.030 refractive index aerogel is 12 photoelectrons and 10 for the tray filled with n=1.015 refractive index aerogel (see Fig. 36).

3.9. Preshower and Shower Counters

3.9.1. Preface

The approved experiments demand a suppression of pion background for electron/hadron separation of 1,000:1, with suppression in the electromagnetic calorimeter alone on the level of 100:1. An experiment to measure the pion form factor at the highest accessible Q^2 at JLab with an 11 GeV beam requires a strong suppression of electrons against negative pions of a few 1,000:1, with a requirement on the electromagnetic calorimeter of a 200:1 suppression.

Particle detection using electromagnetic calorimeters is based on the production of electromagnetic showers in a material. The total amount of the light radiated in this case is proportional to the energy deposited by the primary particle in the medium. Electrons (as well as positrons and photons) will deposit their entire energy in the calorimeter giving the ratio of of energy detected in the calorimeter to particle energy of one.

Charged hadrons entering a calorimeter have a low probability to interact and produce a shower, and may pass through without interaction. In this case,they will deposit a constant amount of energy in the calorimeter. However, they may undergo nuclear interactions in the radiator (in our case lead-glass) and produce particle showers similar to the electron and positron induced particle showers. Hadrons that interact inelastically near the front surface of the calorimeter and transfer a sufficiently large fraction of their energy to neutral pions will mimic electrons. The maximum attainable electron/hadron rejection factor is limited mainly by the cross section of such interactions.

In this section we describe details of construction of the SHMS calorimeter. We present results of preassembly component checkout, and performance from experimental studies.

3.9.2. Construction

As a full absorption detector, the SHMS calorimeter is situated at the very end of detector stack of the spectrometer [54]. The relatively large beam envelope of the

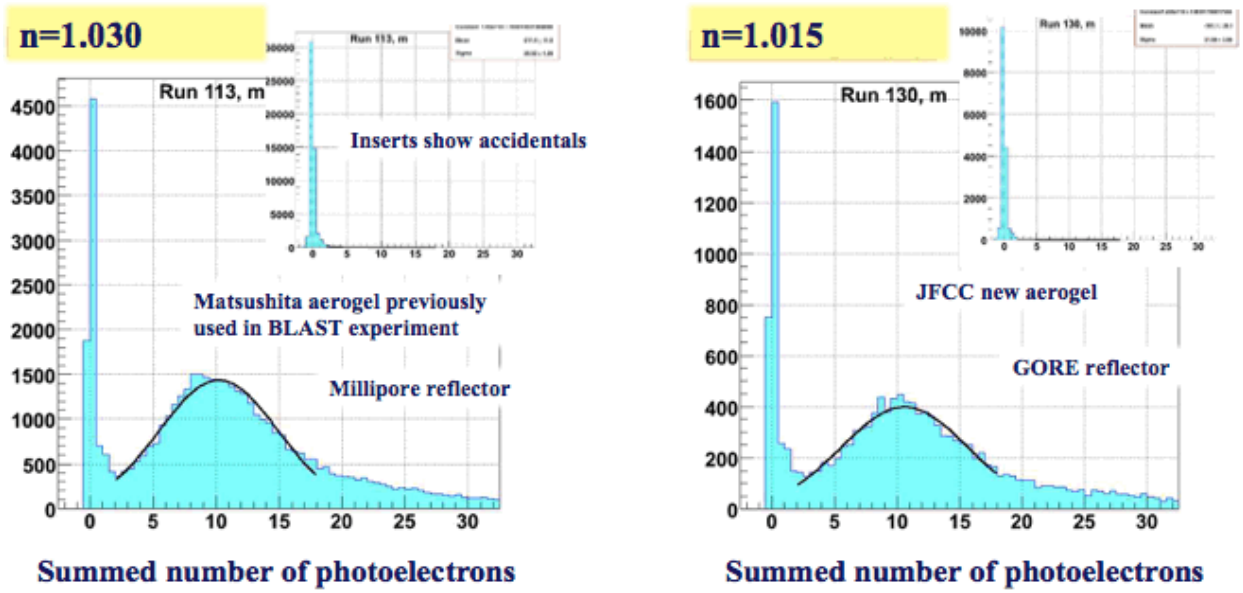

Figure 36: Numbers of photoelectrons observed in the Aerogel Cherenkov.

SHMS dictated a design of a wide acceptance coverage. The general requirements for the SHMS calorimeter were:

- Effective area: $\sim 120 \times 140\,\mathrm{cm}^2$.
- Total thickness: ~ 20 rad. length.
- Dynamic range: 1.0 - 11.0 GeV/c.
- Energy resolution: $\sim 6\%/\sqrt{E}$, E in GeV.
- Pion rejection: $\sim$100:1 at $P \gtrsim$1.5-2.0 GeV/c.
- Electron detection efficiency: $> 98\%$.

The SHMS calorimeter consists of two parts (see Fig. 37): a Preshower at the front of the calorimeter, for additional PID, and the main part, the Shower, at the rear for full calorimetry.

An optimal and cost-effective choice was found by using available modules from the HERMES calorimeter for the Shower part, and modules from the Hall C decommissioned SOS calorimeter for the Preshower. With this choice, the Shower is 18.2 radiation lengths deep and almost entirely absorbs showers from $\sim$10 GeV electromagnetic projectiles, and the Preshower is 3.6 radiation lengths thick.

The SHMS Preshower radiator consists of a layer of 28 TF-1 type lead glass blocks stacked in two columns in an aluminum enclosure (not shown in Fig. 37). 28 PMT assemblies, one per block, are attached to the left and right sides of the enclosure. The Shower part consists of 224 F-101 type lead glass modules stacked in a "fly's eye" configuration of 14 columns and 16 rows. All blocks of the Preshower were produced between 1985-1990 by a Russian factory in Lytkarino [55], whose products were well known for their good optical quality. The effective area of detector ($120\times130\,\mathrm{cm}^2$) covers the beam envelope at the calorimeter.

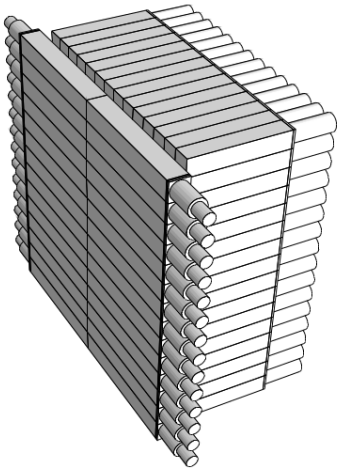

Figure 37: A sketch of SHMS calorimeter. Shown are Preshower (on the left) and Shower parts. Support structures are omitted.

The Preshower enclosure adds little to the material in the path of particles. On the front and back are a 2" honeycomb plate and a 1 mm sheet of aluminum respec-

tively, which add up to only 1.7% of a radiation length. The optical insulation of the 10 cm × 10 cm × 70 cm TF-1 blocks in the Preshower is optimized to minimize the dead material between them, without compromising the light tightness. First, the blocks are loosely wrapped in a single layer of 50 μm thick reflective aluminized Mylar film, with the Mylar layer facing the block surface. Then, every other block is wrapped with a 10 cm wide strip of 50 μm thick black Tedlar film, to cover its top, bottom, left and right sides except for the circular openings for the PMT attachments. Looking at the face of the detector, the wrapped and unwrapped blocks are arranged in a checkerboard pattern. Insulation of the remaining front and back sides of the blocks are provided by facing inner surfaces of the front and rear plates of the enclosure, also covered with Tedlar. In addition, a layer of Tedlar separates the left and the right columns. The PMT assembly tubes are screwed into 90 mm diameter circular openings on both sides of the enclosure. The spacing of the openings matches the height of the blocks, so that a PMT faces to each of the blocks. The 3" XP3462B PMTs are optically coupled to the blocks using ND-703 type Bicron grease of refractive index 1.46.

The Shower radiator is an optically isolated 8.9 × 8.9 × 50 cm^3 block of F-101 lead-glass, which is similar to TF-1 in physical parameters. The typical density of F-101 type lead-glass is 3.86 g/cm^3, radiation length 2.78 cm, and a refractive index of ~1.65. Results of TF-1 and F-101 type lead-glass blocks transmittance measurements are presented in Ref. [54]. Each F-101 block is coupled to a 3" Photonis XP3461 PMT, with green extended bialkali photocathode, of the same sizes and internal structure as the XP3462B in the Preshower. Typical quantum efficiency of the photocathode is ~ 30% for λ ~400 nm light, and the gain is ~ 10^6 at ~1500 V. Silgard-184 silicone glue of refractive index 1.41 is used for optical coupling of the PMTs to the lead-glass blocks. A 1.5 mm thick μ-metal sheet and two layers of Teflon foil are used for magnetic shielding and electrical insulation of the PMTs. The blocks are wrapped with 50 μm aluminized Mylar and 125 μm black Tedlar paper for optical insulation. A surrounding aluminum tube which houses the μ-metal, is fixed to a flange, which is glued to the surface of the lead-glass. The flange is made of titanium, which matches the thermal expansion coefficient of F-101 lead-glass [56].

Beyond simple repairs, no adjustments have been made to the original HERMES construction of the modules for re-use in the SHMS calorimeter. As both the TF-1 and F-101 lead-glass blocks have been in use for more than 14 years under conditions of high luminosity, there was concern about possible radiation degradation of the blocks and the PMTs. The changes in transparency of TF-1 and F-101 type lead-glass radiators have been studied. The estimated radiation dose for the used blocks was about 2 krad. For several samples of F-101 and TF-1 type blocks, the light transmittance has been measured before and after 5 days of curing with UV light (of wavelength λ=200-400 nm). No notable degradation in transmittance was found for the TF-1 type blocks taken from the SOS calorimeter and F-101 blocks taken from the HERMES detector.

The gain and relative quantum efficiencies for randomly selected PMTs from the SOS calorimeter (XP3462B) and from the HERMES detector (XP3461) have been measured to check possible degradation effects in the PMTs. A ~10–15% systematic decrease in quantum efficiency was noticed.

3.9.3. Photomultiplier tube selection and studies

The SHMS Preshower inherited PMTs from the retired SOS calorimeter. The choice of XP3462B PMT for Hall C calorimeters was made in 1994 after studies of several other 3" and 3.5" photomultiplier tubes on the matter of having good linearity, photocathode uniformity, high quantum efficiency, and good timing properties. Gain variations with HV and dark currents were also measured [57]. For samples of PMTs, the photocathode uniformity and effective diameter have been studied with a laser scanner. Following these tests, as a time and cost effective solution, a 3" diameter (≈68 mm) semitransparent bi-alkaline photocathode, Photonis XP3462B PMTs were chosen for the equipment of the JLab Hall C calorimeters. These 8-stage PMTs have a linear focused cube dynode structure with a peak quantum efficiency of ~29% at 400 nm.

3.9.4. Studies on optical properties of TF-1 type lead glass blocks

With its index of refraction ~1.65, radiation length 2.74 cm and density of 3.86 g/cm^3, TF-1 type lead glass is well suited for serving as Cherenkov radiator in electromagnetic calorimeters. The fractional composition consists primarily of PbO (51.2%), SiO_2 (41.3%), K_2O (3.5%) and Na_2O (3.5%).

The light transmittance of TF-1 type lead-glass blocks for the SHMS Preshower was checked in 2008 using a spectrophotometer from the JLab Detector Group [58]. The wave-length was scanned from 200 nm to 700 nm in steps of 10 nm. The blocks were oriented transversely, and the light intensity passing through the 10 cm thickness was measured. The results were compared with measurements from 1992, before assembling

of calorimeters for the Hall C HMS/SOS spectrometers. Reliability of the measurements was checked by measuring spared, unused blocks and comparing again with 1992 data. From comparison of 1992 and 2008 data, signs of marginal degradation has been noticed.

3.9.5. Choice and studies of PMT bases

The Preshower PMT high voltage base design is optimized for the requirements of good linearity (better than 1%), high rate capability and a weak variation of PMT gain with anode current [57].

A design, which is a purely resistive, high current (2.3 mA at 1.5 kV), surface mounted divider ($\sim$ 0.640 $M\Omega$), operating at negative HV was selected. The relative fractions of the applied HV between the dynodes (from cathode to anode) are: 3.12/1.50/1.25/1.25/1.50/1.75/2.00/2.75/2.75. The supply voltage for a gain of 10^6 is approximately 1750 V.

The PMT resistive base assembly is linear to within $\sim 2\%$ up to the peak anode current of 120 μA ($\sim 5\times10^4$ pe). The dark current is typically less than 3 nA. The base has anode and dynode output signals.

3.9.6. Monte Carlo simulations

Prior to construction, the designed calorimeter setup was simulated in order to optimize the setup and get predictions for key characteristics. The simulations were based on the GEANT4 package [59], release 9.2. As in the simulations of the HMS calorimeter (see [54]), the QGSP_BERT physics list was chosen to model hadron interactions [60]. The code closely followed the parameters of the detector components. Other features are added into the model to make it more realistic, such as:

- Light attenuation length in the lead glasses and its block to block variation according to our measurements.
- PMT quantum efficiencies from the graphs provided by vendor.
- Passive material between the spectrometer focal plane and the calorimeter.
- Sampling of incoming particles at the focal plane of the spectrometer.

The Cherenkov light propagation and detection was handled by a custom code, using an approximation of strict rectangular geometry of the lead glass blocks with perfectly polished surfaces. Light reflection and absorption by the Mylar wrapping was modeled via aluminum complex refractive index, with Mylar support facing the block, and a thin air gap between the wrapping and the block. Both light passage to the PMT photocathode through the optical grease and the PMT window, and reflections from the block sides were modeled using the approximation of thin dielectric layers ([61], p. 360). The electronic effects, such as pedestal widths and channel to channel PMT gain variations, were assumed as for the HMS calorimeter before the 12 GeV modifications.

The simulations revealed no flaws in the design construction of the SHMS calorimeter, and performance similar to other lead glass based calorimeters. The studies indicated gain in pion suppression on the order of several times from combining signals from the Preshower with the total energy deposition in the calorimeter.

3.9.7. Calorimeter Gain Matching

Gain matching of PMTs is important for uniformity of performance of the calorimeter over the spectrometer's acceptance. Minimum ionizing particles (MIP's) were used for this purpose as their signals from the calorimeter are nearly independent of the incident particle's momentum.

MIP pion candidates for the Shower gain matching were selected by requesting 4 PMT signals from the Heavy Gas Cherenkov counter of less than 2 p.e., and the normalized deposited in the Preshower energies close to the MIP peak value, within a range from 0.02 to 0.15. In addition, the MIP dominance in the Shower itself was ensured by selecting single hit events, when only one module was fired. The resultant MIP peaks in the ADC signal distributions were localized by Gaussian fits (see Fig. 38).

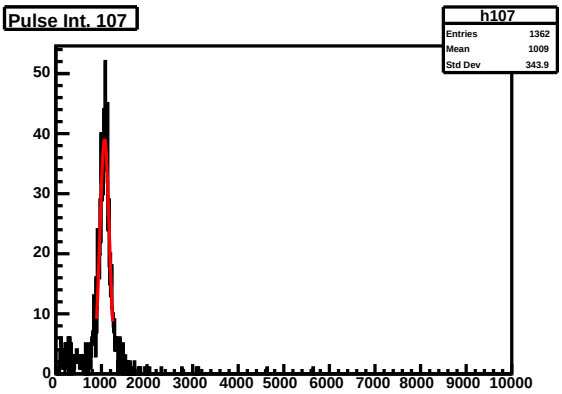

Figure 38: Distribution of ADC signals of a Shower module from minimum ionizing pions. The red line is a Gaussian fit to the MIP peak.

As gain matching had to be achieved by adjustment of high voltages on the PMT bases, knowledge of gain variations versus supplied HV's were needed. These were obtained by measuring signals from MIP pions at 2 constant supply high voltages on all the Shower channels, at 1.4 kV and 1.5 kV (see Fig. 39). By assuming gain dependence on supplied voltage in the form $\sim V^{\alpha}$ [40], the average exponent α was found to be 5.70 ± 0.01 for a set of ∼100 channels.

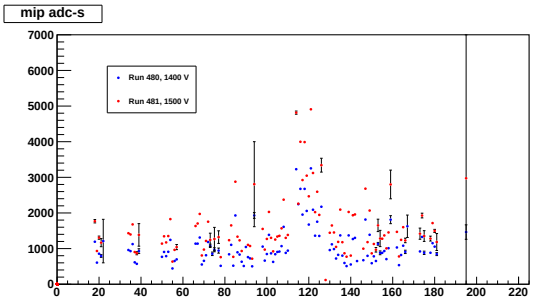

Figure 39: Amplitudes of ADC signals from MIP pions in a set of Shower channels, for supply voltages of 1.4 kV and 1.5 kV.

The gain matching was done in two ways. In the first case, MIP signals from pions were used. From the reference run with supply voltages A_{REF} = 1.4 kV in all the Shower channels, MIP ADC signal amplitudes $A_{REF}(i)$ were obtained, as described above. For a desired constant signal amplitude A_{SET} = 1000 ADC channels, the set voltages $V_{SET}(i)$ were estimated via

$$V_{SET}(i) = V_{REF} \cdot \left(\frac{A_{SET}}{A_{REF}(i)} \right)^{1/\alpha} . \qquad (9)$$

In the second case, data from a run with negative polarity (electrons in the SHMS) were used. The SHMS optics was set up at 3 GeV/c central momentum, in a defocused mode, which allowed for hitting and calibration with electrons of more than 150 Shower modules. For deposited energy E in a given module with signal amplitude A, PMT gain g, and calibration constant c, the following holds: $A \sim g \cdot E$, $E = c \cdot A$. Hence $g \sim V^{\alpha} \sim 1/c$, and for the chosen calibration constant c_{SET} one obtains

$$V_{SET}(i) = V_{REF} \cdot \left(\frac{c_{SET}^{-1}}{c_{REF}^{-1}(i)} \right)^{1/\alpha} . \qquad (10)$$

The HV settings from the second method, for c_{SET} = 35 MeV/ADC ch are within the range from 1.2 kV to 1.6 kV, grouped around 1.4 kV (Fig. 40). A few settings above the hard limit of 1.7 kV were forced to the limit. The HV settings from the two methods are in correlation.

Note that out of the SHMS acceptance, and hence not gain matched, channels were left at nominal 1.4 kV high voltages. Note also that the chosen voltages are conservative, less than the HV settings at which modules had been operated in the HERMES calorimeter.

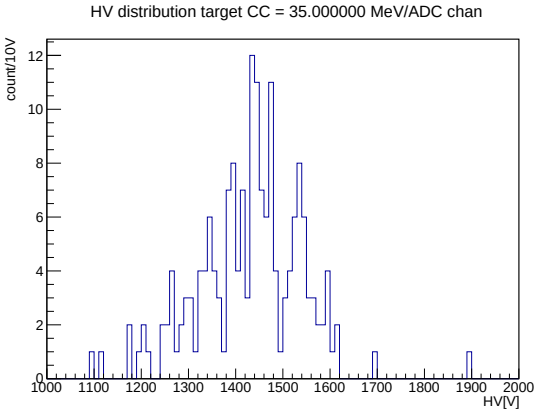

Figure 40: Gain matched high voltage settings for the Shower PMTs (see text for details).

The amplitudes of ADC signals from MIP pions after the gain matching are shown in Fig. 41. The majority of amplitudes are grouped between 20 and 30 ADC channels. The spread in signals among hit channels is much less than in the case of constant supply voltages (compare with Fig. 39).

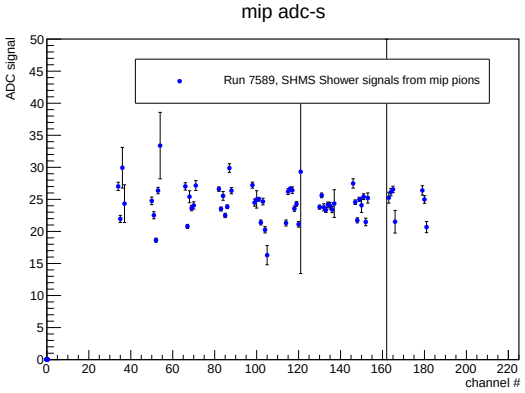

Figure 41: Amplitudes of ADC signals from MIP pions in a set of Shower channels after gain matching.

The Preshower detector was gain matched with cosmic rays prior to installation in the spectrometer. The coincidence of signals from scintillator counters positioned above and below the detector served as a trigger. The gain matching was adjusted after the installation, again with cosmics but this time passing through the de-

tector stack. Muons were identified as events of a single track in the drift chambers and single hit module in the Preshower. A new set of voltages were calculated based on MIP peak positions and according to a formula similar to Eqns 9, 10. The voltages span the range from 1.1 kV to 1.7 kV. The quality of gain matching was insured by taking cosmic data with the new HV settings (Fig. 42).

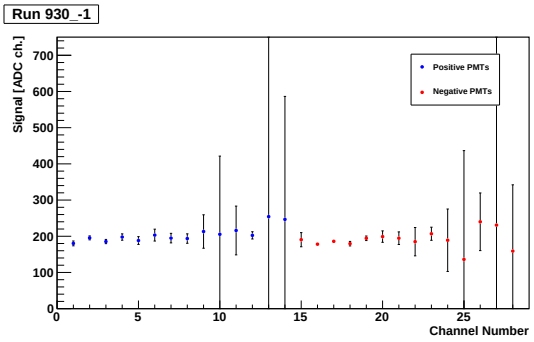

Figure 42: Amplitudes of ADC signals from cosmic muons in the Preshower channels after gain matching.

3.9.8. Calorimeter Calibration

The ability of particle identification of a calorimeter is based on differences in the energy deposition from different types of projectiles. The deposited energy is obtained by converting the recorded ADC channel value of each module into an equivalent energy.

The data analysis procedure corrects for the gain differences in the process of calorimeter calibration. Good electron events are selected by utilising the gas Cherenkov detector(s). The standard calibration algorithm [62] is based on minimization of the variance of the estimated energy with respect to the calibration constants, subject to the constraint that the estimate is unbiased (relative to the primary energy). The momentum of the primary electron is obtained from the tracking in the magnetic field of the spectrometer.

The deposited energy per channel is estimated by

$$e_i = c_i \times A_i, \tag{11}$$

where i is the channel number, c_i is the calibration constant, A_i is the FADC pulse integral signal. Note that the Preshower signals are corrected for the light attenuation dependence versus horizontal hit coordinate y. The calorimeter calibration can be checked by comparing the track momentum to the energy deposition in the calorimeter. The ratio

$$E_{norm} = \frac{P_{Track}}{E_{Dep}}, \tag{12}$$

is referred to as the *normalized energy*. For electrons, E_{Norm} should be equal to 1 as all energy should be deposited in the calorimeter. An example of the normalized energy distribution for electron tracks can be seen before and after a successful calibration in Figs. 43 and 44.

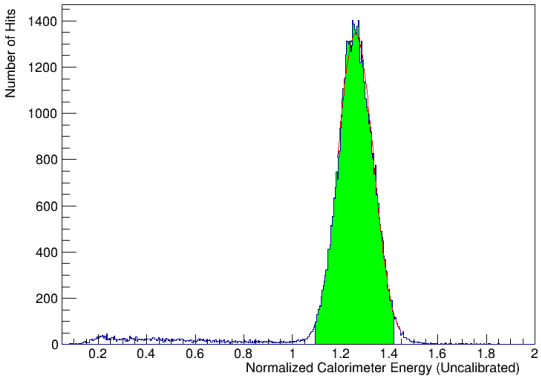

Figure 43: An electron sample (selected through Cherenkov PID) in the calorimeter before calibration. The peak of the E_{Norm} distribution is clearly greater than 1 and is relatively wide.

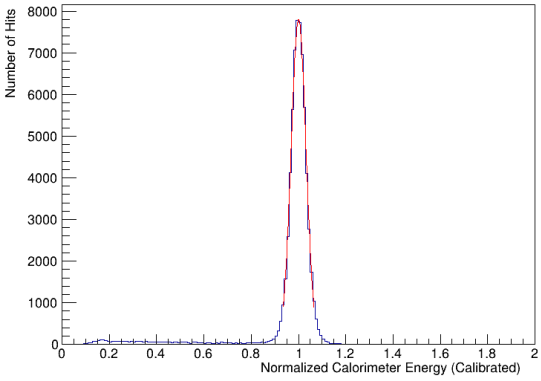

Figure 44: An electron sample (selected through Cherenkov PID) in the calorimeter after calibration. The peak of the E_{Norm} distribution is now much narrower and centered at 1 as expected for electrons.

In the calorimeter analysis code, hits on adjacent blocks in the Preshower and in the Shower are grouped into clusters. For each cluster, the deposited energy and center of gravity are calculated. These clusters are matched with tracks from the upstream detectors if the distance from the track to cluster is less than a predefined "slop" parameter (usually 7.5 cm). For the Preshower, the distance is calculated in the vertical direction.

4. Trigger and Data Acquisition

The Hall C data acquisition (DAQ) system is designed to meet the needs of a high luminosity, dual spectrometer (SHMS + HMS) configuration, with the capability of extracting polarization-dependent absolute cross sections with precision at the 1% level or better. JLab's CODA data acquisition software [63] provides a framework that ties together a distributed network of read-out controllers (ROCs) controlling multiple crates of digitization hardware, event builders to serialize the data, and event recorder processes to write the data to disk. It also provides a graphical control interface for the users.

The Hall C DAQ system can run in dual-arm trigger mode that requires a coincidence between both spectrometers, or each arm's DAQ may be run entirely independently of the other. Incorporating additional detector systems into the standard two-arm design is also straight forward. A high-level block diagram of trigger formation and readout for each spectrometer arm (SHMS or HMS) is depicted in Fig. 45.

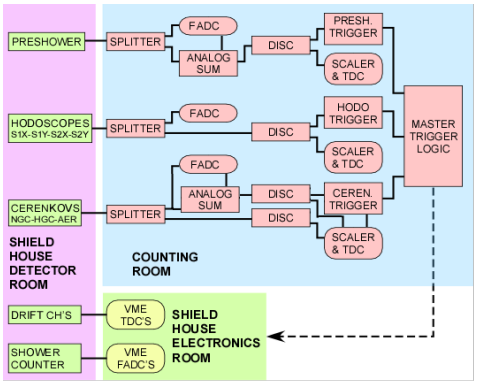

Figure 45: Block diagram of high-level trigger formation for SHMS (and HMS). See Sec. 4.1 for details.

The hardware DAQ and trigger designs were strongly influenced by the preceding 6 GeV HMS and SOS configurations. This choice was made to provide a careful and systematic migration from the very well understood systematics of the 6 GeV system while incorporating and characterizing a new generation of FPGA-based logic and readout electronics. To this end, the present system relies on a combination of legacy NIM and CAMAC discriminators and logic modules to form readout triggers, but utilizes a full set of modern high speed payload and front-end modules to allow a transition to a firmware based trigger and fully pipelined readout in the future.

In the present configuration, the DAQ has a nominal maximum trigger acceptance rate of 4 kHz with a deadtime of ≈20%. Dead times are measured using the Electronic Dead Time Measurement system outlined in Sec. 4.2. The underlying hardware supports running in a fully pipelined mode, and should be capable of running at trigger rates exceeding 20 kHz with minimal deadtime using firmware based triggers similar to those employed in Halls B and D. This capability was not part of the initial 12 GeV upgrade plan for Hall C, but may be pursued in the future (see Sec. 4.5).

Signals from the scintillator planes, Cherenkov detectors, and calorimeter detectors in the SHMS and HMS detector stacks are processed to form *pre-triggers*. Those pre-triggers can serve as *event triggers* themselves (that initiate a recorded event), or be combined to bias data collection towards particular particle types (*i.e.* electrons *vs.* pion) and suppress backgrounds. Each running DAQ can be fed up to six independent triggers simultaneously and the experimenter can control what fraction of each is recorded to disk run-by-run through an integrated pre-scale feature.

4.1. Standard Triggers

All trigger-related PMT signals from both the SHMS and HMS are routed out of the experimental Hall to a dedicated electronics room on the main level of the Hall C Counting House using low-loss RG-8 air-core signal cables. Those signals are then split with one copy running into a JLab F250 flash analog to digital converter (FADC)[64], and the second copy is processed and discriminated. All discriminated pulses are delivered to scalers for rate information, TDCs for precision timing measurement, and to form pre-triggers as described below. This design allows direct access to all raw signals that may participate in a trigger during beam operations and has proven invaluable during the debugging and commissioning phases of Hall operations.

Non-trigger related signals include wire-chamber readouts and the Shower (but not Preshower) layer of the SHMS calorimeter. The readout electronics for those sub-detectors remain inside their respective detector huts within the experimental Hall. All SHMS calorimeter PMT signals are fed into F250 FADCs configured to provide timing, integrated energy, pulse amplitude, and (optionally) pulse profile data as desired. The wire-chamber timing signals are digitized using multi-hit CAEN v1190 modules [65].

The CAEN v1190 payload module provide 128 independent multi-hit/multi-event TDC channels with a user configurable resolution ranging from 52 μs—100 ps per bin. They provide a 32 kilo-word deep output buffer and

can be readout asynchronously with respect to the event triggers. Typical Hall C operation has all units configured for 100 ps/bin.

4.1.1. JLab F250 Flash ADCs

The JLab F250 flash ADC modules are an FPGA-based design developed by the Jefferson Lab Fast Electronics group [64] and are used lab wide. Each F250 module provides 16 independent 50 Ω input channels. The voltage at each input channel is continuously digitized into an 8 μs ring buffer at 250 MHz, with a resolution of 12 bits, and a hardware adjustable full-scale range. When a module receives a readout trigger, digitized sample data stored in the ring buffer is processed in a parallel process that does not incur front-end deadtime. In typical operation each 'hit' over a pre-programmed threshold is assigned an interpolated leading-edge threshold time (<1 ns resolution), integrated energy (analogous to a charge-integrating ADC value), a peak-amplitude, and a measurement of any DC offset (pedestal) present on the channel prior to the detected pulse. Full pulse-profile data for each hit may also be stored if desired. However, that mode increases the data rate by several orders of magnitude, and is generally used only for debugging or limited duration pulse characterization runs.

4.1.2. SHMS Triggers

The SHMS detector stack layout is described in Sec. 3.2. A representative detector layout is presented in Fig. 46.

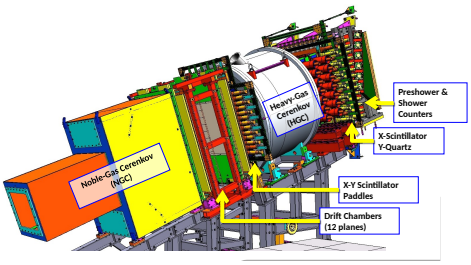

Figure 46: Typical detector layout for the SHMS.

Each hodoscope plane, described in Secs. 3.3 and 3.4, is constructed from an array of horizontal (or vertical) bars with a PMT on each end. Signals from those PMTs are split and one analog copy is delivered to F250 FADCs. The second analog copy is discriminated and sent to CAEN 1190 TDCs for precision timing information, to scalers for raw rate information, and to logic modules to provide the hodoscope pre-triggers plane by plane. A pre-trigger for each plane generated by OR'ing the discriminated signals from each side of a hodoscope plane together, then AND'ing the resulting two signals together. The pre-triggers are designated S1X, S1Y and S2X, S2Y; where 1(2) denote the up(down)stream plane, and X(Y) denote the horizontal(vertical) scintillator bar orientation (see Fig. 47).

It should be noted an optimal design would generate an AND between the PMTs on each side of every bar first, and OR the resulting per-bar coincidences to form a pre-trigger for the plane. The compromise above was driven by constraints of the legacy LeCroy 4564 CAMAC logic units held over from the 6 GeV era.

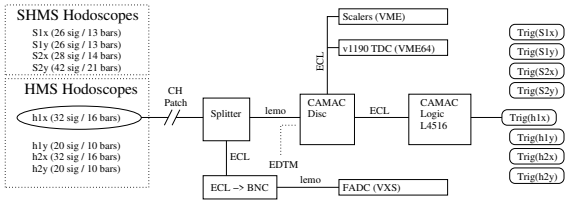

Figure 47: Block diagram for SHMS and HMS hodoscope pre-trigger formation.

The SHMS detector stack includes a permanent Heavy Gas Cherenkov (HGC) (see Sec. 3.6), but also includes space for a *Noble Gas* Cherenkov (NGC) (see Sec. 3.7). Each SHMS gas Cherenkov detector incorporates four PMTs, each detecting light from one of four mirrors inside their respective gas volumes. Analog signals from the PMTs are split (50:50) with one path plugged into an FADC. The second copies from each PMT are summed, and the summed output is discriminated to form a Cherenkov pre-trigger for that Cherenkov detector (HGC and NGC). The pre-triggers are also routed to scaler channels and a v1190 TDC.

An optional SHMS aerogel Cherenkov detector, as detailed in Sec. 3.8, may also be installed. It employs seven PMTs on each side of its diffusion box. The signals from all 14 PMTs are handled analogous to the gas Cherenkov detectors, with each analog signal being split and read out by an individual FADC channel, and second copies being summed and discriminated to form an associated aerogel pre-trigger. The pre-trigger is routed to a scaler and v1190 TDC as well.

A block diagram for the Cherenkov pre-triggers is presented in Fig. 48.

The SHMS Preshower layer, described in Sec. 3.9, consists of 28 lead-glass blocks arranged in 14 rows,

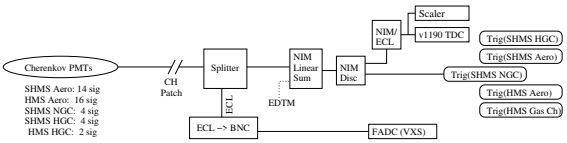

Figure 48: Block diagram for SHMS and HMS Cherenkov pre-trigger formation.

with 2 blocks to a row. Each block is coupled to a single PMT on the side facing the perimeter of the layer. Analog signals from the 28 PMTs are split and summed in 3 groups of 4 rows, and 1 group of 2 rows. Each of the 4 group sums is readout by an FADC channel for cross checks. The 4 group sums are summed in turn to provide a total Preshower sum which is then discriminated and provides the SHMS *PSh* pre-trigger. Provision is made to generate independent pre-triggers for both low- and high- energy depositions in the Preshower layer (*PSh_Lo* and *PSH_Hi*, respectively) as seen in Fig. 49.

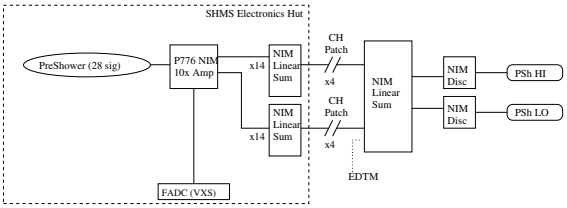

Figure 49: Block diagram for SHMS Preshower summing trigger.

The aforementioned pre-triggers are then combined to form a set of triggers capable of initiating a DAQ event. These combination are often adjusted or optimized to serve the needs of particular experiments but a set of commonly available event triggers is outlined in Sec. 4.1.4.

4.1.3. HMS Triggers

The standard HMS detector stack is the predecessor of the SHMS system and shares a nearly identical design as seen in Fig. 50. It consists of a pair of scintillator-based hodoscope planes in an X+Y configuration, a gas Cherenkov detector, a second pair of X+Y hodoscopes, and a Preshower + Shower Calorimeter. Provision is also made for an optional Aerogel Cherenkov to be inserted into the detector stack just downstream of the drift chambers for supplemental particle identification (PID).

The trigger and readouts designs follow the patterns described in Sec. 4.1.2, with a modest difference associated with the HMS Calorimeter.

Signals from the four HMS hodoscope planes, denoted h1x, h1y, h2x, h2y, are split, discriminated, and

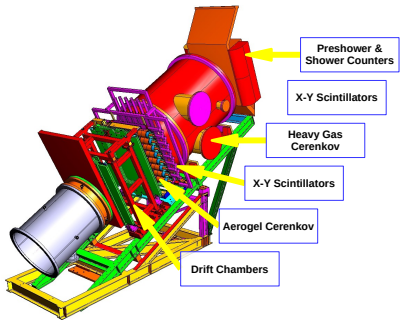

Figure 50: Typical detector layout for the HMS.

recombined to form a *Scin* trigger following the same logic as the SHMS hodoscopes described previously.

The HMS gas Cherenkov detector incorporates two PMTs detecting light from two mirrors inside the HMS Cherenkov tank. Analog signals from the PMTs are split (50:50), with one path plugged into an FADC. The second copies from each PMT are summed, and the summed output is discriminated to form the Cherenkov pre-trigger. That pre-trigger is also routed to a scaler and v1190 TDC.

The HMS Aerogel employs eight PMTs on each side of its diffusion box. The signals from all 16 PMTs are split and readout by an individual FADC channel, with the second copies being summed and discriminated to form the associated aerogel pre-trigger. The pre-trigger is routed to a scaler and v1190 TDC as well.

The HMS calorimeter is composed of four layers of lead glass blocks. Each layer has 13 lead-glass blocks arranged horizontally, and the layers are denoted A, B, C and D as seen by a particle passing through the detector stack. Layers A and B have PMTs bonded to each end of their blocks, while Layers C and D have a single PMT on one side only. Analog signals from the PMTs are split 50:50 with one copy being delivered to an FADC. The copies are formed into an analog sum for each side of each layer, denoted hA+, hA-, hB+, hB-, hC, and hD. Layer sums hA and HB are formed by summing hA+ and hA-, and hB+ and hB-, respectively (hC and hD are already layer sums).

One copy of each layer sum is sent to an FADC for monitoring and cross checks. A Preshower pre-trigger is formed by summing and discriminating Layers A + B, and a *Shower Low* pre-trigger is formed by summing and discriminating Layers A+B+C+D. Copies of the Preshower and Shower sums are sent to FADCs and copies of the discriminated pre-trigger signals are sent to scalers and 1190 TDCs.

Fig. 51 depicts a block diagram of the HMS Calorimeter pre-triggers.

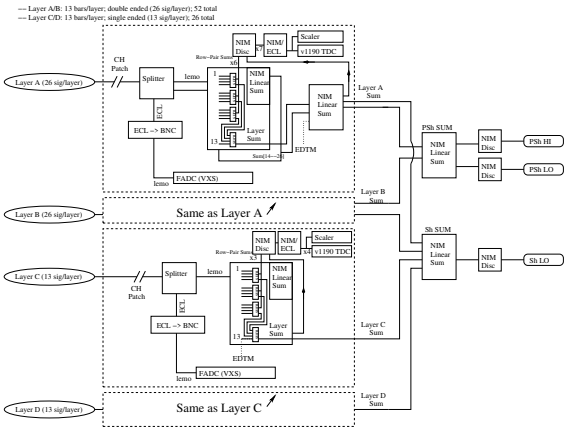

Figure 51: Block diagram for HMS Shower and Preshower summing triggers.

4.1.4. Event Triggers

The aforementioned pre-triggers are then combined to form a set of triggers capable of initiating a DAQ event. The 'default' single-arm trigger is formed by 3 out of 4 hodoscope planes firing in coincidence. Often referred to as the *3 of 4* or *Scin* trigger, it provides a high-efficiency (> 99%) general-purpose charged particle trigger.

A second standard trigger is referred to as *EL_Clean*. It implements particle discrimination at the trigger level by forming a coincidence between the *Scin* pre-trigger, one (or more) Cherenkov pre-triggers, and (optionally) the pre-shower (*PSh*) and/or calorimeter total-sum (*ShTot* pre-triggers).

4.2. Electronic Dead Time Measurement System (EDTM)

The DAQ and trigger system for each spectrometer also includes an Electronic Dead Time Measurement (EDTM) system. This is implemented by replicating a pulse from a pulse-generator circuit and feeding into every pre-trigger leg as close to the analog signals as possible. The timing of those duplicated pulses is adjusted to match those generated by a real particle passing through the detector stack. A copy of each synthetic EDTM trigger is counted in a deadtime free scaler and sent to a dedicated TDC channel in each arm. The presence of an appropriately timed hit in that TDC channel tags an event as having been generated by an EDTM trigger.

During beam operations, this allows a direct measurement of the fraction of triggers that are lost due to some component of the DAQ being busy. This is known as the system *deadtime*. By inducing synthetic signals as early in the trigger electronics as possible, this system is sensitive to high-rate signal pile-up in the full front-end trigger logic chain, as well as digitization and read out related deadtimes implicit in the non-pipelined DAQ operation presently in use in Hall C.

In addition to the above function, the system has proved useful for pre-beam trigger verification and end to end checkout of the DAQ system.

- It allows rough timing on all trigger legs to be verified without beam.
- It allows coincidence timing between the SHMS and HMS arms to be roughed in and tested without beam.
- It allows the entire DAQ system to be stress tested under controlled conditions without beam.

4.3. Auxiliary Data Collection

The standard method for slow controls data logging is through the Experimental Physics and Industrial Control System (EPICS) [66]. EPICS is a system of open source software tools and applications used to provide control user interfaces and data logging for systems such as high- and low-voltage detector power supplies, target systems, spectrometer magnets, vacuum, and cryogenic systems, etc.

Long-term, persistent storage of EPICS based slow controls data is provided through an independent archiving system managed by the Accelerator Division's MYA archiving system. An experimentally relevant subset of EPICS data (beam and target characteristics; magnet, spectrometer and detector settings, etc.) are also stored in the experimental data files at regular intervals whenever the DAQ is running.

4.4. Online Hall C Computing Environment

Hall C employs a dedicated stand-alone computing cluster with redundant multi-core servers focused on prompt online analysis, high volume local data storage, and 1–10 Gb ethernet interconnects. There are dedicated hosts for each independent DAQ system (*ex.* SHMS and HMS), and auxiliary machines for polarimetry, target controls, spectrometer slow controls, etc.

Experimental control and operational feedback is provided to users in the Hall C Counting house through a collection of multi-screen computer workstations and a set of large wall-mounted displays for critical data.

All systems have direct access to the JLab centrally managed Scientific Computing resources. This includes multi-petabyte tape storage and online disk facilities, as well as a several thousand core compute farm for simulation and offline data analysis [67].

4.5. Future Plans / Pipeline trigger

During the early stages of the 12 GeV Hall C upgrade plan, it was concluded that the risks of moving to a fully pipelined DAQ system with a firmware driven trigger were not justified by the needs of the initial experimental program. In general, those experiments did not impose a too heavy burden on the DAQ, and the more conventional trigger design with its well understood characteristics was preferred.

However, provision was made to design and build the low-level DAQ system with an upgrade path in mind. To that end, a full compliment of trigger and payload modules compatible with the pipelined systems being implemented for Halls B and D was selected.

A phased transition from the NIM/CAMAC trigger system to a fully pipelined approach would involve implementing the present trigger logic within the existing JLab FADC and VXS Trigger Processor (VTP) boards, and a thorough validation of the firmware based trigger decisions against the well understood conventional trigger. Once the firmware is fully debugged/characterized, the DAQ could transition to pipelined mode and take advantage of significant boost in trigger accept rates into the 10's of kHz range with minimal deadtime. At that point, the next DAQ bottleneck would likely be rate limitations in the detector systems themselves (signal pile-up in the front-end, track reconstruction limitations, etc.)

5. Software

Hall C Data is analyzed by the Hall C analysis package `hcana`. This package does full event reconstruction for the SHMS used alone or in coincidence with other detectors. `hcana` is based on the modular Hall A `analyzer` [68] ROOT [69] based C++ analysis framework. This framework provides for run time user configuration of histograms, ROOT tree contents, cuts, parameters and detector layout.

`hcana` includes C++ classes for detectors, spectrometers, and physics analyses. Instantiation of these classes as objects is configured at run-time through a ROOT script which also sets up the configuration of analysis replay. Due to the similarity of the SHMS and HMS spectrometers and their detector packages, the same spectrometer and detector classes are used for both spectrometers. For example, the drift chamber package class is instantiated for both spectrometers with each object configured by its specific parameters and geometry. Additional modules such as new front end decoders, detectors, or physics analysis modules can easily be added to `hcana`. These modules can either be compiled into the analyzer or be compiled separately and dynamically loaded at run time.

Event analysis is segmented into 3 steps of spectrometer and detector specific analysis.

1. Decoding: Detector requests from the low level decoder produce a list of hits sorted detector by plane and counter number. A minimal amount of processing is done to make data available for low level histograms.
2. Coarse Processing: Tracks are found in the drift chambers. Hits and clusters in the hodoscope, shower counter and other detectors are matched to the tracks to determine time-of flight. The various detectors provide information for particle identification.
3. Fine processing: Particle identification information is refined, tracks in the focal plane are traced back to the target coordinate system and particle momentum is determined.

Each step of these steps is completed for all detectors before proceeding to the next step. Some limited information is passed between detectors at each step. For example, timing information from the hodoscopes is used to obtain the start time for the the drift chambers in the decoding step and tracks obtained from the drift chambers are associated with shower counter hit clusters in the fine processing step.

After these steps, single arm and coincidence physics quantities are calculated using various physics analysis classes that are configured at run-time.

5.1. Online Monitoring

After each data taking run (typically an hour or less) is started, a subset of the data is analyzed with `hcana`. An easily configurable histogram display GUI is used to view diagnostic histograms and compare them to reference histograms. The EPICS [66] control system alarm handler is used to monitor experiment settings and beam conditions. This includes spectrometer magnet settings, detector high voltages, drift chamber gas, cryogenic systems and spectrometer vacuum.

6. SHMS Performance: Operating Experience and Commissioning Results

6.1. Acceptance

The acceptance of the SHMS can be determined from simulation and defined as $A(\delta,\theta) = N_{sus}(\delta,\theta)/N_{gen}(\delta,\theta)$, where N_{gen} is the number of events generated into a particular δ,θ bin and N_{sus} is the number of events that successfully reached the detector stack. Since $A(\delta,\theta)$ depends on the generation limits of the simulation, a more useful quantity is the effective solid angle, $\Delta\Omega_{eff} = A(\delta,\theta) * \Delta\Omega_{gen}$, where $\Delta\Omega_{gen}$ is the solid angle generated into for each bin. Fig. 52 shows the effective solid angle of the SHMS at a central angle of 21° and central momentum of 3.3 GeV/c for a 10 cm liquid hydrogen target.

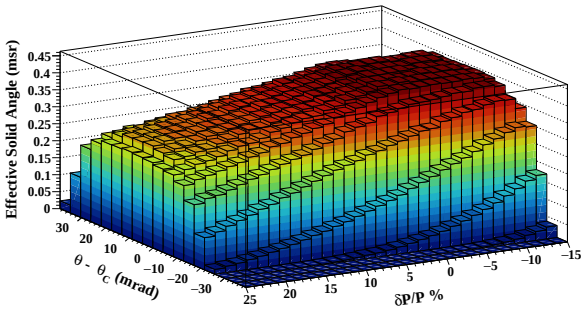

Figure 52: SHMS effective solid angle as a function of $\delta P/P$ and θ. SHMS $\theta_{central} = 21^\circ$ and $P_{central} = 3.3\,GeV/c$.

Fig. 53 shows the position and angular distribution of tracks formed from the drift chambers at the focal plane. A good agreement between the two reflects our understanding of both the magnetic forward transport and physical locations of the apertures which determine the acceptance.

Fig. 54 demonstrates the agreement between simulation (after subtracting the cell walls) of the target variables $x_{tar}, y'_{tar}, x'_{tar}$, and δ that were described in Sec. 3.1.

To demonstrate how large the SHMS acceptance is in y_{tar}, optics data were taken during the A_1^n experiment. Fig. 55 plots the reconstructed position along the beam line, z_{tar} (which was reconstructed using the measured and y'_{tar}).

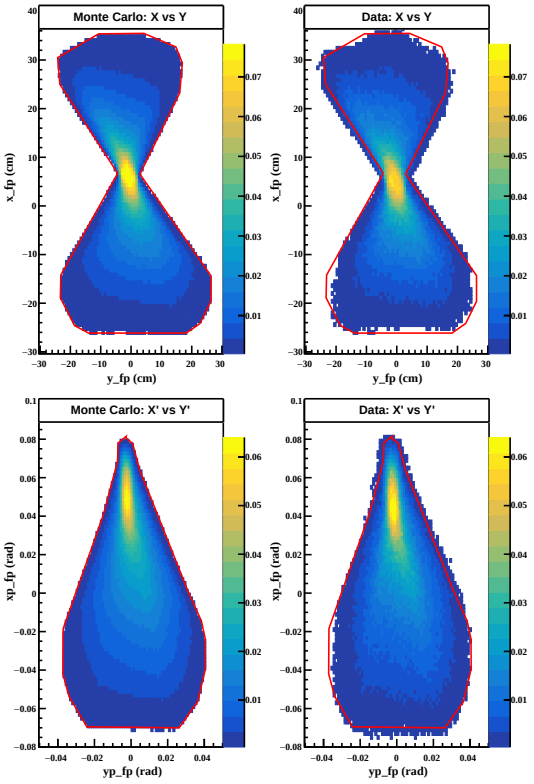

Figure 53: Comparison of SHMS focal plane quantities, simulation is on the left and data is on the right. The top plots are the position at the focal plane and the bottom is the angles at the focal plane determined from tracks formed by the drift chamber planes. The red outline represents the expected shape determined from simulation.

6.2. Rates and Live time

6.2.1. Dead time Measurement by Electronic Pulse Generator

The computer live time efficiency of the DAQ is defined as

$$\epsilon_{\mathrm{CLT}} = \frac{N_{(\mathrm{phy+edtm}),\mathrm{TDC}} - N_{(\mathrm{edtm}),\mathrm{TDC}}}{N_{(\mathrm{phy+edtm}),\mathrm{SCL}} - N_{(\mathrm{edtm}),\mathrm{SCL}}}, \qquad (13)$$

where the numerator is the total number of EDTM-subtracted TDC counts (total accepted physics triggers) and the denominator is the total number of EDTM-subtracted scaler counts (total physics pre-triggers). The EDTM introduces a bias in the computer live time calculation and must therefore be subtracted from the physics trigger. The bias comes from the fact that the the EDTM is a clock and cannot be blocked by another EDTM signal, thereby having no contribution to the deadtime of the system. An additional bias arises during beam-off time periods, where only EDTM triggers are counted. To remove this bias, a beam current cut was required in the live time calculation.

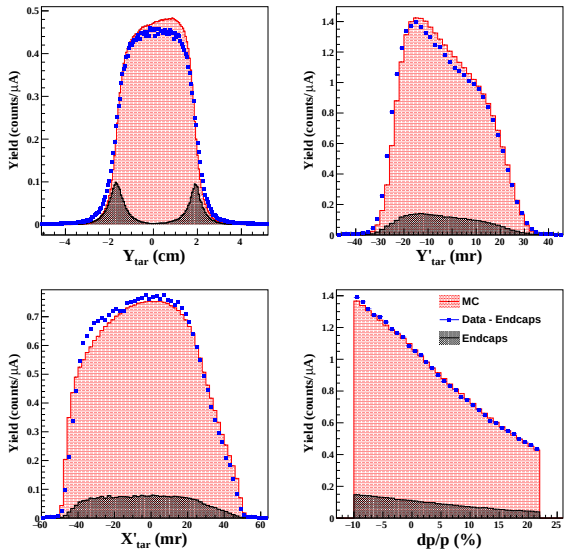

Figure 54: Target variable comparison of data versus Monte Carlo simulation from [10]. After subtracting the aluminum cell walls (black histogram) of the hydrogen target using dummy foil data, the agreement between data (blue histogram) and Monte Carlo (red histogram) is reasonable.

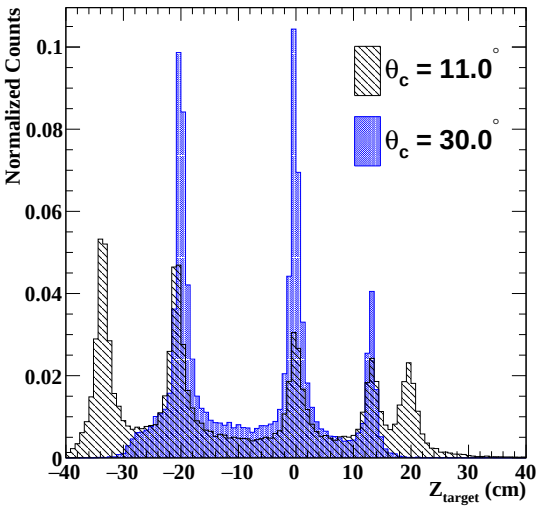

Figure 55: Reconstructed z_{tar} for a carbon foil optics target at SHMS central angles of 11° and 30°. Carbon foils were located at approximately -20, 0, 13.3 and 20.0 cm. The peak located at -35 cm is from the beam pipe exit window. The target chamber was not under vacuum and therefore a background from air is present in the data and not subtracted here.

The computer live time data shown in Fig. 56 is plotted against the un-prescaled input trigger rates (top x-axis) and the first plane (S1X) of the SHMS Hodoscopes (bottom-axis). The data were obtained from the SHMS luminosity scans and the Kaon LT experimental data taken on Fall 2018. The Spring 2018 scans (blue squares) were taken with DAQ in buffer level 1 (unbuffered mode) and the Kaon LT data (green triangles) and Fall 2018 scans (red circles) were with the DAQ in buffer level 10 (buffered mode). The advantage of buffered mode is that the DAQ is capable of accepting higher trigger rates while keeping the computer live time efficiency $\sim$ 100%. Both buffered and unbuffered modes exhibit a characteristic fall-off of the live time as a function of the trigger rate which has been modeled using the fit function,

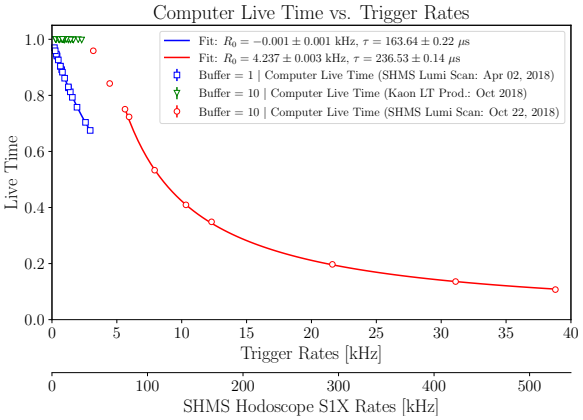

Figure 56: Computer live time vs. trigger rates (top x-axis) and SHMS hodoscope S1X plane rates (bottom x-axis) for DAQ buffer levels 1 and 10.

$$f_{\epsilon_{\rm CLT}}(R) \equiv \frac{1}{1+(R-R_0)\tau}, \tag{14}$$

where R is the input trigger rate, R_0 describes a horizontal offset between the unbuffered and buffered modes and τ represents the averaged data readout time (deadtime) before the DAQ is ready to accept another pretrigger. The fit function, however, is unable to describe the "flat" region where the live time is nearly 100 %. From the fit parameters, the fall-off behavior of buffered mode starts at trigger rates, $R \sim 1/\tau$, which corresponds to a numerical values of $\sim$ 4.2 kHz before a significant drop in the live time is observed.

Since fall 2018, the DAQ has been operated in buffered mode which has proved to be more feasible for current and future high-rate experiments at Hall C.

6.3. Subsystem Performance

6.3.1. Hodoscope Performance

All hodoscope scintillator paddles and the PMTs used on the S1X, S1Y, and S2X planes were extensively

tested during assembly: the dark current and the gain as a function of the high voltage were measured for each tube; the finished paddles were light-leak tested and their detection efficiency as a function of position along the paddle was measured using cosmic rays on an automated test stand. A typical gain versus HV graph is shown in Fig. ,57.

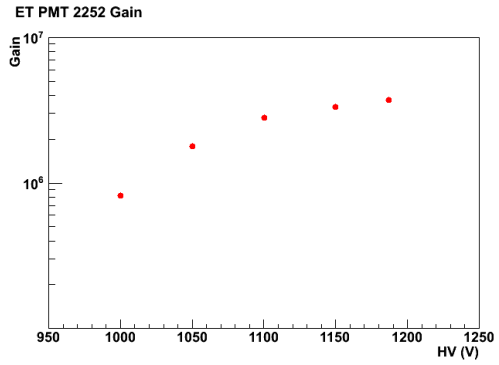

Figure 57: Gain versus high voltage graph for an ET tube used for the scintillator hodoscope.

Once installed in the SHMS detector hut, all paddles were retested and gain matched. During the Hall C commissioning experiments, carried out during spring 2018, the scintillators performed as expected with no major problems. The hodoscope efficiency as a function of S1X rate (first hodoscope plane) can be seen in Fig. 58.

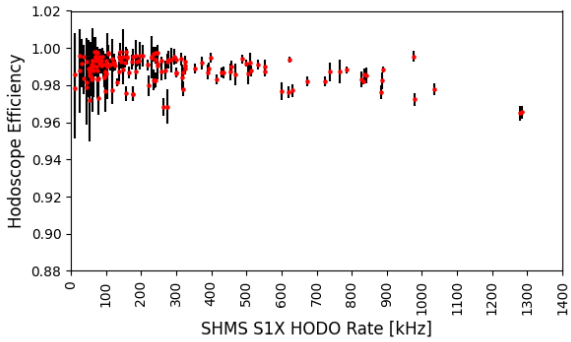

Figure 58: Hodoscope efficiency as a function of rate in the first hodoscope plane, S1X.

The performance of the quartz plane (S2Y) was studied with beam during the Hall C commissioning in Fall of 2017. A plot of the photoelectron response from most bars in the quartz plane is shown in Figs. 59 and 60. Only electrons with an incident angle close to 90° were chosen here to eliminate the bias coming from possibly reduced photon collection efficiency due to sub-optimal angles of the photon cones. All PMTs and optical couplings performed satisfactory.

The threshold for Cherenkov light production in the quartz bars for electrons, pions, kaons and protons is shown in Fig. fig:TBD. Beam data confirmed the expectation that the detection efficiency for low momentum protons, for example, will be smaller than that for pions or electrons simply due to the reduced number of Cherenkov photons that particles close to their firing threshold will produce. This is exemplified by Figs. 61, 62 and 63.

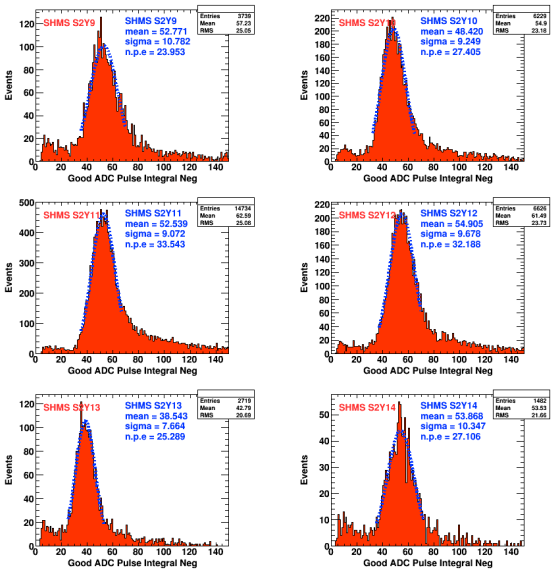

Figure 59: Number of photoelectrons response from the quartz plane, negative end PMTs.

6.3.2. *DC Performance*

The SHMS drift chambers have proven to provide reliable tracking for electrons and hadrons across a broad range of momenta. The drift chambers have also performed very well at high rate, with tracking efficiencies exceeding 96%, even at pre-trigger rates over 2 MHz. The tracking efficiency as a function of the S1X hodoscope trigger rate (a good proxy for the overall event rate) in the SHMS can be seen in Figs. 64 and 65.

Comment on tracking resolution?

6.3.3. *HGC Performance*

The performance of the HGC is determined by the capacity to separate particle species on the basis of

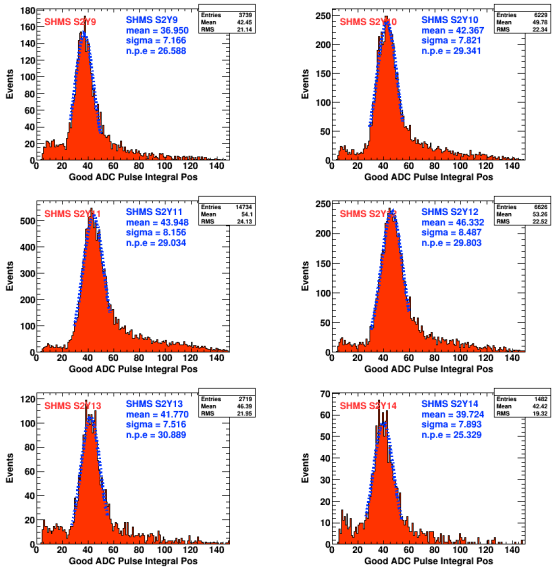

Figure 60: Number of photoelectrons response from the quartz plane, positive end PMTs.

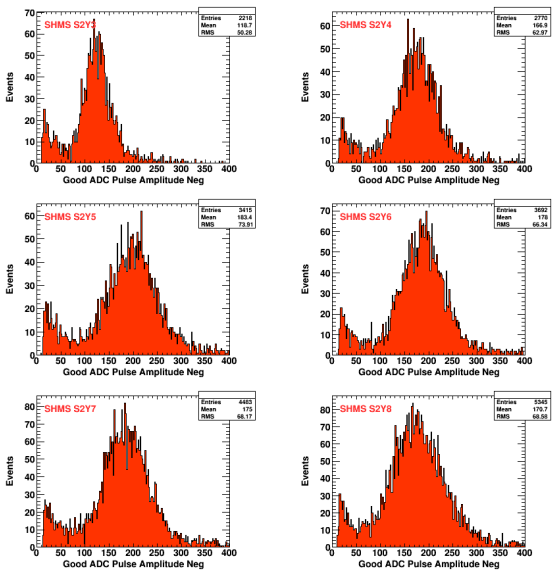

Figure 61: PMT pulse amplitude from pions with momenta of 1.96 GeV/c.

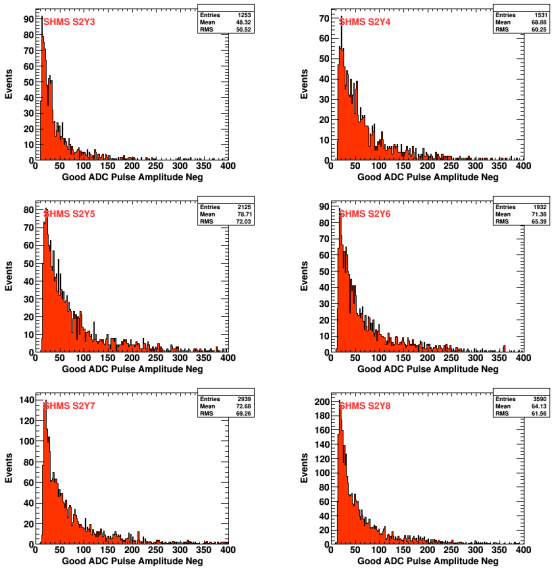

Figure 62: PMT pulse amplitude from protons with momenta of 1.96 GeV/c.

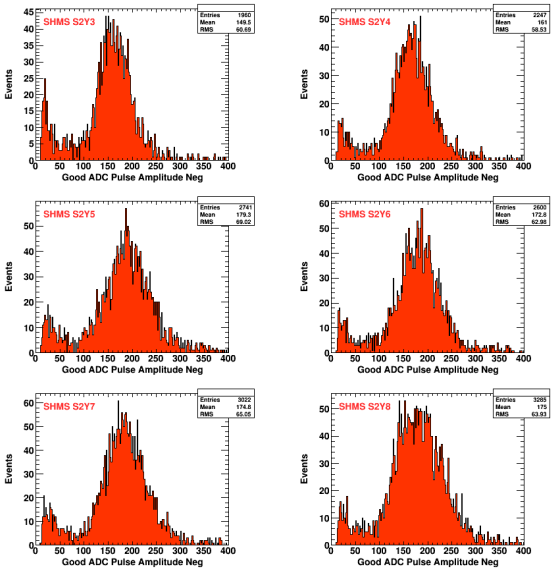

Figure 63: PMT pulse amplitude from protons with momenta of 5.05 GeV/c.

produced number of photoelectrons (NPE). In particular, the HGC is a threshold Cherenkov detector and thus identifies species based on whether or not a signal greater than 1.5 NPE was generated or not. The first metrics of performance to be discussed are the detector efficiency and contamination.

Efficiency in this context refers to the ratio of events selected as a particular particle species by all detectors in the SHMS, including the HGC, over the number of events selected as that same species without any information from the HGC. This is illustrated by the equation

$$\eta_{\text{HGC}} = \frac{\pi^+ \text{ detected with HGC signal}}{\pi^+ \text{ detected without HGC signal}}, \qquad (15)$$

where η_{HGC} represents the detector efficiency of the HGC and π^+ particle type is used as an example. The

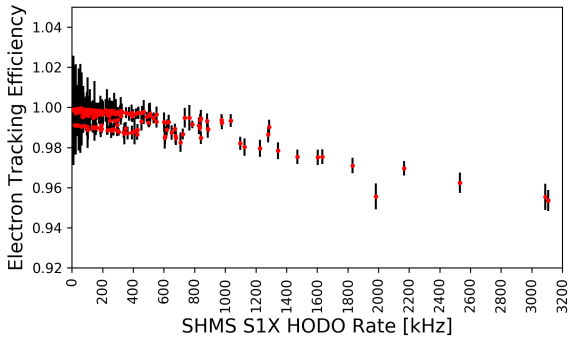

Figure 64: The SHMS electron tracking efficiency as a function of the S1X hodoscope trigger rate.

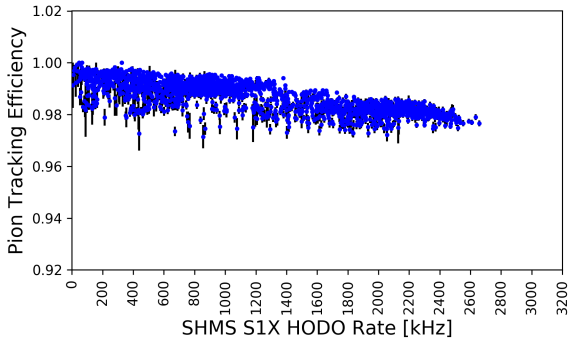

Figure 65: The SHMS pion tracking efficiency as a function of the S1X hodoscope trigger rate.

selection criteria include cuts on the timing information, reconstructed β, calorimeter, aerogel and HGC information, and a single reconstructed track per event. Contamination refers to the number of events identified as a sub-threshold particle by the calorimeter and aerogel Cherenkov, but produced more than 1.5 NPE in the HGC. For example, if the HGC is configured for π^+/K^+ separation, the $K+$ contamination is defined as the number of events identified as a K^+ by all detectors, except the HGC, which identified a π^+.

PID Configuration	Efficiency	Contamination
e^-/π^-	95.99%	10000 : 1
π^+/K^+	98.22%	1000 : 1

Table 5: Summary of the Heavy Gas Cherenkov performance in separating between particle species. Efficiency is based on a photoelectron cut greater than 1.5.

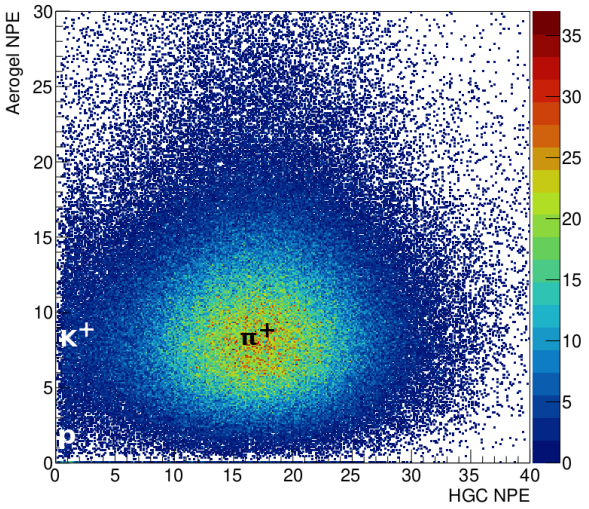

Figure 66: Demonstration of the particle identification capability of the Heavy Gas Cherenkov. Pictured is the separation between π^+, K^+ and proton at the 8.186 GeV beam energy and 6.053 GeV/c SHMS central momentum. The refractive indexes of HGC and aerogel Cherenkov detectors are 1.00143 and 1.011, respectively.

Two runs are chosen to show HGC efficiency and contamination, one where the HGC separated between e^-/π^- and the other π^+/K^+. The former featured the HGC filled with CO_2 at 1 atm and a SHMS central momentum of -3.0 GeV/c. Particle identification was established by a cut on the normalized calorimeter energy. The latter had the HGC filled with C_4F_{10} at 1 atm, giving a π momentum threshold of 2.8 GeV/c and a K momentum threshold of 9.4 GeV/c, at a SHMS central momentum of +5.05 GeV/c. Particle identification was performed by a cut on the aerogel Cherenkov detector and the normalized calorimeter energy. The spectrum obtained for the π^+/K^+ separation is shown in Fig. 66. This figure illustrates the broad distribution of NPE produced by π^+ above their momentum threshold. At the lower end of the NPE axis, there is a large number of events producing no light, or just the SPE. These events correspond to K^+, since they are below the momentum threshold to produce Cherenkov light. The presence of the SPE is likely due to δ-rays, or knock-on e^-, a phenomenon where a kaon can ionize the Cherenkov media and produce e^- which produce Cherenkov radiation. A summary of the particle identification efficiency and contamination is shown in Table 5.

Lastly, measurements of the π efficiency across a variety of momentum settings can be used to verify the index of refraction of the Cherenkov media. The relationship between π efficiency and momentum is fit with

the equation [70]

$$\eta_{HGC} = 1 - e^{-(p-p_o)/\Gamma}, \quad (16)$$

where η_{HGC} is the detector efficiency, p is the momentum of the π, and p_o and Γ are free parameters. Data taken in the range of 2.53 GeV/c to 5.05 GeV/c with the HGC filled with C_4F_{10} yields an index of refraction of $n = 1.001 \pm 0.002$. This is in agreement with the accepted value of $n = 1.00143$ [71]. Additional performance details are given in [72].

Add a plot showing efficiency across HGC, comment on drop in centre due to mirror positioning.

6.3.4. NGC Performance

The primary purpose of the NGC in the SHMS is to distinguish electrons from pions. Typically, PID is determined by utilizing a cut on the number of photoelectrons detected in the NGC. This cut is usually set at X photoelectrons. As this is a threshold Cherenkov, any events with less than the cutoff are identified as pions (or heavier hadron) and any with more than the cutoff are electrons.

Comment/discussion on the NGC performance.

6.3.5. Aerogel Performance

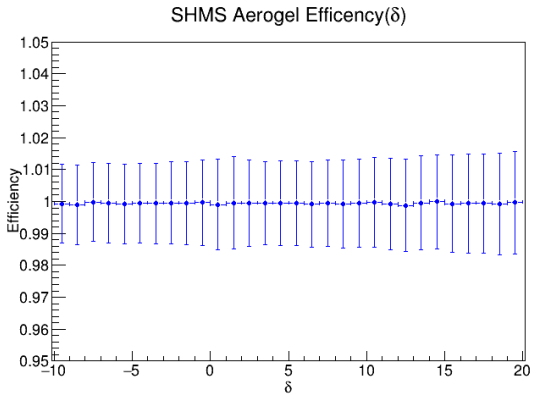

Figure 67: The efficiency of the aerogel is plotted over a range of δ. This efficiency is taken at a beam energy of 6.2 GeV for an SHMS central momentum of 3.486 GeV/c. The refractive index of the aerogel detector is 1.015.

PID Configuration	Efficiency	Contamination
K^+/p	99.94%	1000 : 1

Table 6: Aerogel performance for kaon-proton separation with efficiency based off of cut greater than 1.5 photoelectrons.

The primary use of the aerogel Cherenkov detector in the SHMS is to distinguish between kaons and protons. A variety of aerogel tile refractive indices are used to cover a range of momenta. A cut of greater than 1.5 photoelectron (NPE) is used to cleanly identify particles. Fig. 66 shows the particle identification of the Heavy Gas Cherenkov as well as the aerogel Cherenkov detector. This figure shows the importance of having both the Heavy Gas and the aerogel Cherenkov detectors as the kaon and proton would be indistinguishable without the aerogel.

In order to get clean kaon samples, a high detector efficiency in the aerogel is required. The efficiency is determined by

$$\eta_{\text{aero}} = \frac{K^+ \text{ detected with aerogel signal}}{K^+ \text{ detected without aerogel signal}}, \quad (17)$$

where the detector efficiency is represented by η_{aero}. The efficiency of the aerogel detector can be seen in Table 6. It is clear that the aerogel has a very high efficiency, crucially though, this efficiency also runs over the full range of δ as seen in Fig. 67. This, plus the ability to change refractive indices, allows for terrific kaon identification over a wide range of kinematics.

6.3.6. Calorimeter Performance

Material on the gain stablity/consistency to be added (resolution versus run number for a time period, or mip peak position versus run number).

The performance of the SHMS calorimeter under beam conditions was tested first time during 12 GeV Hall C Key Performance Parameter Run in spring of 2017. As part of the SHMS detector package, the calorimeter was commissioned in the Hall C fall run period of the same year.

As discussed briefly in Sec. 3.9.8, E_{Norm} should be 1 for electrons. This quantity can be utilised for PID selection. In the few GeV/c range, pions and electrons are well separated as can be seen in Fig. 7. The early analyses of the calorimeter data also demonstrate satisfactory performance of the detector in terms of resolution, as demonstrated in Fig. 68.

7. Conclusion

The SHMS has been in service since 2017. Through a range of experiments that utilised a broad range of run conditions, the SHMS has demonstrated itself to be a reliable and stable spectrometer, both in terms of its ion optics, and its detector package.

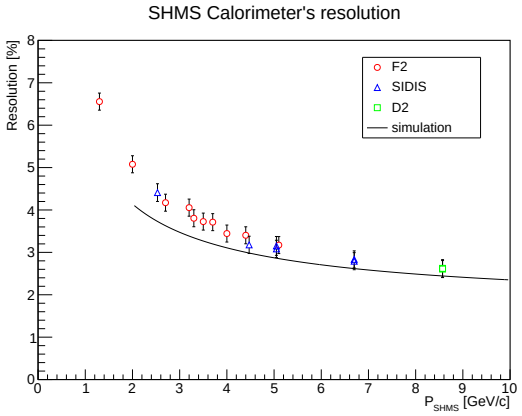

Figure 68: Resolution of the SHMS calorimeter from calibrations of runs from the Spring 18 run period. The solid line is result from the early simulations. [**This figure is not final.**]

Numerous experiments have completed and published high profile results since the SHMS was commissioned in 2017. This includes many high profile results on color transparency [73, 74], the EMC effect [75], deuteron structure [76] and proton structure [77]. This also extends to detailed studies of the proton's gravitational form factors [78].

Many more high profile scientific results are expected in the near future, with several experimental campaigns now completed and data analysis in advanced stages. Due to the design parameters of the SHMS, it could also be utilised extensively in an upgraded, 22 GeV Jefferson Lab Scenario. Some possible experiments and scenarios that utilise the SHMS in a 22 GeV era are outlined in the 22 GeV white paper [79].

Acknowledgments

This material is based upon work supported bythe U.S. Department of Energy, Office of Science, Office of Nuclear Physics under contract DE-AC05-06OR2317. This work is supported by the Natural Sciences and Engineering Research Council of Canada (NSERC) SAPIN-2021-00026 and an award from the SAP-RTI program.

References

[1] I. Niculescu, C. S. Armstrong, J. Arrington, K. A. Assamagan, O. K. Baker, D. H. Beck, C. W. Bochna, R. D. Carlini, J. Cha, C. Cothran, D. B. Day, J. A. Dunne, D. Dutta, R. Ent, B. W. Filippone, V. V. Frolov, H. Gao, D. F. Geesaman, P. L. J. Gueye, W. Hinton, R. J. Holt, H. E. Jackson, C. E. Keppel, D. M. Koltenuk, D. J. Mack, D. G. Meekins, M. A. Miller, J. H. Mitchell, R. M. Mohring, G. Niculescu, D. Potterveld, J. W. Price, J. Reinhold, R. E. Segel, P. Stoler, L. Tang, B. P. Terburg, D. Van Westrum, W. F. Vulcan, S. A. Wood, C. Yan, B. Zeidman, Experimental verification of quark-hadron duality, Phys. Rev. Lett. 85 (2000) 1186–1189. doi:10.1103/PhysRevLett.85.1186.

[2] V. Tvaskis, M. E. Christy, J. Arrington, R. Asaturyan, O. K. Baker, H. P. Blok, P. Bosted, M. Boswell, A. Bruell, A. Cochran, L. Cole, J. Crowder, J. Dunne, R. Ent, H. C. Fenker, B. W. Filippone, K. Garrow, A. Gasparian, J. Gomez, H. E. Jackson, C. E. Keppel, E. Kinney, L. Lapikás, Y. Liang, W. Lorenzon, A. Lung, D. J. Mack, J. W. Martin, K. McIlhany, D. Meekins, R. G. Milner, J. H. Mitchell, H. Mkrtchyan, B. Moreland, V. Nazaryan, I. Niculescu, A. Opper, R. B. Piercey, D. H. Potterveld, B. Rose, Y. Sato, W. Seo, G. Smith, K. Spurlock, G. van der Steenhoven, S. Stepanyan, V. Tadevosian, A. Uzzle, W. F. Vulcan, S. A. Wood, B. Zihlmann, V. Ziskin, Longitudinal-transverse separations of deep-inelastic structure functions at low Q^2 for hydrogen and deuterium, Phys. Rev. Lett. 98 (2007) 142301. doi:10.1103/PhysRevLett.98.142301.

[3] J. Volmer, D. Abbott, H. Anklin, C. Armstrong, J. Arrington, K. Assamagan, S. Avery, O. K. Baker, H. P. Blok, C. Bochna, E. J. Brash, H. Breuer, N. Chant, J. Dunne, T. Eden, R. Ent, D. Gaskell, R. Gilman, K. Gustafsson, W. Hinton, G. M. Huber, H. Jackson, M. K. Jones, C. Keppel, P. H. Kim, W. Kim, A. Klein, D. Koltenuk, M. Liang, G. J. Lolos, A. Lung, D. J. Mack, D. McKee, D. Meekins, J. Mitchell, H. Mkrtchyan, B. Mueller, G. Niculescu, I. Niculescu, D. Pitz, D. Potterveld, L. M. Qin, J. Reinhold, I. K. Shin, S. Stepanyan, V. Tadevosyan, L. G. Tang, R. L. J. van der Meer, K. Vansyoc, D. Van Westrum, W. Vulcan, S. Wood, C. Yan, W.-X. Zhao, B. Zihlmann, Measurement of the charged pion electromagnetic form factor, Phys. Rev. Lett. 86 (2001) 1713–1716. doi:10.1103/PhysRevLett.86.1713.

[4] T. Horn, K. Aniol, J. Arrington, B. Barrett, E. J. Beise, H. P. Blok, W. Boeglin, E. J. Brash, H. Breuer, C. C. Chang, M. E. Christy, R. Ent, D. Gaskell, E. Gibson, R. J. Holt, G. M. Huber, S. Jin, M. K. Jones, C. E. Keppel, W. Kim, P. M. King, V. Kovaltchouk, J. Liu, G. J. Lolos, D. J. Mack, D. J. Margaziotis, P. Markowitz, A. Matsumura, D. Meekins, T. Miyoshi, H. Mkrtchyan, I. Niculescu, Y. Okayasu, L. Pentchev, C. Perdrisat, D. Potterveld, V. Punjabi, P. Reimer, J. Reinhold, J. Roche, P. G. Roos, A. Sarty, G. R. Smith, V. Tadevosyan, L. G. Tang, V. Tvaskis, S. Vidakovic, J. Volmer, W. Vulcan, G. Warren, S. A. Wood, C. Xu, X. Zheng, Determination of the pion charge form factor at $Q^2 = 1.60$ and 2.45 $(\mathrm{GeV}/c)^2$, Phys. Rev. Lett. 97 (2006) 192001. doi:10.1103/PhysRevLett.97.192001.

[5] T. Navasardyan, G. S. Adams, A. Ahmidouch, T. Angelescu, J. Arrington, R. Asaturyan, O. K. Baker, N. Benmouna, C. Bertoncini, H. P. Blok, W. U. Boeglin, P. E. Bosted, H. Breuer, M. E. Christy, S. H. Connell, Y. Cui, M. M. Dalton, S. Danagoulian, D. Day, T. Dodario, J. A. Dunne, D. Dutta, N. El Khayari, R. Ent, H. C. Fenker, V. V. Frolov, L. Gan, D. Gaskell, K. Hafidi, W. Hinton, R. J. Holt, T. Horn, G. M. Huber, E. Hungerford, X. Jiang, M. Jones, K. Joo, N. Kalantarians, J. J. Kelly, C. E. Keppel, V. Kubarovski, Y. Li, Y. Liang, S. Malace, P. Markowitz, E. McGrath, P. McKee, D. G. Meekins, H. Mkrtchyan, B. Moziak, G. Niculescu, I. Niculescu, A. K. Opper, T. Ostapenko, P. Reimer, J. Reinhold, J. Roche, S. E. Rock, E. Schulte, E. Segbefia, C. Smith, G. R. Smith, P. Stoler, V. Tadevosyan, L. Tang, M. Ungaro, A. Uzzle, S. Vidakovic, A. Villano, W. F. Vulcan, M. Wang, G. Warren, F. Wesselmann, B. Wojtsekhowski, S. A. Wood, C. Xu, L. Yuan, X. Zheng, H. Zhu, Onset of quark-hadron duality in pion electroproduction, Phys. Rev. Lett. 98 (2007) 022001.

doi:10.1103/PhysRevLett.98.022001.

[6] D. Abbott, A. Ahmidouch, T. A. Amatuni, C. Armstrong, J. Arrington, K. A. Assamagan, K. Bailey, O. K. Baker, S. Barrow, K. Beard, D. Beatty, S. Beedoe, E. Beise, E. Belz, C. Bochna, H. Breuer, E. E. W. Bruins, R. Carlini, J. Cha, N. Chant, C. Cothran, W. J. Cummings, S. Danagoulian, D. Day, D. DeSchepper, J.-E. Ducret, F. Duncan, J. Dunne, D. Dutta, T. Eden, R. Ent, H. T. Fortune, V. Frolov, D. F. Geesaman, H. Gao, R. Gilman, P. Guèye, J. O. Hansen, W. Hinton, R. J. Holt, C. Jackson, H. E. Jackson, C. E. Jones, S. Kaufman, J. J. Kelly, C. Keppel, M. Khandaker, W. Kim, E. Kinney, A. Klein, D. Koltenuk, L. Kramer, W. Lorenzon, K. McFarlane, D. J. Mack, R. Madey, P. Markowitz, J. Martin, A. Mateos, D. Meekins, M. A. Miller, R. Milner, J. Mitchell, R. Mohring, H. Mkrtchyan, A. M. Nathan, G. Niculescu, I. Niculescu, T. G. O'Neill, D. Potterveld, J. W. Price, J. Reinhold, C. Salgado, J. P. Schiffer, R. E. Segel, P. Stoler, R. Suleiman, V. Tadevosyan, L. Tang, B. Terburg, D. van Westrum, P. Welch, C. Williamson, S. Wood, C. Yan, J.-C. Yang, J. Yu, B. Zeidman, W. Zhao, B. Zihlmann, Quasifree $(e, e' p)$ reactions and proton propagation in nuclei, Phys. Rev. Lett. 80 (1998) 5072–5076. doi:10.1103/PhysRevLett.80.5072.

[7] K. Garrow, D. McKee, A. Ahmidouch, C. S. Armstrong, J. Arrington, R. Asaturyan, S. Avery, O. K. Baker, D. H. Beck, H. P. Blok, C. W. Bochna, W. Boeglin, P. Bosted, M. Bouwhuis, H. Breuer, D. S. Brown, A. Bruell, R. D. Carlini, N. S. Chant, A. Cochran, L. Cole, S. Danagoulian, D. B. Day, J. Dunne, D. Dutta, R. Ent, H. C. Fenker, B. Fox, L. Gan, D. Gaskell, A. Gasparian, H. Gao, D. F. Geesaman, R. Gilman, P. L. J. Guèye, M. Harvey, R. J. Holt, X. Jiang, C. E. Keppel, E. Kinney, Y. Liang, W. Lorenzon, A. Lung, D. J. Mack, P. Markowitz, J. W. Martin, K. McIlhany, D. Meekins, M. A. Miller, R. G. Milner, J. H. Mitchell, H. Mkrtchyan, B. A. Mueller, A. Nathan, G. Niculescu, I. Niculescu, T. G. O'Neill, V. Papavassiliou, S. Pate, R. B. Piercey, D. Potterveld, R. D. Ransome, J. Reinhold, E. Rollinde, P. Roos, A. J. Sarty, R. Sawafta, E. C. Schulte, E. Segbefia, C. Smith, S. Stepanyan, S. Strauch, V. Tadevosyan, L. Tang, R. Tieulent, A. Uzzle, W. F. Vulcan, S. A. Wood, F. Xiong, L. Yuan, M. Zeier, B. Zihlmann, V. Ziskin, Nuclear transparency from quasielastic $A(e, e' p)$ reactions up to $Q^2 = 8.1(\mathrm{GeV}/c)^2$, Phys. Rev. C 66 (2002) 044613. doi:10.1103/PhysRevC.66.044613.

[8] N. Fomin, J. Arrington, D. B. Day, D. Gaskell, A. Daniel, J. Seely, R. Asaturyan, F. Benmokhtar, W. Boeglin, B. Boillat, P. Bosted, A. Bruell, M. H. S. Bukhari, M. E. Christy, E. Chudakov, B. Clasie, S. H. Connell, M. M. Dalton, D. Dutta, R. Ent, L. El Fassi, H. Fenker, B. W. Filippone, K. Garrow, C. Hill, R. J. Holt, T. Horn, M. K. Jones, J. Jourdan, N. Kalantarians, C. E. Keppel, D. Kiselev, M. Kotulla, R. Lindgren, A. F. Lung, S. Malace, P. Markowitz, P. McKee, D. G. Meekins, T. Miyoshi, H. Mkrtchyan, T. Navasardyan, G. Niculescu, Y. Okayasu, A. K. Opper, C. Perdrisat, D. H. Potterveld, V. Punjabi, X. Qian, P. E. Reimer, J. Roche, V. M. Rodriguez, O. Rondon, E. Schulte, E. Segbefia, K. Slifer, G. R. Smith, P. Solvignon, V. Tadevosyan, S. Tajima, L. Tang, G. Testa, R. Trojer, V. Tvaskis, W. F. Vulcan, C. Wasko, F. R. Wesselmann, S. A. Wood, J. Wright, X. Zheng, Scaling of the F_2 structure function in nuclei and quark distributions at $x > 1$, Phys. Rev. Lett. 105 (2010) 212502. doi:10.1103/PhysRevLett.105.212502.

[9] N. Fomin, J. Arrington, R. Asaturyan, F. Benmokhtar, W. Boeglin, P. Bosted, A. Bruell, M. H. S. Bukhari, M. E. Christy, E. Chudakov, B. Clasie, S. H. Connell, M. M. Dalton, A. Daniel, D. B. Day, D. Dutta, R. Ent, L. El Fassi, H. Fenker, B. W. Filippone, K. Garrow, D. Gaskell, C. Hill, R. J. Holt, T. Horn, M. K. Jones, J. Jourdan, N. Kalantarians, C. E. Keppel, D. Kiselev, M. Kotulla, R. Lindgren, A. F. Lung, S. Malace, P. Markowitz, P. McKee, D. G. Meekins, H. Mkrtchyan, T. Navasardyan, G. Niculescu, A. K. Opper, C. Perdrisat, D. H. Potterveld, V. Punjabi, X. Qian, P. E. Reimer, J. Roche, V. M. Rodriguez, O. Rondon, E. Schulte, J. Seely, E. Segbefia, K. Slifer, G. R. Smith, P. Solvignon, V. Tadevosyan, S. Tajima, L. Tang, G. Testa, R. Trojer, V. Tvaskis, W. F. Vulcan, C. Wasko, F. R. Wesselmann, S. A. Wood, J. Wright, X. Zheng, New measurements of high-momentum nucleons and short-range structures in nuclei, Phys. Rev. Lett. 108 (2012) 092502. doi:10.1103/PhysRevLett.108.092502.

[10] S. Malace, M. Christy, C. Keppel, M. Niculescu, Precision measurements of the F_2 structure function at large x in the resonance region and beyond, JLab Proposal E12-10-002.
URL https://www.jlab.org/exp_prog/proposals/10/PR12-10-002.pdf

[11] D. Gaskell, J. Arrington, A. Daniel, N. Fomin, Detailed studies of the nuclear dependence of F_2 in light nuclei, Jlab Proposal E12-10-008.
URL https://www.jlab.org/exp_prog/proposals/10/PR12-10-008.pdf

[12] A. Karki, et al., First Measurement of the EMC effect in B10 and B11, Phys. Rev. C 108 (3) (2023) 035201. arXiv:2207.03850, doi:10.1103/PhysRevC.108.035201.

[13] D. Dutta, R. Ent, The search for color transparency at 12 gev, JLab Proposal E12-06-107.
URL https://www.jlab.org/exp_prog/proposals/06/PR12-06-107.pdf

[14] W. Boeglin, M. Jones, Deuteron electro-disintegration at very high missing momentum, JLab Proposal E12-10-108.
URL https://www.jlab.org/exp_prog/proposals/10/PR12-10-003.pdf

[15] D. Bhetuwal, et al., Ruling out Color Transparency in Quasielastic ^{12}C(e,e'p) up to Q^2 of 14.2 $(\mathrm{GeV}/c)^2$, Phys. Rev. Lett. 126 (8) (2021) 082301. arXiv:2011.00703, doi:10.1103/PhysRevLett.126.082301.

[16] C. Yero, et al., Probing the Deuteron at Very Large Internal Momenta, Phys. Rev. Lett. 125 (26) (2020) 262501. arXiv:2008.08058, doi:10.1103/PhysRevLett.125.262501.

[17] R. Ent, P. Bosted, E. Kinney, H. Mktrchyan, Transverse momentum dependence of semi-inclusive pion production, JLab Proposal E12-09-017.
URL https://www.jlab.org/exp_prog/PACpage/PAC38/proposals/Previously_Approved/E12-09-017_Update.pdf

[18] K. Hafidi, D. Dutta, D. Gaskell, Precise measurement of π^+/π^- ratios in semi-inclusive deep inelastic scattering part i: Charge symmetry violating quark distributions, JLab Proposal E12-09-002.
URL https://www.jlab.org/exp_prog/PACpage/PAC38/proposals/Previously_Approved/E12-09-002Update.pdf

[19] T. Horn and G. M. Huber , P. Markowitz , Studies of the l-t separated kaon electroproduction cross section from 5-11 gev, JLab Proposal E12-09-011.
URL https://www.jlab.org/exp_prog/PACpage/PAC38/proposals/Previously_Approved/E12-09-011_Update.pdf

[20] B. Duran, et al., Determining the gluonic gravitational form factors of the proton, Nature 615 (7954) (2023) 813–816. arXiv:2207.05212, doi:10.1038/s41586-023-05730-4.

[21] R. Li, et al., Measured proton electromagnetic structure deviates from theoretical predictions, Nature 611 (7935) (2022) 265–270. arXiv:2210.11461, doi:10.1038/s41586-022-05248-1.

[22] T. Horn, G. Huber, D. Gaskell *et al.*,, Study of the l–t separated pion electroproduction cross section at 11 gev and measurement of the charged pion form factor to high q^2, approved Jefferson Lab 12 GeV Experiment (2019).
URL http://www.jlab.org/exp_prog/proposals/19/E12-19-006.pdf

[23] X. Zheng, G. Cates, J. P. Chen, Z. E. Meziani *et al.*,, Measurement of neutron spin asymmetry a1n in the valence quark region using an 11 gev beam and a polarized 3he target in hall c, approved Jefferson Lab 12 GeV Experiment (2006).
URL http://www.jlab.org/exp_prog/proposals/06/PR12-06-110.pdf

[24] B. Sawatzky, T. Averett, W. Korsch, Z. E. Meziani *et al.*,, A path to 'color polarizabilities' in the neutron: A precision measurement of the neutron g_2 and d_2 at high q^2 in hall c, approved Jefferson Lab 12 GeV Experiment (2006).
URL http://www.jlab.org/exp_prog/proposals/06/PR12-06-121.pdf

[25] O. Hen, F. Hauenstein, D. Higinbotham, L. Weinstein *et al.*,, The cafe experiment: Short-range pairing mechanisms in heavy nuclei, approved Jefferson Lab 12 GeV Experiment (2017).
URL https://misportal.jlab.org/pacProposals/proposals/1352/attachments/98357/Proposal.pdf

[26] J. Arrington, D. Day, N. Fomin, P. Solvignon *et al.*,, Inclusive scattering from nuclei at $x > 1$ in the quasielastic and deeply inelastic regimes, approved Jefferson Lab 12 GeV Experiment (2006).
URL http://www.jlab.org/exp_prog/proposals/06/PR12-06-105.pdf

[27] M. Moore, B. Waidyawansa, S. Covrig, R. Carlini, J. Benesch, Primary beam steering due to field leakage from superconducting shms magnets, Journal of Instrumentation 9 (11) (2014) T11002. doi:10.1088/1748-0221/9/11/T11002.
URL https://dx.doi.org/10.1088/1748-0221/9/11/T11002

[28] P. J. Griffin, T. F. Luera, F. W. S. P. J. Cooper, S. G. Karr, G. L. Hash, E. Fuller, The role of thermal and fission neutrons in reactor neutron-induced upsets in commercial srams., IEEE Transactions on Nuclear Science 44 (1997) 2079–2086.

[29] C. I. Underwood, The single-event-effect behaviour of commercial-off-the-shelf memory devices - a decade in the low-earth orbit, IEEE Transactions on Nuclear Science 45.

[30] T. Horn, SHMS Shielding Design, JLab Hall C Document Database 392-v1.
URL https://hallcweb.jlab.org/doc-private/ShowDocument?docid=392

[31] W. R. Leo, Techniques for nuclear and particle physics experiments: a how-to approach; 2nd ed., Springer, Berlin, 1994. doi:10.1007/978-3-642-57920-2.
URL https://cds.cern.ch/record/302344

[32] J. F. B. (ed.), Mcnp - a general monte carlo n-particle transport code version a, LA-12625-M, Los Alamos National Laboratory, Los Alamos, New Mexico.

[33] Y. Birenbaum, Z. Berant, S. Kahane, A. Wolf, R. Moreh, Absolute cross sections for (γ,n) transitions in lead, bismuth, and terbium, Phys. Rev. C 51 (1995) 3496–3499. doi:10.1103/PhysRevC.51.3496.
URL https://link.aps.org/doi/10.1103/PhysRevC.51.3496

[34] D. Marsh, Particle practice, https://concreteproducts.com/index.php/2014/02/14/particle-practice/ (2014).

[35] T. Skwarnicki, Beam test of a c4f8o-mapmt rich prototype, Nuclear Instruments and Methods in Physics Research Section A: Accelerators, Spectrometers, Detectors and Associated Equipment 553 (1) (2005) 339–344, proceedings of the fifth International Workshop on Ring Imaging Detectors. doi:https://doi.org/10.1016/j.nima.2005.08.070.
URL https://www.sciencedirect.com/science/article/pii/S0168900205016219

[36] ASM Aerospace Specification Metals, 2501 NW 34th Pl #29, Pompano Beach, FL 33069, United States.
URL https://aerospacemetals.com/

[37] Sinclair Glass, 105 N Wabash Ave, Hartford City, IN 47348, United States.
URL https://sinclairglass.com/

[38] W. Li, Heavy gas cherenkov detector construction for hall c at thomas jefferson national accelerator facility, University of Regina, MSc Thesis (2012).
URL http://ourspace.uregina.ca/bitstream/handle/10294/3818/Li_Wenliang_200302222_MSC_PHYS_Spring2013.pdf

[39] Corning International, 1 Riverfront Plaza, Corning, NY 14831, United States.
URL https://www.corning.com/

[40] Hamamatsu Photonics K.K., 314-5 Shimokanzo, Iwata, Shizuoka 438-0126, Japan.
URL http://www.hamamatsu.com/

[41] Evaporated Coatings Inc., 2365 Maryland Rd, Willow Grove, PA 19090, United States.
URL https://evaporatedcoatings.com/

[42] Rayotek Scientific, 8845 Rehco Rd, San Diego, CA 92121, United States.
URL https://rayotek.com/

[43] Detector Technologies Group (CERN), espl. des Particules 1, 1211 Meyrin, Switzerland.
URL https://ep-dep-dt.web.cern.ch/thin-film-glass-service

[44] ET Enterprises, 45 Riverside Way, Uxbridge UB8 2YF, United Kingdom.
URL http://et-enterprises.com/

[45] T. Horn, et al., The Aerogel Čerenkov detector for the SHMS magnetic spectrometer in Hall C at Jefferson Lab, Nucl. Instrum. Meth. A842 (2017) 28–47. arXiv:1607.05264, doi:10.1016/j.nima.2016.10.039.

[46] T. Horn, H. Mkrtchyan, S. Ali, A. Asaturyan, M. Carmignotto, A. Dittmann, D. Dutta, R. Ent, N. Hlavin, Y. Illieva, A. Mkrtchyan, P. Nadel-Turonski, I. Pegg, A. Ramos, J. Reinhold, I. Sapkota, V. Tadevosyan, S. Zhamkochyan, S. Wood, The aerogel Čerenkov detector for the shms magnetic spectrometer in hall c at jefferson lab, Nuclear Instruments and Methods in Physics Research Section A: Accelerators, Spectrometers, Detectors and Associated Equipment 842 (2017) 28–47. doi:https://doi.org/10.1016/j.nima.2016.10.039.
URL https://www.sciencedirect.com/science/article/pii/S0168900216310774

[47] Gore, W. L. & Assosiates INC., 555 Paper Mill Road, Newark, DE 19711, United States.
URL http://www.gore.com

[48] Millipore Corporation, 80 Ashly Road, Bedford, MA 01730.
URL http://www.millipore.com/

[49] I. Adachi, et al., Study of highly transparent silica aerogel as a RICH radiator, Nucl. Instrum. Meth. A553 (2005) 146–151. doi:10.1016/j.nima.2005.08.022.

[50] E. Aschenauer, et al., Optical characterization of n = 1.03 silica aerogel used as radiator in the RICH of HERMES, Nucl. Instrum. Meth. A440 (2000) 338–347. doi:10.1016/S0168-9002(99)00923-7.

[51] T. Horn, G.M. Huber *et al.*,, Scaling study of the l-t separated pion electroproduction cross section at 11 gev, approved

Jefferson Lab 12 GeV Experiment (2007).
URL https://www.jlab.org/exp_prog/PACpage/PAC38/proposals/Previously_Approved/E12-07-105_Update.pdf

[52] P. Bosted, R. Ent, E. Kinney *et al.*,, Measurement of the ratio $r = \sigma_l/\sigma_t$ in semi-inclusive deep-inelastic regimes, approved Jefferson Lab 12 GeV Experiment (2006).
URL https://www.jlab.org/exp_prog/PACpage/PAC36/Proposals/previously%20approved/E12-06-104.pdf

[53] R. Asaturyan, et al., The aerogel threshold Cerenkov detector for the high momentum spectrometer in Hall C at Jefferson Lab, Nucl. Instrum. Meth. A548 (2005) 364–374. arXiv:physics/0411147, doi:10.1016/j.nima.2005.04.058.

[54] H. Mkrtchyan, R. Carlini, V. Tadevosyan, J. Arrington, A. Asaturyan, M. Christy, D. Dutta, R. Ent, H. Fenker, D. Gaskell, T. Horn, M. Jones, C. Keppel, D. Mack, S. Malace, A. Mkrtchyan, M. Niculescu, J. Seely, V. Tvaskis, S. Wood, S. Zhamkochyan, The lead-glass electromagnetic calorimeters for the magnetic spectrometers in hall c at jefferson lab, Nuclear Instruments and Methods in Physics Research Section A: Accelerators, Spectrometers, Detectors and Associated Equipment 719 (2013) 85–100. doi:https://doi.org/10.1016/j.nima.2013.03.070.
URL https://www.sciencedirect.com/science/article/pii/S0168900213004154

[55] Lytkarino optical glass plant, lytkarino Optical Glass Factory, 140061, Lytkarino, Moscow Oblast, Russia.
URL https://lzos.ru/

[56] H. Avakian, N. Bianchi, G. Capitani, E. De Sanctis, A. Fantoni, V. Giourdjian, R. Mozzetti, V. Muccifora, M. Nupieri, A. Reolon, P. Rossi, J. van den Brand, M. Doets, T. Henkes, M. Kolstein, A. Airapetian, N. Akopov, M. Amarian, R. Avakian, A. Avetissian, V. Garibian, S. Taroian, P. Galumian, A. Simon, B. Bray, B. Filippone, A. Lung, Performance of f101 radiation resistant lead glass shower counters, Nuclear Instruments and Methods in Physics Research Section A: Accelerators, Spectrometers, Detectors and Associated Equipment 378 (1) (1996) 155–161. doi:https://doi.org/10.1016/0168-9002(96)00443-3.
URL https://www.sciencedirect.com/science/article/pii/0168900296004433

[57] T. Amatuni, G. Kazaryan, H. Mkrtchyan, V. Tadevosyn, W. Vulcan, A study of gain variation in philips xp-3462p photomultipliers, Nuclear Instruments and Methods in Physics Research Section A: Accelerators, Spectrometers, Detectors and Associated Equipment 374 (1) (1996) 39–47. doi:https://doi.org/10.1016/0168-9002(96)37473-1.
URL https://www.sciencedirect.com/science/article/pii/0168900296374731

[58] C. Zorn, Private Communication (2008).

[59] S. Agostinelli, J. Allison, K. Amako, J. Apostolakis, H. Araujo, P. Arce, M. Asai, D. Axen, S. Banerjee, G. Barrand, F. Behner, L. Bellagamba, J. Boudreau, L. Broglia, A. Brunengo, H. Burkhardt, S. Chauvie, J. Chuma, R. Chytracek, G. Cooperman, G. Cosmo, P. Degtyarenko, A. Dell'Acqua, G. Depaola, D. Dietrich, R. Enami, A. Feliciello, C. Ferguson, H. Fesefeldt, G. Folger, F. Foppiano, A. Forti, S. Garelli, S. Giani, R. Giannitrapani, D. Gibin, J. Gómez Cadenas, I. González, G. Gracia Abril, G. Greeniaus, W. Greiner, V. Grichine, A. Grossheim, S. Guatelli, P. Gumplinger, R. Hamatsu, K. Hashimoto, H. Hasui, A. Heikkinen, A. Howard, V. Ivanchenko, A. Johnson, F. Jones, J. Kallenbach, N. Kanaya, M. Kawabata, Y. Kawabata, M. Kawaguti, S. Kelner, P. Kent, A. Kimura, T. Kodama, R. Kokoulin, M. Kossov, H. Kurashige, E. Lamanna, T. Lampén, V. Lara, V. Lefebure, F. Lei, M. Liendl, W. Lockman, F. Longo, S. Magni, M. Maire, E. Medernach, K. Minamimoto, P. Mora de Freitas, Y. Morita, K. Murakami, M. Nagamatu, R. Nartallo, P. Nieminen, T. Nishimura, K. Ohtsubo, M. Okamura, S. O'Neale, Y. Oohata, K. Paech, J. Perl, A. Pfeiffer, M. Pia, F. Ranjard, A. Rybin, S. Sadilov, E. Di Salvo, G. Santin, T. Sasaki, N. Savvas, Y. Sawada, S. Scherer, S. Sei, V. Sirotenko, D. Smith, N. Starkov, H. Stoecker, J. Sulkimo, M. Takahata, S. Tanaka, E. Tcherniaev, E. Safai Tehrani, M. Tropeano, P. Truscott, H. Uno, L. Urban, P. Urban, M. Verderi, A. Walkden, W. Wander, H. Weber, J. Wellisch, T. Wenaus, D. Williams, D. Wright, T. Yamada, H. Yoshida, D. Zschiesche, Geant4—a simulation toolkit, Nuclear Instruments and Methods in Physics Research Section A: Accelerators, Spectrometers, Detectors and Associated Equipment 506 (3) (2003) 250–303. doi:https://doi.org/10.1016/S0168-9002(03)01368-8.
URL https://www.sciencedirect.com/science/article/pii/S0168900203013688

[60] J. Apostolakis, G. Folger, V. Grichine, A. Heikkinen, A. Howard, V. Ivanchenko, P. Kaitaniemi, T. Koi, M. Kosov, J. M. Quesada, A. Ribon, V. Uzhinskiy, D. Wright, Progress in hadronic physics modelling in geant4, Journal of Physics: Conference Series 160 (1) (2009) 012073. doi:10.1088/1742-6596/160/1/012073.
URL https://dx.doi.org/10.1088/1742-6596/160/1/012073

[61] M. Born, E. Wolf, Principles of Optics, 3rd Edition, Pergamon Press, 1965.

[62] Ts. Amatuni, On the calibration of segmented full absorption calorimeters, unpublished (1995).

[63] JLab DAQ Group, Cebaf online data acquistion system (coda).
URL https://coda.jlab.org/

[64] JLab DAQ Group, Jefferson lab f250 flash adc module.
URL https://coda.jlab.org/drupal/node/91/10671311

[65] CAEN, Caen v1190 time to digital converter.
URL https://www.caen.it/products/v1190a-2esst/

[66] EPICS Collaboration, Experimental physics and industrial control system (epics).
URL https://epics-controls.org/

[67] JLab Scientific Computing, Jefferson lab farm.
URL https://scicomp.jlab.org

[68] O. Hansen *et al.*, Hall a analyzer.
URL https://redmine.jlab.org/projects/podd/wiki

[69] R. Brun, F. Rademakers, Root — an object oriented data analysis framework, Nuclear Instruments and Methods in Physics Research Section A: Accelerators, Spectrometers, Detectors and Associated Equipment 389 (1) (1997) 81–86, new Computing Techniques in Physics Research V. doi:https://doi.org/10.1016/S0168-9002(97)00048-X.
URL https://www.sciencedirect.com/science/article/pii/S016890029700048X

[70] E. Brash, J. Hovdebo, G. Lolos, G. Huber, R. van der Meer, Z. Papandreou, Operational performance of the hall a mirror aerogel cherenkov counter, Nuclear Instruments and Methods in Physics Research Section A: Accelerators, Spectrometers, Detectors and Associated Equipment 487 (3) (2002) 346–352. doi:https://doi.org/10.1016/S0168-9002(01)02199-4.
URL https://www.sciencedirect.com/science/article/pii/S0168900201021994

[71] O. Ullaland, Fluid systems for rich detectors, Nuclear Instruments and Methods in Physics Research Section A: Accelerators, Spectrometers, Detectors and Associated Equipment 553 (1) (2005) 107–113, proceedings of the

fifth International Workshop on Ring Imaging Detectors. doi:https://doi.org/10.1016/j.nima.2005.08.033.
URL https://www.sciencedirect.com/science/article/pii/S0168900205015779

[72] G. Ambrose, Blinded by the light: Commissioning of the hall c shms heavy gas cherenkov detector, University of Regina, MSc Thesis (2018).
URL http://ourspace.uregina.ca/bitstream/handle/10294/8882/Ambrose_Ryan_MSc_PHYS_Spring2019.pdf

[73] D. Bhetuwal, J. Matter, H. Szumila-Vance, M. L. Kabir, D. Dutta, R. Ent, D. Abrams, Z. Ahmed, B. Aljawrneh, S. Alsalmi, R. Ambrose, D. Androic, W. Armstrong, A. Asaturyan, K. Assumin-Gyimah, C. Ayerbe Gayoso, A. Bandari, S. Basnet, V. Berdnikov, H. Bhatt, D. Biswas, W. U. Boeglin, P. Bosted, E. Brash, M. H. S. Bukhari, H. Chen, J. P. Chen, M. Chen, E. M. Christy, S. Covrig, K. Craycraft, S. Danagoulian, D. Day, M. Diefenthaler, M. Dlamini, J. Dunne, B. Duran, R. Evans, H. Fenker, N. Fomin, E. Fuchey, D. Gaskell, T. N. Gautam, F. A. Gonzalez, J. O. Hansen, F. Hauenstein, A. V. Hernandez, T. Horn, G. M. Huber, M. K. Jones, S. Joosten, A. Karki, C. Keppel, A. Khanal, P. M. King, E. Kinney, H. S. Ko, M. Kohl, N. Lashley-Colthirst, S. Li, W. B. Li, A. H. Liyanage, D. Mack, S. Malace, P. Markowitz, D. Meekins, R. Michaels, A. Mkrtchyan, H. Mkrtchyan, S. J. Nazeer, S. Nanda, G. Niculescu, I. Niculescu, D. Nguyen, Nuruzzaman, B. Pandey, S. Park, E. Pooser, A. Puckett, M. Rehfuss, J. Reinhold, N. Santiesteban, B. Sawatzky, G. R. Smith, A. Sun, V. Tadevosyan, R. Trotta, S. A. Wood, C. Yero, J. Zhang, Ruling out color transparency in quasielastic ^{12}C(e, e' p) up to Q^2 of 14.2 (GeV/c)^2, Phys. Rev. Lett. 126 (2021) 082301. doi:10.1103/PhysRevLett.126.082301.
URL https://link.aps.org/doi/10.1103/PhysRevLett.126.082301

[74] D. Bhetuwal, J. Matter, H. Szumila-Vance, C. A. Gayoso, M. L. Kabir, D. Dutta, R. Ent, D. Abrams, Z. Ahmed, B. Aljawrneh, S. Alsalmi, R. Ambrose, D. Androic, W. Armstrong, A. Asaturyan, K. Assumin-Gyimah, A. Bandari, S. Basnet, V. Berdnikov, H. Bhatt, D. Biswas, W. U. Boeglin, P. Bosted, E. Brash, M. H. S. Bukhari, H. Chen, J. P. Chen, M. Chen, E. M. Christy, S. Covrig, K. Craycraft, S. Danagoulian, D. Day, M. Diefenthaler, M. Dlamini, J. Dunne, B. Duran, R. Evans, H. Fenker, N. Fomin, E. Fuchey, D. Gaskell, T. N. Gautam, F. A. Gonzalez, J. O. Hansen, F. Hauenstein, A. V. Hernandez, T. Horn, G. M. Huber, M. K. Jones, S. Joosten, A. Karki, C. Keppel, A. Khanal, P. M. King, E. Kinney, H. S. Ko, M. Kohl, N. Lashley-Colthirst, S. Li, W. B. Li, A. H. Liyanage, D. Mack, S. Malace, P. Markowitz, D. Meekins, R. Michaels, A. Mkrtchyan, H. Mkrtchyan, S. J. Nazeer, S. Nanda, G. Niculescu, I. Niculescu, D. Nguyen, Nuruzzaman, B. Pandey, S. Park, E. Pooser, A. Puckett, M. Rehfuss, J. Reinhold, N. Santiesteban, B. Sawatzky, G. R. Smith, A. Sun, V. Tadevosyan, R. Trotta, S. A. Wood, C. Yero, J. Zhang, Constraints on the onset of color transparency from quasielastic ^{12}C($e, e'p$) up to $Q^2 = 14.2$ (GeV/c)^2, Phys. Rev. C 108 (2023) 025203. doi:10.1103/PhysRevC.108.025203.
URL https://link.aps.org/doi/10.1103/PhysRevC.108.025203

[75] A. Karki, D. Biswas, F. A. Gonzalez, W. Henry, C. Morean, A. Nadeeshani, A. Sun, D. Abrams, Z. Ahmed, B. Aljawrneh, S. Alsalmi, R. Ambrose, D. Androic, W. Armstrong, J. Arrington, A. Asaturyan, K. Assumin-Gyimah, C. Ayerbe Gayoso, A. Bandari, J. Bane, J. Barrow, S. Basnet, V. Berdnikov, H. Bhatt, D. Bhetuwal, W. U. Boeglin, P. Bosted, E. Brash, M. H. S. Bukhari, H. Chen, J. P. Chen, M. Chen, M. E. Christy, S. Covrig, K. Craycraft, S. Danagoulian, D. Day, M. Diefenthaler, M. Dlamini, J. Dunne, B. Duran, D. Dutta, C. Elliott, R. Ent, H. Fenker, N. Fomin, E. Fuchey, D. Gaskell, T. N. Gautam, J. O. Hansen, F. Hauenstein, A. V. Hernandez, T. Horn, G. M. Huber, M. K. Jones, S. Joosten, M. L. Kabir, N. Kalantarians, C. Keppel, A. Khanal, P. M. King, E. Kinney, H. S. Ko, M. Kohl, N. Lashley-Colthirst, S. Li, W. B. Li, A. H. Liyanage, D. Mack, S. Malace, P. Markowitz, J. Matter, D. Meekins, R. Michaels, A. Mkrtchyan, H. Mkrtchyan, S. Nanda, D. Nguyen, G. Niculescu, I. Niculescu, Nuruzzaman, B. Pandey, S. Park, E. Pooser, A. J. R. Puckett, M. Rehfuss, J. Reinhold, N. Santiesteban, B. Sawatzky, G. R. Smith, H. Szumila-Vance, A. S. Tadepalli, V. Tadevosyan, R. Trotta, S. A. Wood, C. Yero, J. Zhang, First measurement of the emc effect in ^{10}B and ^{11}B, Phys. Rev. C 108 (2023) 035201. doi:10.1103/PhysRevC.108.035201.
URL https://link.aps.org/doi/10.1103/PhysRevC.108.035201

[76] C. Yero, D. Abrams, Z. Ahmed, A. Ahmidouch, B. Aljawrneh, S. Alsalmi, R. Ambrose, W. Armstrong, A. Asaturyan, K. Assumin-Gyimah, C. Ayerbe Gayoso, A. Bandari, J. Bane, S. Basnet, V. V. Berdnikov, J. Bericic, H. Bhatt, D. Bhetuwal, D. Biswas, W. U. Boeglin, P. Bosted, E. Brash, M. H. S. Bukhari, H. Chen, J. P. Chen, M. Chen, M. E. Christy, S. Covrig, K. Craycraft, S. Danagoulian, D. Day, M. Diefenthaler, M. Dlamini, J. Dunne, B. Duran, D. Dutta, R. Ent, R. Evans, H. Fenker, N. Fomin, E. Fuchey, D. Gaskell, T. N. Gautam, F. A. Gonzalez, J. O. Hansen, F. Hauenstein, A. V. Hernandez, T. Horn, G. M. Huber, M. K. Jones, S. Joosten, M. L. Kabir, A. Karki, C. E. Keppel, A. Khanal, P. King, E. Kinney, N. Lashley-Colthirst, S. Li, W. B. Li, A. H. Liyanage, D. J. Mack, S. P. Malace, J. Matter, D. Meekins, R. Michaels, A. Mkrtchyan, H. Mkrtchyan, S. J. Nazeer, S. Nanda, G. Niculescu, M. Niculescu, D. Nguyen, N. Nuruzzaman, B. Pandey, S. Park, C. F. Perdrisat, E. Pooser, M. Rehfuss, J. Reinhold, B. Sawatzky, G. R. Smith, A. Sun, H. Szumila-Vance, V. Tadevosyan, S. A. Wood, J. Zhang, Probing the deuteron at very large internal momenta, Phys. Rev. Lett. 125 (2020) 262501. doi:10.1103/PhysRevLett.125.262501.
URL https://link.aps.org/doi/10.1103/PhysRevLett.125.262501

[77] R. Li, N. Sparveris, H. Atac, M. K. Jones, M. Paolone, Z. Akbar, C. A. Gayoso, V. Berdnikov, D. Biswas, M. Boer, A. Camsonne, J.-P. Chen, M. Diefenthaler, B. Duran, D. Dutta, D. Gaskell, O. Hansen, F. Hauenstein, N. Heinrich, W. Henry, T. Horn, G. M. Huber, S. Jia, S. Joosten, A. Karki, S. J. D. Kay, V. Kumar, X. Li, W. B. Li, A. H. Liyanage, S. Malace, P. Markowitz, M. McCaughan, Z.-E. Meziani, H. Mkrtchyan, C. Morean, M. Muhoza, A. Narayan, B. Pasquini, M. Rehfuss, B. Sawatzky, G. R. Smith, A. Smith, R. Trotta, C. Yero, X. Zheng, J. Zhou, Measured proton electromagnetic structure deviates from theoretical predictions, Nature 611 (7935) (2022) 265–270. doi:10.1038/s41586-022-05248-1.
URL https://doi.org/10.1038/s41586-022-05248-1

[78] B. Duran, Z.-E. Meziani, S. Joosten, M. K. Jones, S. Prasad, C. Peng, W. Armstrong, H. Atac, E. Chudakov, H. Bhatt, D. Bhetuwal, M. Boer, A. Camsonne, J.-P. Chen, M. M. Dalton, N. Deokar, M. Diefenthaler, J. Dunne, L. El Fassi, E. Fuchey, H. Gao, D. Gaskell, O. Hansen, F. Hauenstein, D. Higinbotham, S. Jia, A. Karki, C. Keppel, P. King, H. S. Ko, X. Li, R. Li, D. Mack, S. Malace, M. McCaughan, R. E. McClellan, R. Michaels, D. Meekins, M. Paolone, L. Pentchev, E. Pooser, A. Puckett, R. Radloff, M. Rehfuss, P. E. Reimer, S. Riordan, B. Sawatzky, A. Smith, N. Sparveris, H. Szumila-Vance, S. Wood, J. Xie, Z. Ye, C. Yero, Z. Zhao, Determining the glu-

onic gravitational form factors of the proton, Nature 615 (7954) (2023) 813–816. doi:10.1038/s41586-023-05730-4.
URL https://doi.org/10.1038/s41586-023-05730-4

[79] A. Accardi, P. Achenbach, D. Adhikari, A. Afanasev, C. S. Akondi, N. Akopov, M. Albaladejo, H. Albataineh, M. Albrecht, B. Almeida-Zamora, M. Amaryan, D. Androić, W. Armstrong, D. S. Armstrong, M. Arratia, J. Arrington, A. Asaturyan, A. Austregesilo, H. Avagyan, T. Averett, C. A. Gayoso, A. Bacchetta, A. B. Balantekin, N. Baltzell, L. Barion, P. C. Barry, A. Bashir, M. Battaglieri, V. Bellini, I. Belov, O. Benhar, B. Benkel, F. Benmokhtar, W. Bentz, V. Bertone, H. Bhatt, A. Bianconi, L. Bibrzycki, R. Bijker, D. Binosi, D. Biswas, M. Boër, W. Boeglin, S. A. Bogacz, M. Boglione, M. Bondí, E. E. Boos, P. Bosted, G. Bozzi, E. J. Brash, R. A. Briceño, P. D. Brindza, W. J. Briscoe, S. J. Brodsky, W. K. Brooks, V. D. Burkert, A. Camsonne, T. Cao, L. S. Cardman, D. S. Carman, M. Carpinelli, G. D. Cates, J. Caylor, A. Celentano, F. G. Celiberto, M. Cerutti, L. Chang, P. Chatagnon, C. Chen, J.-P. Chen, T. Chetry, A. Christopher, E. Christy, E. Chudakov, E. Cisbani, I. C. Cloët, J. J. Cobos-Martinez, E. O. Cohen, P. Colangelo, P. L. Cole, M. Constantinou, M. Contalbrigo, G. Costantini, W. Cosyn, C. Cotton, A. Courtoy, S. C. Dusa, V. Crede, Z. F. Cui, A. D'Angelo, M. Döring, M. M. Dalton, I. Danilkin, M. Davydov, D. Day, F. D. Fazio, M. D. Napoli, R. D. Vita, D. J. Dean, M. Defurne, A. Deur, B. Devkota, S. Dhital, P. D. Nezza, M. Diefenthaler, S. Diehl, C. Dilks, M. Ding, C. Djalali, S. Dobbs, R. Dupré, D. Dutta, R. G. Edwards, H. Egiyan, L. Ehinger, G. Eichmann, M. Elaasar, L. Elouadrhiri, A. E. Alaoui, L. E. Fassi, A. Emmert, M. Engelhardt, R. Ent, D. J. Ernst, P. Eugenio, G. Evans, C. Fanelli, S. Fegan, C. Fernández-Ramírez, L. A. Fernandez, I. P. Fernando, A. Filippi, C. S. Fischer, C. Fogler, N. Fomin, L. Frankfurt, T. Frederico, A. Freese, Y. Fu, L. Gamberg, L. Gan, F. Gao, H. Garcia-Tecocoatzi, D. Gaskell, A. Gasparian, K. Gates, G. Gavalian, P. K. Ghoshal, A. Giachino, F. Giacosa, F. Giannuzzi, G. P. Gilfoyle, F.-X. Girod, D. I. Glazier, C. Gleason, S. Godfrey, J. L. Goity, A. A. Golubenko, S. Gonzàlez-Solís, R. W. Gothe, Y. Gotra, K. Griffioen, O. Grocholski, B. Grube, P. Guèye, F. K. Guo, Y. Guo, L. Guo, T. J. Hague, N. Hammoud, J. O. Hansen, M. Hattawy, F. Hauenstein, T. Hayward, D. Heddle, N. Heinrich, O. Hen, D. W. Higinbotham, I. M. Higuera-Angulo, A. N. H. Blin, A. Hobart, T. Hobbs, D. E. Holmberg, T. Horn, P. Hoyer, G. M. Huber, P. Hurck, P. T. P. Hutauruk, Y. Ilieva, I. Illari, D. G. Ireland, E. L. Isupov, A. Italiano, I. Jaegle, N. S. Jarvis, D. Jenkins, S. Jeschonnek, C.-R. Ji, H. S. Jo, M. Jones, R. T. Jones, D. C. Jones, K. Joo, M. Junaid, T. Kageya, N. Kalantarians, A. Karki, G. Karyan, A. T. Katramatou, S. J. D. Kay, R. Kazimi, C. D. Keith, C. Keppel, A. Kerbizi, V. Khachatryan, A. Khanal, M. Khandaker, A. Kim, E. R. Kinney, M. Kohl, A. Kotzinian, B. T. Kriesten, V. Kubarovsky, B. Kubis, S. E. Kuhn, V. Kumar, T. Kutz, M. Leali, R. F. Lebed, P. Lenisa, L. Leskovec, S. Li, X. Li, J. Liao, H. W. Lin, L. Liu, S. Liuti, N. Liyanage, Y. Lu, I. J. D. MacGregor, D. J. Mack, L. Maiani, K. A. Mamo, G. Mandaglio, C. Mariani, P. Markowitz, H. Marukyan, V. Mascagna, V. Mathieu, J. Maxwell, M. Mazouz, M. McCaughan, R. D. McKeown, B. McKinnon, D. Meekins, W. Melnitchouk, A. Metz, C. A. Meyer, Z. E. Meziani, C. Mezrag, R. Michaels, G. A. Miller, T. Mineeva, A. S. Miramontes, M. Mirazita, K. Mizutani, H. Mkrtchyan, A. Mkrtchyan, B. Moffit, P. Mohanmurthy, V. I. Mokeev, P. Monaghan, G. Montaña, R. Montgomery, A. Moretti, J. M. M. Chàvez, U. Mosel, A. Movsisyan, P. Musico, S. A. Nadeeshani, P. M. Nadolsky, S. X. Nakamura, J. Nazeer, A. V. Nefediev, K. Neupane, D. Nguyen, S. Niccolai, I. Niculescu, G. Niculescu, E. R. Nocera, M. Nycz, F. I. Olness, P. G. Ortega, M. Osipenko, E. Pace, B. Pandey, P. Pandey, Z. Papandreou, J. Papavassiliou, L. L. Pappalardo, G. Paredes-Torres, R. Paremuzyan, S. Park, B. Parsamyan, K. D. Paschke, B. Pasquini, E. Passemar, E. Pasyuk, T. Patel, C. Paudel, S. J. Paul, J.-C. Peng, L. Pentchev, R. Perrino, R. J. Perry, K. Peters, G. G. Petratos, W. Phelps, E. Piasetzky, A. Pilloni, B. Pire, D. Pitonyak, M. L. Pitt, A. D. Polosa, M. Pospelov, A. C. Postuma, J. Poudel, L. Preet, S. Prelovsek, J. W. Price, A. Prokudin, A. J. R. Puckett, J. R. Pybus, S. X. Qin, J. W. Qiu, M. Radici, H. Rashidi, A. D. Rathnayake, B. A. Raue, T. Reed, P. E. Reimer, J. Reinhold, J. M. Richard, M. Rinaldi, F. Ringer, M. Ripani, J. Ritman, J. R. West, A. Rivero-Acosta, C. D. Roberts, A. Rodas, S. Rodini, J. Rodríguez-Quintero, T. C. Rogers, J. Rojo, P. Rossi, G. C. Rossi, G. Salmè, S. N. Santiesteban, E. Santopinto, M. Sargsian, N. Sato, S. Schadmand, A. Schmidt, S. M. Schmidt, G. Schnell, R. A. Schumacher, P. Schweitzer, I. Scimemi, K. C. Scott, D. A. Seay, J. Segovia, K. Semenov-Tian-Shansky, A. Seryi, A. S. Sharda, M. R. Shepherd, E. V. Shirokov, S. Shrestha, U. Shrestha, V. I. Shvedunov, A. Signori, K. J. Slifer, W. A. Smith, A. Somov, P. Souder, N. Sparveris, F. Spizzo, M. Spreafico, S. Stepanyan, J. R. Stevens, I. I. Strakovsky, S. Strauch, M. Strikman, S. Su, B. C. L. Sumner, E. Sun, M. Suresh, C. Sutera, E. S. Swanson, A. P. Szczepaniak, P. Sznajder, H. Szumila-Vance, L. Szymanowski, A. S. Tadepalli, V. Tadevosyan, B. Tamang, V. V. Tarasov, A. Thiel, X. B. Tong, R. Tyson, M. Ungaro, G. M. Urciuoli, A. Usman, A. Valcarce, S. Vallarino, C. A. Vaquera-Araujo, L. Venturelli, F. Vera, A. Vladimirov, A. Vossen, J. Wagner, X. Wei, L. B. Weinstein, C. Weiss, R. Williams, D. Winney, B. Wojtsekhowski, M. H. Wood, T. Xiao, S. S. Xu, Z. Ye, C. Yero, C. P. Yuan, M. Yurov, N. Zachariou, Z. Zhang, Z. W. Zhao, Y. Zhao, X. Zheng, X. Zhou, V. Ziegler, B. Zihlmann, W. de Paula, G. F. de Téramond, Strong interaction physics at the luminosity frontier with 22 gev electrons at jefferson lab (2023). arXiv:2306.09360.